Multi-Spectral Confocal Microscopy for Localization of Exogenous Contrast Agents in Nonmelanoma Skin Cancers

A Thesis Presented

by

Jose Goncalves Barbosa

to

The Department of Electrical and Computer Engineering

in partial fulfillment of the requirements

for the degree of

Master of Science

in

Electrical Engineering

in the field of

Electromagnetics, Optics, and Plasma

Northeastern University

Boston, Massachusetts

December 2004

Acknowledgements

This project was a collaborating effort between Northeastern University and Wellman Laboratories of Photomedicine, Massachusetts General Hospital. I would like to thank my thesis advisor Charles A. DiMarzio for his patients, support, and invaluable guidance through out my master's program and specifically master's research. Also from Northeastern I would like to thank Milind Rajadhyaksha for his direction and expertise in confocal microscopy. From Wellman Laboratories, I would also like to thank my thesis co-advisor Anna N. Yaroslavsky for her countless contributions, suggestions, and expertise in tissue optics and contrast agents. I would like to thank Victor Neel and his staff for providing Mohs frozen sections and histology slides. I would like to thank all Wellman personnel that contributed to the success of this project. I also thank R. Rox Anderson for his advise, ideas, and financial support. This project was supported by the Wellman Graduate Student Program. From Lucid, I would like to thank William Fox for his technical advice on the VivaScope 2000. Finally, I would like to thank my mother Julinha, sister Carlita, and wife Vannou for all their love and support through out the years.

Jose Goncalves Barbosa

Northeastern University
December 2004

ABSTRACT

Non-melanoma skin cancers are more common than all other human cancers. It is imperative to develop methods that enable effective detection and delineation of these tumors. In this study we evaluated the use of multi-spectral confocal microscopy for localization of exogenous contrast agents in the cells of non-melanoma skin cancer. An *ex-vivo* confocal microscope has been modified for multi-wavelength imaging (620-690nm and 830nm). The Coherent 399 Dye laser was used to provide visible light in the range of 620-690nm and diode lasers were used to provide 660nm and 830nm light. Thick, freshly excised skin samples with basal cell carcinoma and squamous cell carcinoma were imaged using the multi-wavelength confocal set-up. The measured resolutions with a water immersion 20x, NA 0.75 objective lens were 5-8μm axial, 1.2μm lateral for red light and 7-8μm axial, 1.2μm lateral for the 830nm source. This allowed optical sectioning comparable to histology (typical 5um thick) and horizontal imaging of the skin cells. The confocal images have a field of view of about 600x800μm for a single image; mosaics of the samples were created using 144 images for macro viewing of the samples. Contrast agents, including aqueous solutions of methylene blue (MB) and toluidine blue (TB), were applied to excised skin to enhance the contrast of the tumor in the image, while 3% acetic acid was employed to increase the scattering from cell nuclei in the excised tumor samples. MB and TB exhibit strong absorption in the range from 550nm-690nm. Therefore confocal imaging using the light of 620-690nm allows localization of these dyes. The 830nm light is outside the absorption band of the dyes and allows imaging deeper in the tissue. To optimize contrast and signal, different dye concentrations of MB and TB were tested. Multi-spectral confocal microscopy may

prove to be a useful tool for the detection of contrast agents in non-melanoma skin cancers.

Table of Contents

List of Illustrations

List of Tables

1. Introduction

The development of optical imaging modalities including reflectance confocal microscopy and multi-spectral polarized light macro-imaging have led to the introduction of new techniques that may become viable alternatives to the existing methods of skin tumor detection and demarcation. In the case of non-melanoma skin cancer (NMSC), it is useful to apply tumor specific optical contrast agents in order to enhance the contrast of a lesion with respect to the healthy tissue. Phenothiazinium dyes such as methylene blue (MB) and toluidine blue (TB) are retained by tumors and rinse from healthy tissue. Methylene blue and toluidine blue increase absorption at specific wavelengths, thus allowing spectral selectivity. A contrast agent that increases scattering from cell nuclei is acetic acid. Acetic acid increases scattering over the entire spectral range. These contrast agents so far have been tried separately in confocal microscopy (acetic acid) and multi-spectral imaging (MB and TB) [Rajadhyaksha 2000 and Yaroslavsky].

For this research project, confocal microscopy and multi-spectral imaging have been combined for the detection and localization of basal cell carcinoma and squamous cell carcinoma in excised skin samples using contrasts agents such as methylene blue, toluidine blue, and acetic acid. The development of a new method and equipment, multi-spectral confocal microscopy, for the precise localization and delineation of non-melanoma skin tumor margins was proposed. The Lucid VivaScope 2000 confocal microscope was modified for multi-wavelength operation and to become a flexible research tool. Images were acquired at different wavelengths with the multi-spectral confocal microscope and were compared with each other and histology. Localization of the dyes retained by the tumor was possible with multi-spectral confocal microscopy.

1.1. Objective

The specific aim of the project was to develop a new method to localize and delineate non-melanoma skin cancer for assistance in guiding tumor excision surgery, specifically Mohs micrographic surgery (MMS). The project takes advantage of existing equipment and techniques used at Wellman Labs, Lucid VivaScope 2000 and tumor staining. To achieve this goal two complimentary objectives were employed.

- Expand the capabilities of the commercially available Lucid *ex-vivo* VivaScope 2000 to operate at wavelengths between 620nm – 690nm and the existing 830nm laser. The additional light source emitted within the absorption band of MB and TB, which allowed the localization for these dyes. The 830nm light source emitted out of the absorption band of these dyes, which was used for comparison to the 620nm – 690nm images. The operator is able to select a wavelength from 620nm – 690nm imaging and 830nm imaging of excised tumor samples without having any impact on the sample.
- Optimize and select the contrast agents on a basis of comparative evaluation. Contrast agents concentration and stain/rinse time were optimized to improve contrast for the multi-spectral confocal microscope.

To implement these objectives the Lucid VivaScope had to be modified and experiments with variations in the tissue staining process were conducted.

1.2. Overview

The following chapters contain background, instrument detail, analysis, and data collected, which reflect the work done on this project. Chapter 2 discusses the background of non-melanoma skin cancer, confocal microscopy, multi-spectral imaging,

and contrast agents being used. Chapter 3 discusses the growing concerns of non-melanoma skin cancers and the medical significance of multi-spectral confocal microscopy. Chapter 4 describes the modifications made to the Lucid VivaScope 2000 *ex-vivo* confocal microscope and examines the components added. Chapter 5 describes the light path and reports on the calculated and measured lateral and axial resolution. Chapter 6 discusses the materials and methods used to image the excised tumor samples. Chapter 7 shows the results of the *ex-vivo* multi-spectral confocal microscope and compares the images which each other and histology. Finally Chapter 8 includes the conclusion and future work.

2. Background

2.1. Non-melanoma Skin Cancer

Exposure to ultraviolet radiation at solar wavelengths of 280-320nm (UVB) and 320-400nm (UVA) is carcinogenic and responsible for 90% of non-melanoma skin cancers [Strasswimmer]. Other carcinogens are ionizing radiation, aromatic hydrocarbons (coal tar, asphalt, cutting oils), arsenic, smoking, and alcohol [Strasswimmer]. The UV energy absorbed by chromophores in the skin causes a series of photochemical reactions, which may lead to photodamaging of skin cells. The photodamaged cells can have DNA mutations and oxidative stress that alter the function of the cells [Pinnell]. The body is equipped to defend itself again UV damage and mutated cells. Melanocytes in the basal layer create melanin, the protein which adds pigment to skin. Melanin works its way into the keratinocytes as they move from the bottom layer of the epidermis to the top layer of the epidermis. Melanin protects the cells

from UV radiation by absorbing UV energy, preventing the UV radiation from penetrating into the body. The body protects itself from oxidative stress by naturally using antioxidants to lessen cell changes [Pinnell]. Although the body is equipped with defenses, chronically exposed and excessively exposed sites may develop skin malignancies.

Non-melanoma skin cancer includes basal cell carcinoma (BCC) and squamous cell carcinoma (SCC), occurring at the basal cell layer and squamous cell level of the epidermis. Figure 2-1 illustrates the two layers of the skin, the epidermis (50-100μm thick) and dermis (1-3mm thick). About 80% of all skin cancers are basal cell and 17% are squamous cell carcinoma [Weinstock]. These cancers usually develop on sun-exposed areas of the body, commonly on the face, ear, neck, lips, and back of hands. Basal cell carcinoma tends to grow slowly and has a metastatic rate of 0.0028% to 0.55% [Strasswimmer]. Histologic types of basal cell carcinoma are nodular, superficial, micronodular, infiltrative, and morpheaform. Invasive growth patterns that have infiltrating strands of tumor that can extend well into the tissue can be seen with morpheaform and infiltrative BCCs. Squamous cell carcinoma tends to grow rapidly and has a 2% to 6% rate of metastasis [Martinez and Otley]. Variants of squamous cell carcinoma include Bowen's disease [Strasswimmer], erythroplasia of Queyrat (SCC-*in-situ* on the penis) [Tsao], cervical intraepithelial neoplasia [Tsao], and squamous intraepithelial neoplasia [Tsao]. Melanoma skin cancer has an incident rate of 3% [Weinstock] and has a much higher mortality rate, therefore it is treated differently and is not the target of this project.

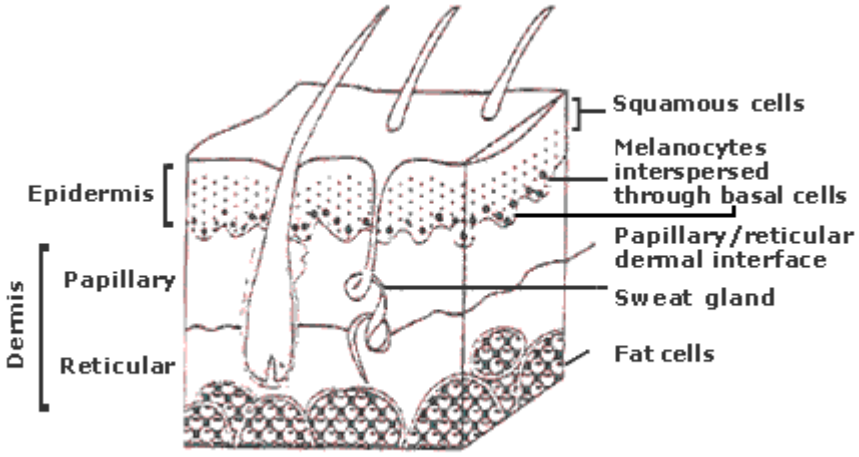

Figure 2-1. The skin layers [CDC].

The type of treatment for non-melanoma skin cancers depends on many indicators, one of them being whether the tumor is high risk or low risk, defined as the likelihood of a tumor recurring or metastasizing. The factors that determine if a tumor will recur or metastasize are location, size, borders, and type of tumor. The types of treatment are cryotherapy (freezing), electrodessication and curettage (scrape and burn), excision, Mohs micrographic surgery, and radiation. High risk aggressive tumors are normally treated by Mohs micrographic surgery, radiation therapy, and excision surgery. The face, ears, and scalp are areas where recurrence and metastasis are more likely; therefore, cancers in these locations are generally classified as high risk [Martinez and Otley]. For excision treatment, Mohs micrograph surgery insures the highest cure rate and conservation of normal skin tissue. The visible tumor lesion is excised, carefully mapped through histology, and examined microscopically. If there is still cancer seen on the excised margin from histopathologic examination, another very thin layer of skin is excised from that exact location on the patient. This procedure may be repeated as many times as necessary to completely remove the tumor. Mohs surgery is not always the

treatment of choice because it is complex, expensive, and time consuming. Also patients have to be referred to a Mohs surgeon by their physician and the referral process may be influenced by the patient and referring physician. Mohs referral studies have been conducted by the Mayo Clinic, the Brooke Army Medical Center, and the University of Missouri. It was found that the percentage of NMSC referred for Mohs Micrographic surgery is about 30% [Gaston]. However, Mohs Micrographic surgery offers the greatest cure of difficult tumors and has the best cosmetics results.

2.2. Confocal Microscopy

2.2.1. Brief History and Applications

Harvard University postdoctoral fellow Marvin Minsky patented a stage scanning confocal microscope in 1957 [U.S. Patent No. 3013467]. The conventional microscope condenser was replaced by an identical objective lens, with a pinhole to limit the field of illumination, and an exit pinhole to restrict the field of view. A specimen could be imaged by trans-illumination or epi-illumination (reflectance). Since it uses point source illumination and point source detection the specimen must be scanned. The advantages are reduced blurring, increased resolution, improved signal-to-noise ratio, and the capability to optically section volume specimens. The advantages are discussed in the sections following. The disadvantages are that scanning optics and electronics are needed to image a specimen. Over the years scanning technology has been well developed and is commercially available. There are stage scanners in which the optics are fixed and the object is moved, disk scanners in which the position of the source and detector conjugates are moved, and laser beam scanners in which the laser beam is moved in a raster pattern [Stelzer]. Raster scanning like that of a television requires a

fast scan in the horizontal direction and a slow scan in the vertical direction. Laser scanning confocal microscopes can rapidly image surface sections, and with the addition of an axially moveable stage relative to the objective lens axial sections can also be imaged. Advances in laser technology such Gaussian beam profile, monochromaticity, small divergence, miniaturization, stability, clean mode, and wavelength availability have also made confocal microscopy more readily implemented.

Applications of the confocal microscope range from CD players to a variety of biomedical imaging. The ability to image a plane at high resolution without the presence of out-of-focus light from surrounding planes has many advantages. Depth discrimination is very useful when detailed topological information is needed from a volume specimen, whether it is an integrated circuit or biological tissue. In the field of biomedicine, human or animal tissue may be imaged non-invasively *in-vivo* or *ex-vivo*. Cellular, nuclear, and morphologic details can be imaged in their native state [Rajadhyaksha, 2003] with high lateral and axial resolutions of about 1μm and 3μm respectively [González, 2001]. A reflectance laser scanning confocal microscope (LSCM) has been used to image rat bladder tissue [Koenig], human oral mucosa [White], and human tissue [Rajadhyaksha, April1999] *in-vivo*. Confocal images of normal skin and inflammatory skin conditions have been compared with histopathology. The correlation with histology of corneocytes, granular cells, keratinocytes, blood vessels, and collagen bundles were studied [Rajadhyaksha, Sept 1999]. Skin lesions such as allergic contact dermatitis [Gonzalez, May 1999], psoriasis [Gonzalez, 1999], and non-melanoma tumors [Rajadhyaksha, 2000] were imaged and compared to histology.

Confocal imaging may be either reflectance or fluorescence. Contrast in the reflectance mode is due mainly to the variations in index of refraction in the tissue [Dunn, 1996]. In the fluorescence mode the contrast is from endogenous (native) or exogenous (administered agents to label tissue microstructures, topically or through intravenous injection) fluorophores [Rajadhyaksha, 2003]. Fluorescence confocal images of microcirculation in rat brain cortex, rabbit bone, cellular morphology in mouse skin, and rat kidney have been noted by Rajadhyaksha and Gonzalez in "Real-time *in-vivo* confocal fluorescence microscopy". Fluorescence confocal images are more specific to tissue microstructure and function; the fluorescence is limited to the plane in focus. Therefore, there is a growing interest in fluorescence confocal microscopy. In the field of dermatology, confocal microscopy has been used to study different normal skin and pathological skin conditions the results proved confocal microscopy to be a useful tool for diagnosis.

2.2.2. Principle of Operation

The basic components of a confocal microscope are a point light source, objective lens, pinhole, and detector. The point light source, point illumination on the object, and point image at the detector are all conjugate. The point source is imaged at the focal point on the object and the detector, limited to a point by the pinhole, is also imaged at the focal point on the object. The light source generates light that is brought to a focus on the object by a condenser or objective lens. The focused light on the object is transmitted or reflected onto an objective lens (same objective in reflectance mode) and brought to focus on the detector. The detector registers only light that is focused on the focal plane of the object. Photons from the light source will also illuminate other parts of the object,

but will be rejected by the pinhole. These basic components operate in a confocal microscope to provide optical sectioning; other components are for scanning and optimization. Refer to Figure 2-2 and Figure 2-3 for an illustration of transmitted illumination and epi-illumination configuration.

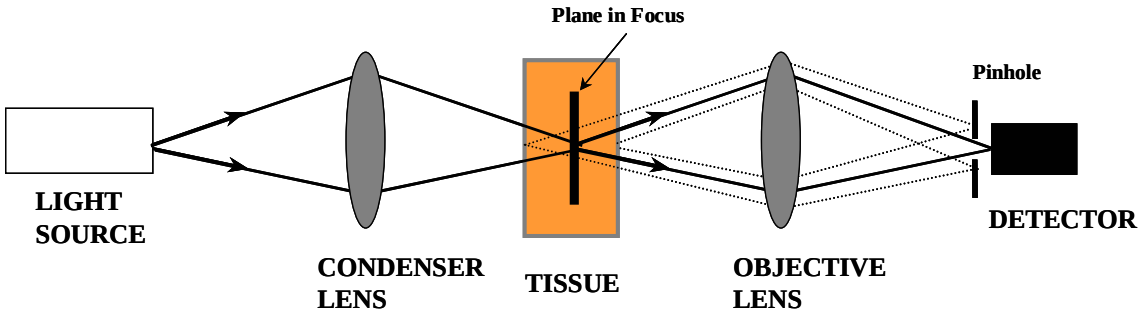

Figure 2-2. Transmitted illumination configuration. The solid line is the in-focus light that is registered by the detector. The dashed lines are out-of-focus light that is rejected by the pinhole in front of the detector. [Wilson].

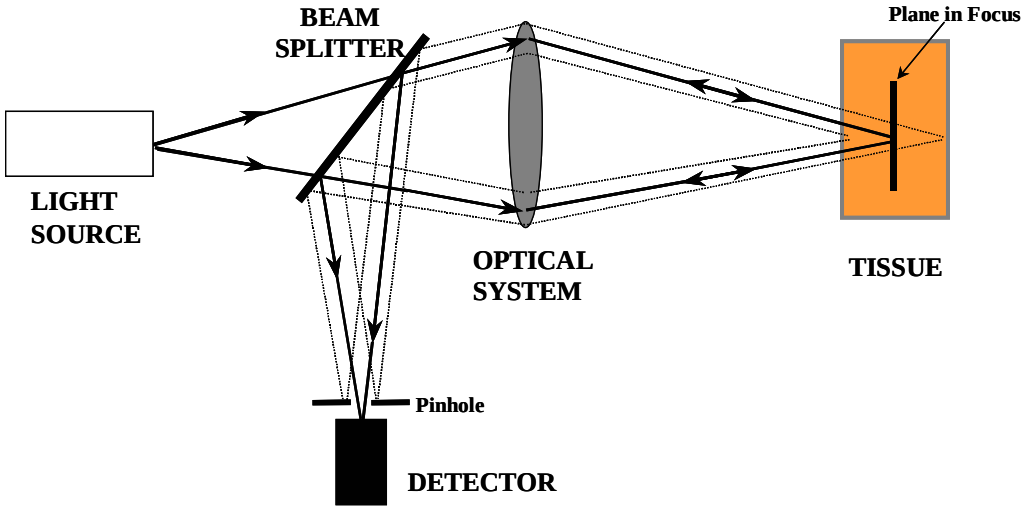

Figure 2-3. Epi-illumination (reflected) configuration. The solid line represents the optical path of the in-focus light and dashed lines are the out-of-focus light. The pinhole rejects out-focus-light and the in-focus light is registered by the detector. [Wilson].

A well-collimated laser source acts as a point source at negative infinity. Lasers are also coherent (monochromatic and matching wavefronts) and have high radiance. Conventional microscopes generally use incoherent illumination. Coherent plane

illumination may cause dark spots in the image (speckles) due to interference effects. In the laser scanning confocal microscope a focused beam is moved across the object, hence speckles are minimized (not present at low magnification) in the confocal image because of single spot illumination and detection. The image is composed of light intensity levels from different illuminated points at different times on the object. When two or more reflective surfaces are within the illuminated point they may cause spatial variations in the wavefront that can lead to constructive or destructive interferes on the detector. This will increase or decrease the detected intensity and may cause interference fringes on the scanned confocal image [Smithpeter, Cheng].

2.2.3. Resolution

The human eye cannot resolve objects smaller than 10μm and to visualize structural details clearly magnification is required. The purposes of a microscope are to first resolve details and then to magnify. The resolving power of a microscope is the ability of the microscope to see the smallest detail in an object and depends on the microscope components [Rajadhyaksha, microscopy tutorial]. Resolution is the smallest detail in an object that can actually be seen depending on the properties of the object and image system [Rajadhyaksha, microscopy tutorial]. The main components of concern in our confocal system that affect the resolution of the confocal microscope are the illumination source, objective lens, contrast, and pinhole diameter. The three dimensional illumination spot size formed by the objective lens quantifies the resolution. Lateral resolution is the size of this spot in the transverse plane (x-y) and axial resolution is the size of this spot along the optical axis (z).

Illumination source. The illumination source has to be well-collimated to simulate a point source at negative infinity. The Abbé sine condition states that

$$n_o y_o \sin\alpha_o = n_i y_i \sin\alpha_i \qquad (2.1)$$

where n, y, α are the index of refraction, height, and divergence respectively. The 'o' indices are for the source and the 'i' indices are for the image of the source. The illumination spot produced by the objective lens cannot be better than the illumination point source. Setting the object and image medium equal and assuming paraxial conditions we see that the transverse magnification is constant.

$$M_T = \frac{y_i}{y_o} = \frac{\alpha_o}{\alpha_i} = \text{constant} \qquad (2.2)$$

From the equation above we see that the height of the illumination spot depends on the height of the point source. The smaller the point source the smaller the focal spot the objective lens can produce, depending on the wavelength and numerical aperture of the objective lens.

Objective lens. The objective lens is the most important element in a microscope system. The objective lens determines the magnification, the field of view, the resolution, and contains optical components to correct for aberrations. Some specifications of the objective lens are the working distance, numerical aperture (NA), dry or immersion media, and cover slip thickness. The working distance is the distance from the surface of the objective lens to the focal point. When used with the proper immersion medium (usually water or oil) and cover slip thickness the performance of the objective lens is optimized, aberrations are minimized. The NA describes the angular behavior of the

light cone, which determines the resolution of the objective lens. Figure 2-4 shows the irradiance distribution at the focal plane and along the optical axis. The larger the NA the more confined the focal spot.

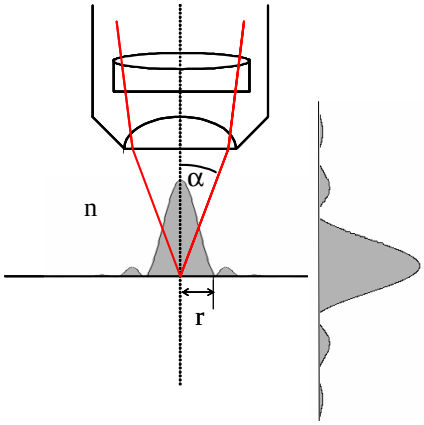

Figure 2-4. Horizontal and vertical intensity distribution along the focal plane and optical axis [Webb].

The NA is the sine of the half angle multiplied by the index of refraction of the media and can be related to the f/# by the equation below.

$$NA = n \cdot \sin(\alpha) \qquad f/\# = \frac{n}{2NA} \tag{2.3}$$

When the entrance aperture of the objective lens is uniformly illuminated (overfilling the entrance aperture) a diffraction pattern is observed at the focal point. The irradiance distribution (W/m^2 incident upon a region) is called the "point spread function" (PSF) of the lens [Cogswell]. The dimension of the point spread function to the first dark ring defines the resel, the lateral and axial resolution elements [Webb]. For a circular aperture the transverse irradiance has an Airy pattern distribution. For small NA a good approximation for the distribution is

$$\left(2\frac{J_1(\rho)}{\rho}\right)^2 \tag{2.4}$$

for the conventional microscope and

$$\left(2\frac{J_1(\rho)}{\rho}\right)^4 \tag{2.5}$$

for the confocal microscope because both the condenser and objective perform imaging and the response is the product of the two lenses' PSF [Wilson, 1990], where

$$\rho = \frac{2\pi}{\lambda}\cdot r \cdot NA \tag{2.6}$$

is a normalized optical unit coordinate [Webb 1996, Born and Wolf]. The zero crossings are the same, but the center peak is sharper for the confocal case. The distance from the center peak to the first dark ring occurs when $\rho = 1.22\pi$ for the first order Bessel function. In terms of the NA and wavelength the radial distance is

$$r = 0.61\frac{\lambda}{NA}. \tag{2.7}$$

For the axial irradiance distribution along the optical axis for small NA the pattern is a sinc function squared.

$$\left(\frac{\sin(\zeta/4)}{\zeta/4}\right)^2 \tag{2.8}$$

for the conventional microscope and

$$\left(\frac{\sin(\zeta/4)}{\zeta/4}\right)^4 \tag{2.9}$$

for the confocal microscope [Wilson, 1990], where

$$\zeta = \frac{2\pi}{n\lambda}\cdot z \cdot NA^2 \tag{2.10}$$

is a normalized optical unit coordinate [Webb 1996, Born and Wolf]. Again the center peak is sharper in the confocal case. The zero crossing occurs at $\zeta/4 = \pm\pi$. In terms of the NA and wavelength the axial distance is

$$z = \frac{2n\lambda}{NA^2} \qquad (2.11)$$

where n is the index of refraction. The lateral and axial resel can be defined by equations 2.7 and 2.11. They satisfy the Rayleigh criterion which state that two points are resolvable if the first principal intensity maximum of one coincides with the first intensity minimum of the other. For the lateral resolution there is a 26.5% dip between adjacent peaks one resel apart (see Figure 2-6) and for the axial resolution at the mid point there is $8/\pi^2$ of the maximum (18.9% dip). The confocal point spread function has a sharper peak, to get the same 26.5% dip in the lateral and 18.9% dip in the axial between adjacent peaks equations 2.12 and 2.13 are used ($\rho = 2.77$ and $\zeta = 9.1$). For incoherent and uniform illumination the lateral and axial resolutions are

$$\Delta r = \frac{0.44\lambda}{NA} \qquad (2.12)$$

and

$$\Delta z = \frac{1.4n\lambda}{NA^2} \qquad (2.13)$$

respectively [Rajadhyaksha, April 1999, Corle, Webb1995]. The PSF reflects the NA of the objective and is the “diffraction-limited” spot. The NA is important because it determines what can be resolved. In Figure 2-5a the lines cannot be resolved since the illumination spot is too larger as opposed to Figure 2-5b where the lines are easily resolved by scanning.

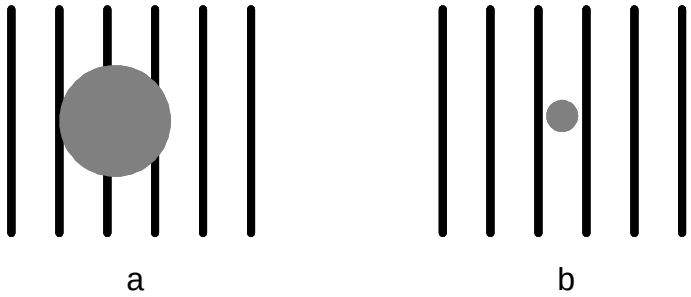

Figure 2-5. The focal spot cannot resolve the bar lines (a). The bar lines are easily resolvable by scanning (b).

Two closely spaced points can be resolved if they meet the Raleigh criterion. The Raleigh criterion is the most commonly used definition to set the minimal resolvable distance between two adjacent points. The minimal distance is met when the peak of one diffraction irradiance distribution coincides with the first dark ring of the second diffraction irradiance distribution if the same PSFs are observed.

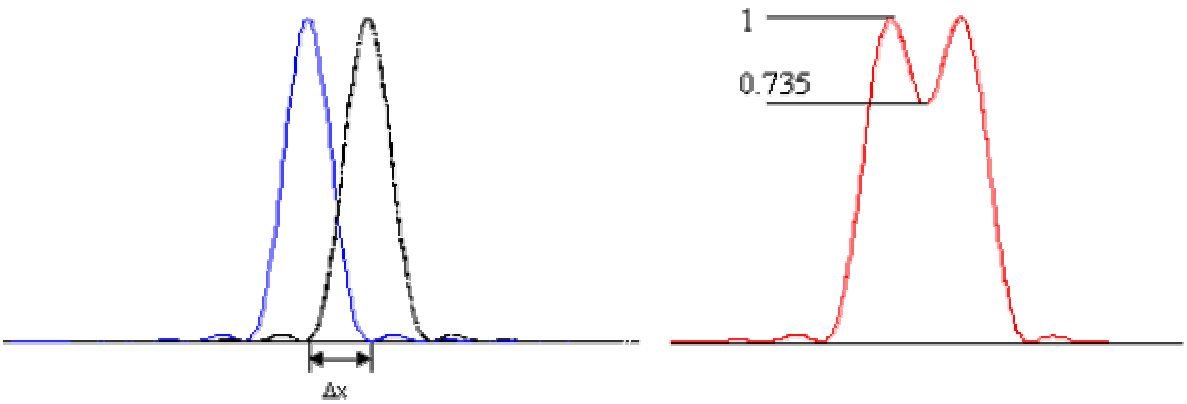

Figure 2-6. Minimum distance in order to resolve two Airy patterns produced by two points (left) and the sum on the intensity patterns (right). There is a 26.5% dip between the adjacent Airy disks.

Contrast. Two points illuminated by the same wavelength and separated by one resolution element, resel, are resolvable according to the Rayleigh criterion. This holds true if the two peak intensities can be relatively distinguished from one another (100%

contrast, white on black). The two points may not be resolvable if the difference in brightness and noise prevent a noticeable dip between the two points or cannot be seen as two separate Airy disks. The intensity differences are due to contrast in the object. Contrast is the difference in signal strength between different points in an object or the object of interest with the background [Cheng and Kriete]. The interaction of light with the specimen gives contrast to images. This interaction may include absorption, fluorescence, refraction, reflection, scattering, or change in polarization [Cheng and Kriete]. Confocal images tend to have high contrast because background light is rejected, the high lateral and axial resolution, and the sharper peak of the 3-D PSF. Noise in the image may come in the form of electronic noise or optical noise (aberration or misalignment) and will have an impact on the image resolution. Some of the noise is reduced by the image acquisition system by averaging the frames to producing a better overall image.

Pinhole. The difference between the confocal laser scanning microscope and a conventional scanning microscope is that the confocal microscope uses a point detector rather than a wide field detector [Wilson, 1995]. As the pinhole size increases the optical sectioning disappears and the axial resolution becomes that of a conventional microscope. The resolution limit as the pinhole size decreases becomes that of the objective lenses' PSF and no further improvement is gained for smaller pinhole sizes of less than 1 lateral resel [Webb, 1996]. The size of the pinhole also determines the amount of light detected. The lateral resolution is more sensitive to pinhole size than the axial resolution [Wilson, 1995, Webb 1996, and Rajadhyaksha, Sept 1999]. Acceptable images can still be

obtained using pinhole diameters greater than that of the pinhole diameter to obtain true confocal images. This would allow for more light to enter the detector at the sacrifices of a slight decrease in resolution. To obtain optimal sectioning the pinhole diameter can be calculated from

$$\frac{M}{NA} \geq \frac{\pi d_o}{2.5\lambda} \qquad (2.14)$$

where d_o is the pinhole diameter and M is the magnification [Wilson, 1995].

2.3. Multi-Spectral Imaging

Spectroscopy may reveal certain properties or attributes not initially obvious in a spatial image. Spectroscopy usually uses point measurements, but the combination of spectral and spatial information is even more useful. Spectral images are collected at either contiguous narrow wavelengths (Hyper-spectral) or at selected wavelengths (Multi-spectral) depending on the absorption band(s) of the specimen. The images can be analyzed as shown in

Figure 2-7 as a function of wavelength. This technique allows for the detection of absorbing chromophores and/or the fluorescence of fluorophores in a specimen. *In vivo* fluorescence spectroscopy has been used for the detection of non-melanoma skin cancers [Wennberg, Brancaleon]. Spectral images have been used in military and commercial applications in remote sensing, ocean imaging, agricultural, medical, and a growing list of others [Barbosa]. As a medical tool, spectral reflectance of biological tissue has been used in the diagnosis of non-melanoma skin cancer [Yaroslavsky] and monitoring of blood flow for the oxygenation of hemoglobin [Dwyer].

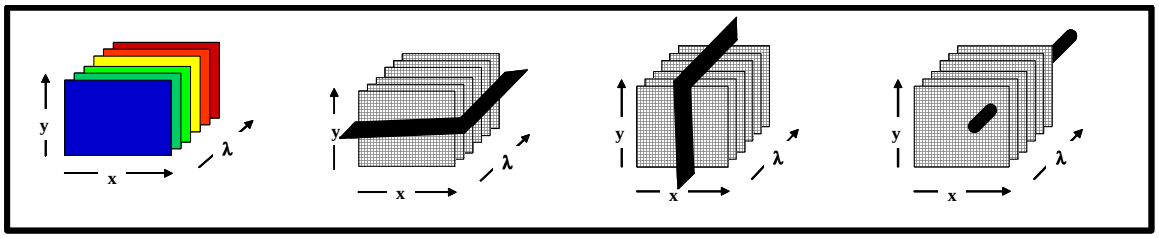

Figure 2-7. Spatial spectral data is analyzed as a function of wavelength by either one image at a time, as a horizontal line, vertical line, or pixel intensity.

2.4. Contrast Agents

The quality of an image depends on resolution, the resolving power of the system and contrast. Biological substances may be transparent and therefore lack absorptive contrast to resolve borders and sub-cellular details. Refractive index changes cause light scattering and reflectance which provides an alternative mechanism for contrast. In histopathology of non-melanoma skin cancer, the excised lesion is mainly stained with hematoxylin and eosin which stain cells purple and collagen pink, to increase contrast. There are tumor specific contrast agents which enhance contrast with respect to healthy tissue. Phenothiazinium dyes such as methylene blue and toluidine blue are retained by tumor and rinse from healthy tissue. Mitochondria organelles in the cells uptake these dyes. Carcinoma cells contain a large amount of mitochondria compared to healthy cells, therefore the dye uptakes in the cancer cells are greater and more is retained after rinsing. These dyes absorb light in the 550-700nm wavelength range, giving the tumor a shade of blue. The imaginary part of the index of refraction is increased in the 550-700nm range in the tumor. This is out of the absorption band of melanin and hemoglobin in the skin, which both have a maximum absorption centered at around 400nm. Figure 2-9 shows the

absorption curves for MB, TB and dermis with 2% blood. Methylene blue has been approved for human use. It has been used to stain bladder carcinoma [Gill, Kaisary], columnar epithelium in Barrett's esophagus *in-vivo* [Canto], and in the localization of islet cell tumors of the pancreas [Fedorak]. Toluidine blue has been used as an oral rinse in the delineation of tumor tissue of patients with oral carcinoma [Niebel], topically used to detect cervical carcinoma [Richart], and has also been used to stain carcinoma for histopathology during Mohs surgery [Humphreys]. The dyes have been shown to stain non-melanoma skin cancer on fresh excised lesions and used for the demarcation of tumor margins using a multi-spectral polarized light imaging system [Yaroslavsky]. These dyes have demonstrated their carcinoma-staining capability and at the same time have been spectrally resolved in skin cancer. MB and TB have similar chemical structures (Figure 2-8) and have similar physicochemical properties.

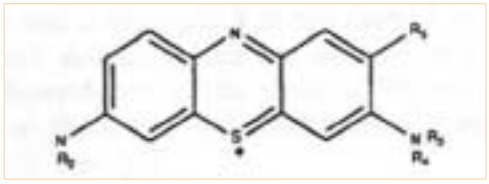

Figure 2-8. Chemical structures of methylene blue (MB^+) : $R_1=R_2=R_3=R_4=CH_3$, $R_5=H$; and toluidine blue (TB^+) : $R_1=R_2=R_5=CH_3$, $R_3= R_4=H$. [Yaroslavsky]

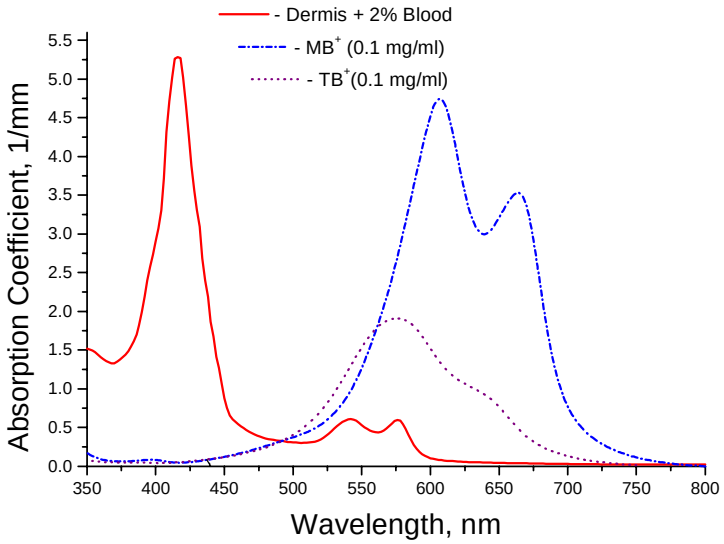

Figure 2-9: Absorption of TB, BM, and dermis with 2% blood. [Yaroslavsky]

Acetic acid is a contrast agent that increases scattering from cell nuclei. Rinsing tissue in acetic acid increases the back scattered light in confocal microscopy giving the nucleus a brighter appearance. Monte Carlo simulations predict that changes in the index of refraction are the largest source of contrast in confocal microscopy [Dunn, 1996]. Smithpeter and Zuluaga have used phase contrast images to show that after the addition of acetic acid there is an increase in index fluctuations in the nucleus, which results in more scattering and hence more signal from the nucleus in confocal microscopy. Acetic acid alters the chromatin structure in the nucleus and it is hypothesized that acetic acid causes crosslinking between proteins in the nucleus [Smithpeter]. Acetic acid has been used to increase backscatter from cell nuclei of BCC and SCC in confocal microscopy [Rajadhyaksha, 2000] (making cells more visible in the dermis and epi-dermis) and in the imaging of cervical cancer cells [Zuluaga].

3. Significance

Non-melanoma skin cancer is the most common form of human skin cancer. In the United States more than 1 million new cases of basal cell carcinoma and squamous cell carcinoma are reported each year [American Cancer Society]. The incidence of skin cancer is increasing each year. This may be due to an increase in outdoor activities, new fashions that are less protective, and inadequate sunscreen protection. Skin cancer on women's legs is more common due to new fashions that cover less skin [Strasswimmer]. Sunscreen users are not protected as well as they may believe. The protection indicator on sunscreens is measured for a topical application of 2 mg of sunscreen per square centimeter. The sunscreen user on average applies only $0.5mg/cm^2$ or less [Autier]; this reduces the effective sun protection factor (SPF) number drastically (see Table 3-1). The SPF is a measure of energy needed to trigger erythema (sunburn) with sunscreen compared to without sunscreen. For example a person using $2mg/cm^2$ of SPF 10 sunscreen could be exposed to the sun 10 times longer than a person without sunscreen before any visible signs of erythema are noticed for both persons having equivalent skin sensitivity. Erythema is a result of UVB (280-320nm) radiation. Sunscreens are therefore graded on their ability to protect against UVB radiation and not for UVA (320-400nm) radiation [Gasparro]. Sunscreens do not provide full protection across the full UV spectral and give sunbathers a false sense of protection that may result in prolonged sun exposure. These factors contribute to the increase of new cases of skin cancer each year.

SPF	2.0mg/cm^2	1.5mg/cm^2	1.0mg/cm^2	0.5mg/cm^2
2	2	1.7	1.4	1.2
4	4	2.8	2.0	1.4
8	8	4.8	2.8	1.7
15	15	7.6	3.9	2.0
30	30	12.8	5.5	2.3
50	50	18.8	7.1	2.7

Table 3-1. Photoprotection from sunscreens at different application concentrations. [Pinnell SR]

With the increase of new cases of non-melanoma skin cancer there is a need to improve the treatment process by reducing cost, increasing efficiency, and reducing any patient anxiety. For surgical excision treatment, Mohs micrographic surgery offers the highest cure rate and significantly spares healthy tissue. Mohs surgery is performed after diagnosis from biopsy pathology. Mohs surgery involves the removal of the tumor lesion, color coding the tissue edges for mapping, fixing and freezing the tissue, slicing the tissue into thin sections, staining with hematoxylin and eosin, placing the tissue between a slide and cover slip, and finally viewing under a microscope. If there is still tumor seen on the excision margin under a microscope, another thin section is removed from the patient until there are tumor free margins seen under the microscope [Steinman and Gross]. During this time between excisions and histopathologic diagnosis, the patient is waiting with an open wound and under local anesthesia. A trained Mohs surgeon, a technician to prepare histopathology sections, and a specialized laboratory are needed to perform Mohs micrographic surgery accurately and precisely. Because Mohs surgery is complex, time inefficient, and expensive, it is sometimes not the treatment of choice even when indications suggest Mohs surgery. Faced with an increasing rate of

skin cancer incidents, it is imperative to reduce the cost and time associated with Mohs micrographic surgery and to overall improve the quality of care for skin cancer patients.

Multi-spectral confocal microscopy may prove to become a viable alternative to existing methods of tumor detection and demarcation. Multi-spectral confocal microscopy can assist Mohs surgery by providing rapid and precise localization and delineation of non-melanoma skin cancer margins. The confocal microscope can optically section tissue with high axial resolution (section thickness) about 3-5μm, which is comparable to histopathology which typically has a section thickness of 5μm, and optically resolve structures with lateral resolution of about 1μm. Confocal microscopy has been shown to image nuclear, cellular, and morphological details *in-vivo* and *ex-vivo*. With the addition of contrast agents that localize in cancer cells and rinse from healthy cells and imaging with a multi-spectral confocal system, the demarcation of tumor margins can be improved. The advantage of a multi-spectral confocal system is the addition of spectral variations to delineate tumor margins. Aqueous solutions of methylene blue and toluidine blue localize in cancer cells and absorb in the red wavelengths of light. Confocal imaging using 620-690nm laser light allows localizations of these dyes. In addition imaging at 830nm laser light, which is outside the absorption band of the dyes, allows for deeper imaging and comparison. The tumor area will image dark at wavelengths between 620-690nm comparatively to the 830nm wavelength image allowing the localization of these dyes in the tumor cells. An additional contrast agent, acetic acid, may be used to increase scattering from cell nuclei to more easily locate cells within the tissue. This technique may lead to the diagnosis of excised tumor tissue during surgery to eliminate the need for histology to guide surgery. Furthermore, it can be

combined with a macro multi-spectral imaging system to increase efficiency in non-melanoma skin cancer localization and demarcation during surgery [Yaroslavsky 2005].

4. Modification to VivaScope

The VivaScope 2000 shown in Figure 4-1 is a laser scanning inverted confocal microscope for the pathological examination of *ex-vivo* tissue. The VivaScope 2000 can image excised surgical tissue at near video rates (10 frames per second) with a lateral resolution of 1μm and optical section thickness between 6μm to 8μm. Optical components used for imaging include a Micro Lasers System Lepton II 830nm diode laser, a Nikon 20x, NA 0.75, Plan Fluor multi-immersion objective lens, and a Hamamatsu C5460 avalanche photodiode (APD) detector. The scanning optics consists of a MRC polygon scanner for the horizontal fast scanner and a General Scanning Inc. galvanometric scanner for the slow vertical scanner. The systems control panel consists of a keyboard with mouse, laser power knob, adjustment knobs for moving the tissue stage, and tissue imaging interface. A computer with a National Instruments IMAQ acquisition card, monitor, VivaScope software, and VivaScope control electronics are used to acquire and display the images. The VivaScope 2000 is a complete clinical confocal microscope ready for use by medical practitioners.

Figure 4-1. Lucid VivaScope 2000 System.

To make the VivaScope 2000 into a flexible research tool with the capability of multi-wavelength operation and ease of accessibility to the optics (for alignment and measurements) the unit was opened. The optics board and control electronic were mounted onto an optical table and modifications were made to the system. The modifications included were: creation of a new stage to replace the existing Lucid tissue cassettes, the addition of two other laser sources, improvement of transmission for 620-690nm wavelength operation, replacement of the avalanche photodiode with a photomultiplier tube, and making the optics easily accessible. The reasons for and details of the modification are discussed in the sections following.

4.1. Additional Laser Sources

To image within the absorption band of MB and TB (see Figure 2-9) an additional laser source was add to the confocal system. Confocal images within the dye absorption band and out of the dye absorption band would be possible by using a red laser source and the existing near infrared 830nm diode laser. The Coherent 599 Dye Laser pumped by the Coherent 100 Argon Laser was used to image in the 620-690 nanometer range.

DCM (4-Dicyanomethylene-2-methyl-6-p-diethylaminostyryl-4-H-pyran) Special laser dye was used for the Coherent 599 dye laser. DCM Special has a lasing range of 606-714nm with a lasing maximum at 642nm and operates at pump excitation of 458-514nm. The Dye laser output wavelength was kept between 620-690nm because the output power beyond this range was not sufficient for imaging. The existing 830nm diode laser was relocated on the optics board to allow room for a sliding mirror to direct the 599 Dye laser beam into the VivaScope optics. Confocal images at 830nm and from 620-690nm were possible. The objective lenses' focal length varies slightly for the different wavelengths. Therefore the object had to be axially adjusted to be in the same imaging plane for the different wavelengths. The depth of imaging is deeper for 830nm imaging compared to 620-690nm imaging, since longer wavelengths travel deeper in tissue. See Figure 4-2 for a drawing of the optics layout.

The 830nm power can be adjusted from 0 to 115mW by the controls on the VivaScope. The dye laser power can reach 200mW by increasing the Argon pump's current. The power delivered to the VivaScope from the dye laser is not the maximum power the dye laser can produce. The power is attenuated by the use of mirrors to guide the beam into the VivaScope optical path. The beam propagating out of the dye laser is s (vertically) polarized and optics are needed to rotate the state of polarization to p polarized. Finally, there is additional loss because the optics on the VivaScope was optimized for 830nm wavelength operation. The coatings on the lenses are unknown, the quarter wave plate is for 830nm operation, and the beam splitter cube is for 830nm. Using the 830nm diode laser, the measured power after the objective lens was found to be15mW at 115mW output power. Most of the loss comes from overfilling the objective

lens. In order to image, power delivered to the tissue would have to be in the range of 15mW, which is possible with the Dye laser.

Another laser source was later added to the system after the existing detector was replaced by a more sensitive detector, see section 4.3. A Micro Laser Systems Lepton II 660nm diode laser was put into the system. The 660nm diode laser was mounted on a XYZ translation stage that could be moved into the optical path of the Dye laser beam, which follows into the VivaScope optics. This would allow imaging with 830nm diode laser light, 660nm diode laser light, and 620-690nm Dye laser light. The 660nm diode can be adjusted from 0 to 40mW by increasing the driver current. The Dye laser or the 660nm diode laser beam could be directing into the system using mirrors, see Figure 4-2 below.

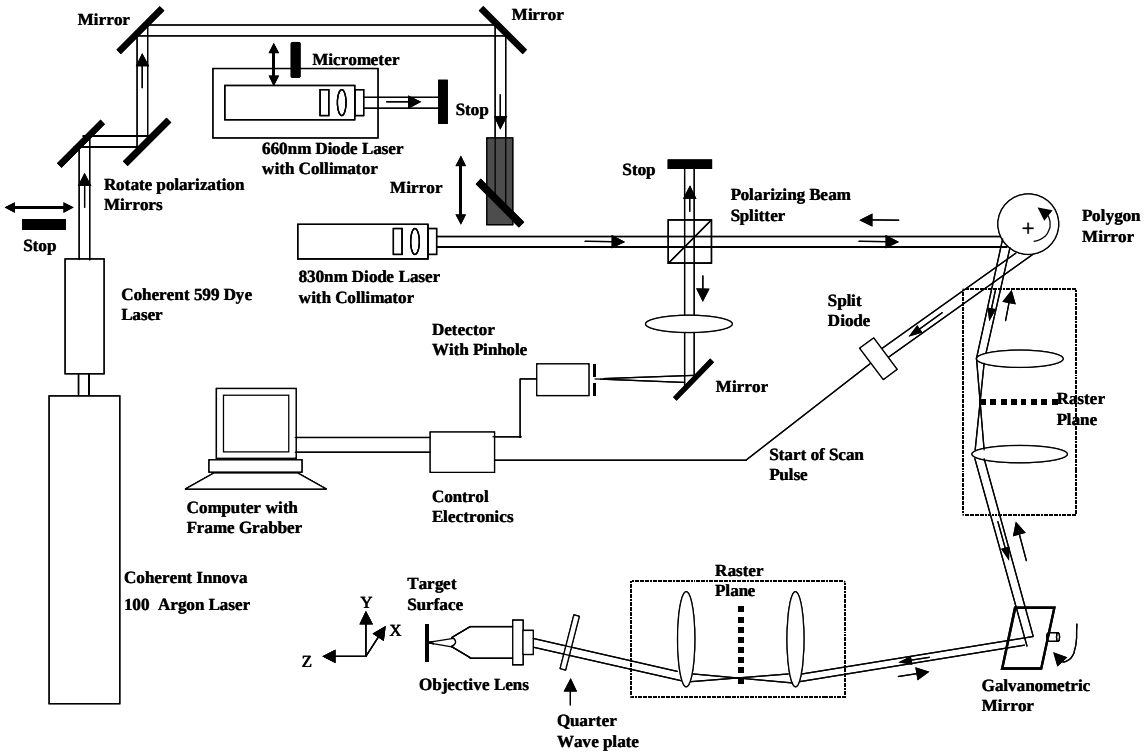

Figure 4-2. Layout of the multi-spectral confocal system.

The beam characteristics of the 660nm diode laser are similar to the 830nm diode laser except the 660 diode laser's beam diameter was requested to be 5mm. The 830nm diode laser beam is elliptical with axes of 4mm and 6mm. The 660nm diode laser is moved into the optical path of the 599 Dye Laser light when the operator wants to image using the 660nm diode laser. The beam characteristics of the two diode lasers are better than the Dye Laser's beam characteristics, but the dye laser delivers more power than the 660nm diode laser.

The characteristics of the three lasers were profiled using Spiricon Laser Beam Diagnostics software with the Cohu 4812 CCD camera. The laser beams were attenuated by neutral density filters mounted in front of the camera. The attenuated laser beams were captured and processed. Each beam's profile was plotted, the diameter was measured, and the divergence was calculated using the Spiricon software and making measurements at two different points by moving the camera. The results are shown below in Table 4-1 and

Table 4-2.

Model and Manufacture	λ (nm)	Max Power (mW)	Diameter (mm) Horiz	Vert	Divergence (mrad) Horiz	Vert
Micro Laser System L2 830S-115	830	115	5.592	4.142	0.116	0.540
Micro Laser System L2 660S-40	660	40	5.45	5.85	0.073	0.095
Coherent 599 Dye	630	200	2.00	1.67	4.93	9.25

Table 4-1. Laser sources and their beam characteristics used for multi-spectral confocal imaging.

	L2 830S-115	L2 660S-40	599 Dye (630nm)
Top View	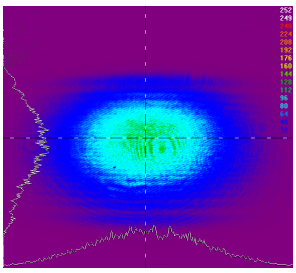	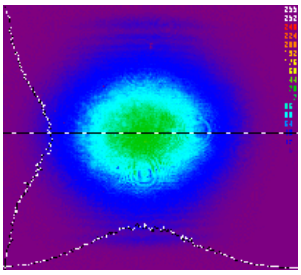	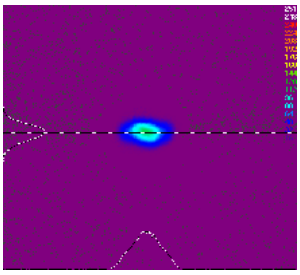
3-D View	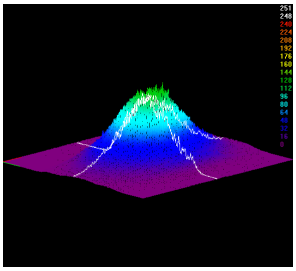	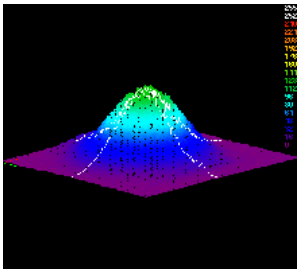	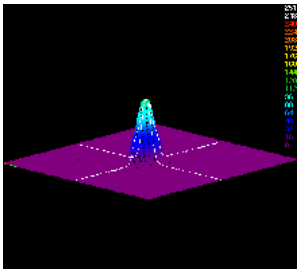
Horiz-X axis	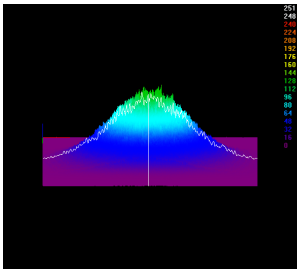	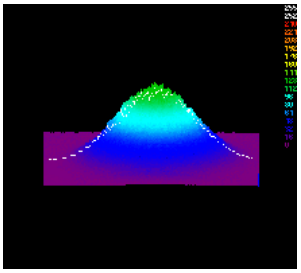	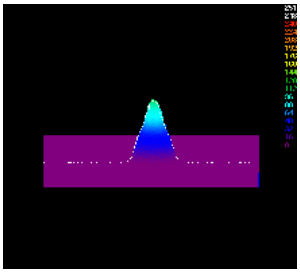
Vert-Y axis	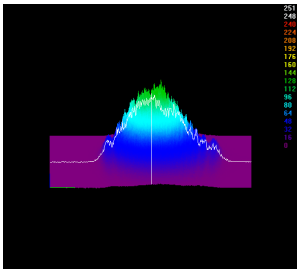	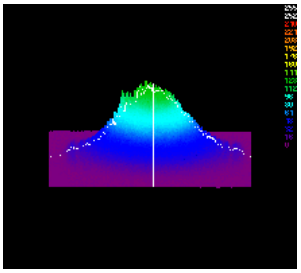	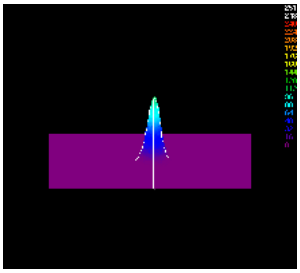

Table 4-2. Laser sources profile.

The profile of the Dye laser shows that the diameter is small compared to the diode lasers and the divergence is greater. Lenses were used to expand and collimate the beam initially, but the beam profile changes when varying the wavelength of the Dye laser. The beam shape varies, the diameter changes slightly within a millimeter, and the

divergence changes slightly causing errors in collimation. The laser power also changes when varying the wavelength. Although the Dye laser's beam diameter is small it is significantly larger at the aperture of the objective because of the divergence and distance to the VivaScope.

4.2. Improve Transmission in the Red

The VivaScope optics were optimized for 830nm wavelength operation. The quarter wave plate wavelength is designed for 830nm, the polarizing beam splitter is for 830nm operation, and the avalanche photodiode detector spectral response sensitivity peaks at 800nm. The 830nm beam splitter measured p-polarization transmission and s-polarization reflection for 630nm were 40% and 90% respectively. A Matlab script was created to calculate the fraction of power received by the detector using the Jones matrices, only considering the beam splitter and quarter wave plate. Using only these optical components the detector would receive about 28% of the light from a 630nm source with the 830nm beam splitter and 830nm quarter wave plate. The 830nm polarizing beam splitter was removed and replaced by a broadband polarizing beam splitter, which responds well from 620-1000nm. With the new beam splitter in place the calculated fraction of power the detector would receive is about 72% with the 630nm as the source. Figure 4-3 shows the typical response of the new beam splitter.

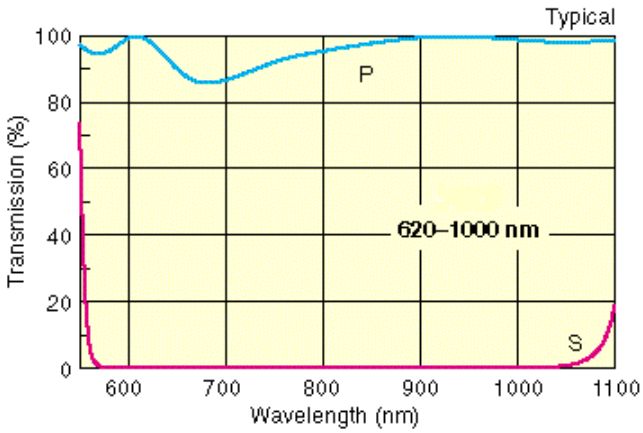

Figure 4-3. New Polarizing beam splitter s and p transmission percentage curve [Newport optics].

There is still a loss going through the quarter wave plate but since it is a zero order quarter wave plate the losses are not significant. The percentage of power received by the detector is approximate; the calculations do not consider all of the optics in the VivaScope system, only the beam splitter and quarter wave plate are considered. In general the losses are greater the further the source is from 830nm. The calculated percentage of power received by the detector is 79% when 660nm is used as the source. The calculations in power received were made for p-polarized beam propagation through the beam splitter, quarter wave plate at a 45º degree angle, returning through the quarter wave plate, and reflecting off the beam splitter, see equation 4.1. The power transmitted and reflected through the original beam splitter was measured for p and s polarization using a linear polarized 630nm HeNe laser. For a 630nm source p transmission (T_p) was 40%, s transmission (T_s) was 0.8%, p reflection (R_p) was 50%, and s reflection (R_s) was 90%. To calculate the percentage of power seen by the detector the following was calculated, where T's and R's are the power transmitted and reflected respectively from the coherency matrix:

$$E = \begin{bmatrix} 1 \\ 0 \end{bmatrix} \qquad \Delta\phi = 2\pi \frac{N}{4} \frac{\lambda_{HeNe}}{\lambda_{830\,Diode}}$$

$$c = \cos(\pi/4) \qquad s = \sin(\pi/4) \tag{4.1}$$

$$F = \begin{bmatrix} \sqrt{R_p} & 0 \\ 0 & \sqrt{R_s} \end{bmatrix} \begin{bmatrix} c & -s \\ s & c \end{bmatrix} \begin{bmatrix} 1 & 0 \\ 0 & e^{2i\Delta\phi} \end{bmatrix} \begin{bmatrix} c & s \\ -s & c \end{bmatrix} \begin{bmatrix} \sqrt{T_p} & 0 \\ 0 & \sqrt{T_s} \end{bmatrix} E.$$

The magnitude squared of F is the fraction of power measured by the detector. With the 830nm polarizing beam splitter some of the 620-690nm p-polarized light would be reflected into the detector causing non-single scattered light to be detected, which would degrade the quality of the image when not imaging at 830nm. With the new beam splitter this is significantly reduced and mostly single scattered light falls on the detector.

4.3. Photomultiplier Tube

A photomultiplier tube was later placed into the system replacing the avalanche photodiode, because signals were too weak for several reasons. First, high power diode lasers in the 630nm to 670nm range are not currently available from diode laser manufactures. Diode lasers systems can be housed in miniature modules that can be easily mounted and coupled into the VivaScope optics. Less space would be required and relocation of the confocal system would be more feasible than with the Dye laser. Second, in order to use the full resolving power (NA) of the objective lens, overfilling the entrance aperture is required. By overfilling the entrance aperture laser power is lost. Third, only back-scattered single reflection light from the tissue at the plane of focus is returned to the detector through the pinhole. The returned signal from the tissue has to have significant intensity (greater than 1nW at APD gain of 200 and 830nm wavelength) to generate a detectable signal for the VivaScope imaging circuit using the avalanche

photodiode (APD). With the 830nm diode laser this is not a problem since the maximum power is 115mW and the system was optimized for 830nm imaging. It was decided to replace the APD with a detector that can generate a high signal from low intensity incident light. The photomultiplier tube (PMT) has the capability to detect low intensity light, amplifying the signal to produce easily measured voltages.

The APD and PMT are optical detectors that absorb photons and produce a current. The main functional difference between the APD and PMT is a significant difference in gain. The APD produces a few hundred electrons per photon and the PMT produces millions of electrons per photon. The photodiode (PD) construction is a semiconductor diode junction similar to a silicon photocell used for solar power conversion, but optimized for sensitivity instead of output power. The APD is reverse biased at a high voltage to produce a moderate gain. The photomultiplier construction is a vacuum tube consisting of a photocathode, electrodes called “dynodes” with voltage dividers, and an anode. Photons that strike the photocathode release electrons that are accelerated by a high negative bias voltage on the cathode. The electrons accelerate towards a series of dynodes each biased by successively more positive voltage. An accelerated electron from the cathode strikes the first dynode and generates more free electrons through a process called secondary emission. These then accelerate towards the second dynode generating many more electrons. Thus if an electron causes m secondary emissions and there are n identical dynodes, the overall gain is m^n. The anode, the final electrode, collects the electrons and delivers them to a resistor, a current to voltage amplifier, or another circuit element. The high gain makes the PMT suitable for low level light detection.

The Hamamatsu R7400U-20 PMT was used to replace the VivaScope APD in order to image with low laser power, specifically the 40mW 660nm diode laser. The output of the PMT was connected to a socket which increases the PMT's maximum DC linear output to 13μA. The PMT and socket was housed in a cylindrical magnetic shield to prevent any magnetic field interference and also to serve as a mount for a 150μm pinhole (same size pinhole mounted on the APD). The output current of the socket is connected to a 10,000 V/A conversion ratio current-to-voltage amplifier. The voltage output of this amplifier was amplified further by a voltage amplifier with a gain of 10. Figure 4-4 shows the PMT circuit connections and components. Finally, the output of the second stage amplifier feeds into the VivaScope board to a preamplifier and then to an analog to digital converter. The range of the A/D converter on the VivaScope electronics board is 0V to 3.3VDC. Therefore each pixel count on the VivaScope acquired image corresponds to a voltage of about 12.9mV. The voltage swing of the PMT circuit can saturate the acquired image (reach a pixel values from zero to 255 counts).

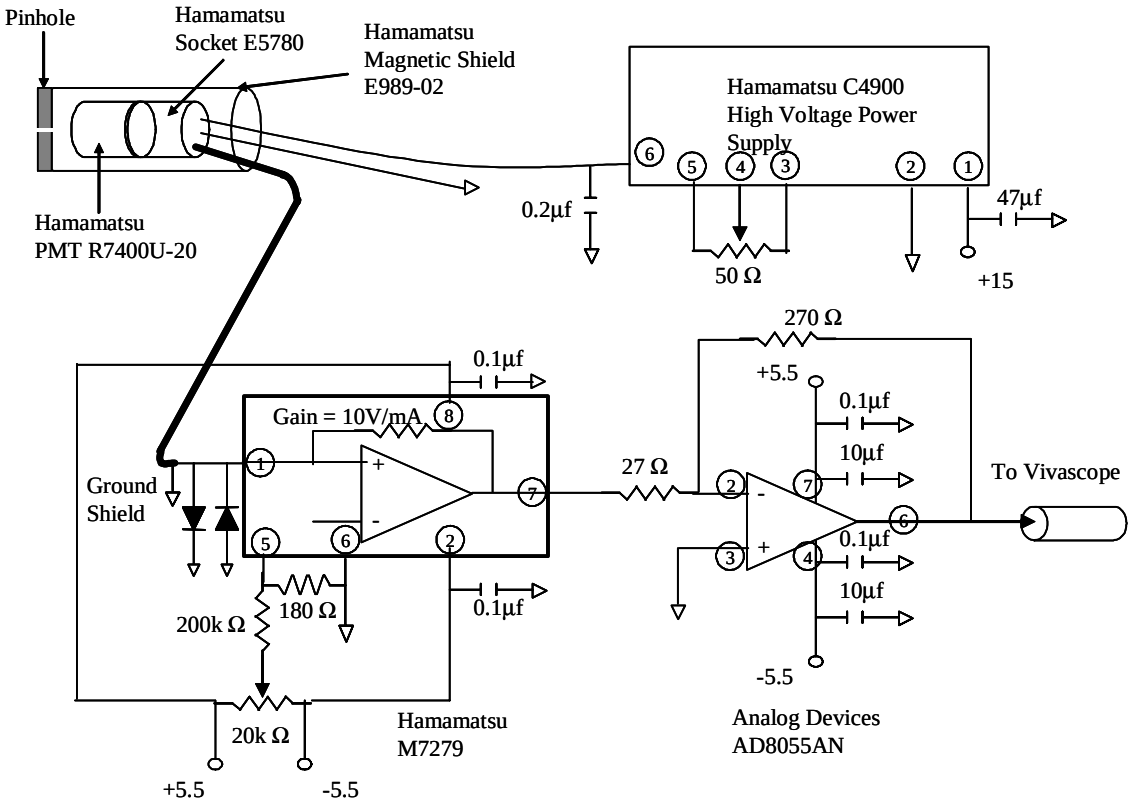

Figure 4-4. Circuit layout of PMT.

At a wavelength of 630nm the PMT has a sensitivity of 78mA/W at the photo cathode and the APD has a pre-gain sensitivity of 0.333A/W. Both, the APD and PMT have a current-to-voltage amplifier to convert current to voltage. The APD's factory shipped gain is 30 but could be adjusted via a gain adjustment trimmer up to 200. The PMT has a maximum gain of 2×10^6 at negative 1000VDC applied to the photocathode. With negative 500 volts applied to the PMT, the gain is 2×10^4. To compare the sensitivity of both detectors take the following voltage output of each detector for 1nW of incident light as an example:

$$V_{out\,APD} = Power_{in} \times Radiant\,Sensitivity \times APD\,Gain \times Amplifier\,Gain$$
$$= Power_{in} \times 0.3333\frac{A}{W} \times 30 \times (1\times10^{5}\,\frac{V}{A})$$
$$= Power_{in} \times 10^{6}\,\frac{V}{W} \qquad (4.2)$$

$$Pixel_{value} = Power_{in} \times 10^{6}\,\frac{V}{W} \times \frac{1}{0.013}\frac{counts}{V}$$
$$= Power_{in} \times (77\times10^{6})\frac{counts}{W}$$
$$= 0.077\,counts$$

The voltage output of the APD would be 1mV for 1nW incident light at 630nm. This would not register as a pixel count even with an APD maximum gain of 200.

$$V_{out\,PMT} = Power_{in} \times Radiant\,Sensitivity \times PMT\,Gain \times I-V\,Gain \times V-V\,Gain$$
$$= Power_{in} \times 0.078\frac{A}{W}(2\times10^{4}) \times 10000\frac{V}{A} \times 10$$
$$= Power_{in} \times (156\times10^{6})\frac{V}{W}$$

(4.3)

$$Pixel_{value} = Power_{in} \times (156\times10^{6})\frac{V}{W} \times \frac{1}{0.013}\frac{counts}{V}$$
$$= Power_{in} \times (12\times10^{9})\frac{counts}{W}$$
$$= 12\,counts$$

The voltage output of the PMT circuit would be 0.156V for 1nW incident light at 630nm. This would register at about 12 pixel counts and the PMT gain can further be increased to a maximum of 2 x 10^{6}.

4.4. VivaScope Stage

The VivaScope stage was created to image the skin sample though a custom made tissue cassette. The tissue cassette is a plastic disk that folds to seal the included tissue. It has a clear plastic center for imaging the tissue and an adhesive outer square to form an air tight seal. An image of the tissue cassette can be seen in Figure 4-5. The tissue cassette is inserted into a holder on the VivaScope which can be moved in the left/right (x) and forward/backward (y) direction by two motorized actuators. A cover cone mounted above the objective lens presses onto the bottom of the tissue cassette for imaging. To scan axially, the cover cone moves the center of the tissue cassette vertically by a motorized actuator. The tissue cassettes did not suit our purpose. They left air bubbles in the inside of the enclosed seal and they were for a one-time use, making experiments more costly. Also the stage with the holder did not allow for axial resolution measurements with fine increments. The axial, up/down (z), motorized actuator control allowed about 3μm increments per count and was not accurate.

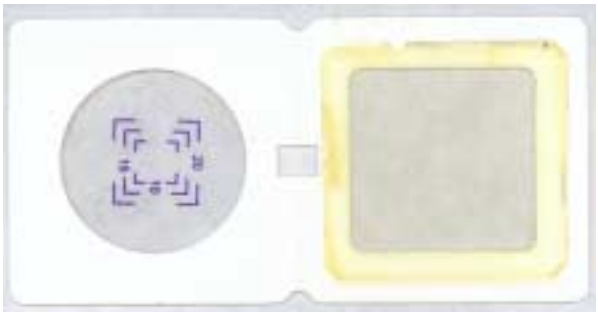

Figure 4-5. VivaScope tissue cassette.

A new stage was machined and mounted above the objective. The new stage did not require the cover cone. It uses commercially available cover glasses (170um thick), and sandwiches the excised tissue between two cover glasses to make the tissue as flat as

possible for imaging. Most importantly it allows for the use of an approximate 1μm per division differential micrometer to be mounted and used for axial resolution measurements. Axial resolution is used to judge the alignment and measure the performance of the system. The new stage incorporates the existing x and y actuators and also the optional use of the existing z axial actuator, see Figure 4-6 below.

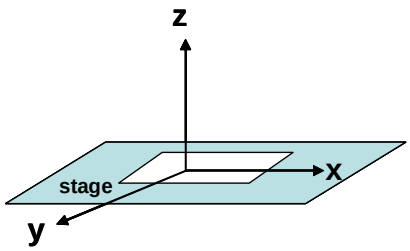

Figure 4-6. Movable direction of stage.

4.5. VivaScope Fast Scanner

The VivaScope polygon scanner was scanning more lines than needed for our work. With the beam propagating in the optical axis the polygon scans in the horizontal direction (fast scan) while the galvanometric scanner scans in the vertical direction (slow scan). By making configuration changes to the VivaScope software the scan speed of the polygon was reduced. These changes will prolong the life of the scanner by reducing unnecessary stress, wear, and tear. This also reduces vibrations caused by the fast scanner on the VivaScope optical board.

4.6. Implement a flexible unit

The VivaScope hardware was removed from its enclosure and mounted onto a breadboard table with the optics easily accessible. The polygon connection to the VivaScope electronics board was extended with a cable bus in order to separate the electronics board from the VivaScope optics board. The circuit board was mounted on

the side of the VivaScope optical board for the optics to be readily accessible for adjustment or replacement. This allows alignment of the sliding mirror and optics, proper placement of the 830nm laser after relocation, and power measurements of the laser sources on the board. Additional optics and configurations may also be made without committing to one particular alignment or setup by placing optics on mounts that allow fine adjustments. This is crucial when attempting to focus a beam into a 150 micron pinhole and optimize the alignment to reduce aberrations.

5. Analysis of Multi-Spectral Confocal Microscope

5.1. Light Path and Optics

The Lucid VivaScope 2000 laser scanning confocal microscope is an inverted microscope that can display images at about 9-10 frames per second. Refer to Figure 5-1 for the VivaScope 2000 optics board layout. Horizontally polarized (p-polarized) light is transmitted through a polarizing beam splitter. The polarizing beam splitter transmits horizontally polarized (p-polarized) light and reflects vertically polarized (s-polarized) light. The laser light is then reflected from a rapidly rotating polygon mirror, which has 30 facets, into the first telescope system. A split diode consisting of an LED and detector shines light and detects it from the polygon mirror for synchronization. The first telescope system has a magnification ratio of about 3.3x on the input laser beam diameter. The laser light is then reflected from the galvanometric mirror into the second telescope system. The second telescope has a magnification ratio of about 1.1x on the input laser beam diameter. The laser beam is magnified in two places so not to exceed the dimensions of the mirrors and apertures. After the second telescope system the laser

beam travels through a quarter wave plate which has its fast axis rotated at a forty-five degree angle with respect to the linearly polarized light, to change the stage of polarization from p-polarized to circularly polarized light. The circularly polarized laser light then travels through the objective lens which focuses the laser light to a tiny spot on the target surface. Single back scattered light collected by the objective lens travels back through a similar optical path as the illumination path. The light reflected by the target surface is represented by arrows on the outside of the collimated beam in Figure 5-1. Single scattered light maintains its state of polarization. Therefore circularly polarized light that travels back towards the quarter wave plate is changed to s-polarized light. The back scattered light is then de-scanned and de-magnified by the scanning mirrors and telescope systems. The back scattered light is then reflected by the polarizing beam splitter to a lens. The light is then reflected from a mirror and focused to a spot at the aperture in front of the detector. Only single back scattered light from the illumination spot on the target is registered by the detector. Back scatted light which is not single scattered (or is not circularly polarized) will not be converted to s-polarization by the quarter wave plate and therefore not be reflected by the polarizing beam splitter towards the detector. Also specular reflection (glare) from normal incident light on the optics before the quarter wave plate is minimized. The specular reflection which maintains its state of polarization is not reflected by the polarizing beam splitter to the detector because it is p-polarized. Specular reflection from normal incident light after the quarter wave plate is eliminated by a slight tilt of the quarter wave plate. With a pinhole size of 150μm, a solid bright centered vertical line would be seen in the images if the quarter

wave plate is not slightly tilted or the beam splitter reflected the specular reflected light to the detector.

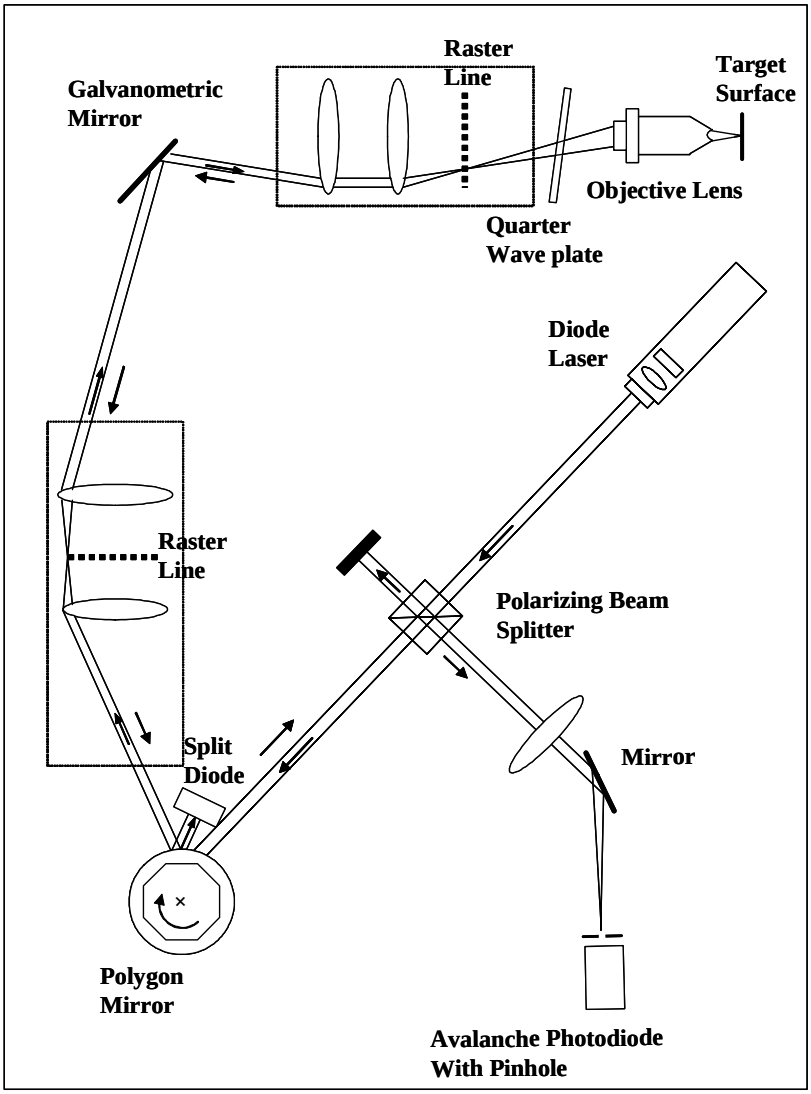

Figure 5-1. VivaScope optical board.

Refer to Figure 5-2 for a confocal microscope's focal points and conjugate planes similar to the VivaScope 2000. The objective lens is infinity-corrected, meaning an

image is formed by parallel beams as opposed to at a spot 160mm away. The objective images a point source at the object plane O. The objective lens's back focal plane (entrance aperture) plane P is imaged by the telescope system's lenses. The entrance aperture, galvanometric mirror, and polygon mirror surfaces are pupil conjugates. That is where the scanning takes place. An image of the object point source is imaged at O planes.

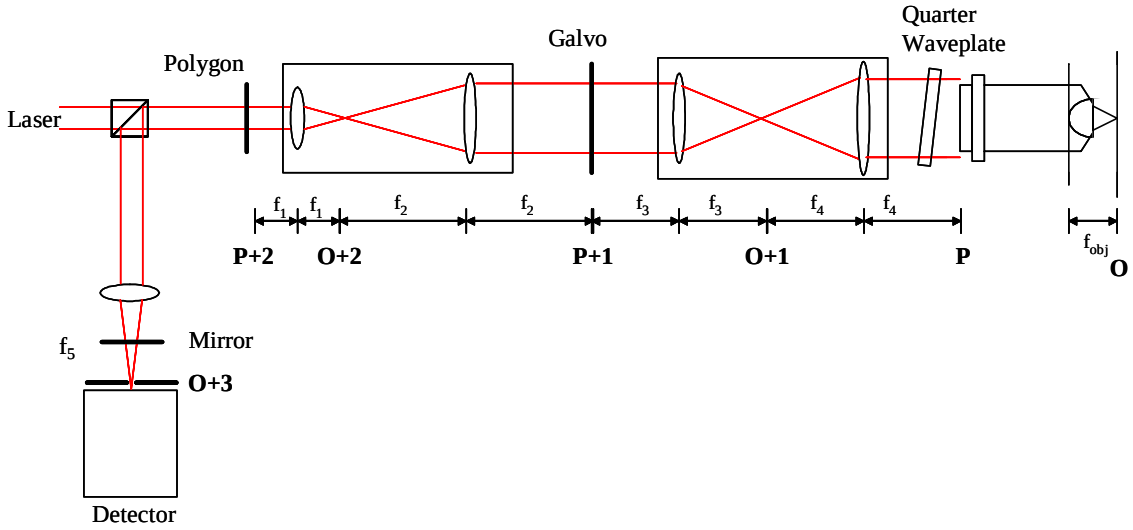

Figure 5-2. Optics layout of the confocal system. O is conjugate to the object and P is conjugate to the pupil.

5.2. Point Spread Function

5.2.1. Paraxial and Non-Paraxial

Paraxial imaging assumes that the angles are small and therefore sin(α) is approximately equal to α. In non-paraxial analysis this is not assumed. The point spread function (PSF) is the three-dimensional diffraction pattern observed in the region of focus of a lens when the illumination source is uniform over the pupil aperture. This is accomplished by overfilling the entrance aperture with a laser beam. A laser beam has a

Gaussian cross-section and if it underfills the aperture the focused beam will also have a Gaussian cross-section intensity.

$$I = I_0 e^{-2r^2/w^2}, \qquad (5.1)$$

where *w* is the beam waist defined at the $1/e^2$ beam radius. In order to use the full NA of the objective lens the entrance aperture needs to be overfilled. For small NA (small semi-aperture angle α) and an aberration free system the transverse intensity distribution is that found by Airy (eq 2.4). Lommel and Struve later extended Airy's analysis for the whole three-dimensional PSF [Born and Wolf], which agrees with Airy in the transverse intensity and is the sinc-squared function in the axial direction (eq 2.8). Richards and Wolf in 1959 presented a solution not limited to systems with low numerical apertures. The assumptions made for imaging are that the system uses linearly polarized monochromatic light, obeys the Abbe sine condition, images a point source at infinity, and is stigmatic (no aberrations). It is also assumed that the wavelength is small compared to the linear dimensions of the exit pupil. The derived electric and magnetic vectors in the image space are

$$\vec{e}(u,v,\phi) = -iA(I_0 + I_2\cos 2\phi)\,\hat{x} \; - \; iAI_2 \sin 2\phi\,\hat{y} \; - \; 2AI_1\cos\phi\,\hat{z} \qquad (5.2)$$

$$\vec{h}(u,v,\phi) = -iAI_2 \sin 2\phi\,\hat{x} \; - \; iA(I_0 - I_2\cos 2\phi)\,\hat{y} \; - \; 2AI_1\cos\phi\,\hat{z} \qquad (5.3)$$

where A is a constant, ϕ is the azimuth angle, and *u*, *v* are normalized optical coordinates for convenience The source polarization defines the direction in which ϕ equals to zero. The I terms are the integrals below:

$$I_0(u,v)=\int_0^{\alpha}\sqrt{\cos\theta}\ \sin\theta\ (1+\cos\theta)\ J_0\left(\frac{v\sin\theta}{\sin\alpha}\right)e^{iu\cos\theta/\sin^2\alpha}d\theta$$

$$I_1(u,v)=\int_0^{\alpha}\sqrt{\cos\theta}\ \sin^2\theta\ J_1\left(\frac{v\sin\theta}{\sin\alpha}\right)e^{iu\cos\theta/\sin^2\alpha}d\theta \qquad (5.4)$$

$$I_2(u,v)=\int_0^{\alpha}\sqrt{\cos\theta}\ \sin\theta\ (1-\cos\theta)\ J_2\left(\frac{v\sin\theta}{\sin\alpha}\right)e^{iu\cos\theta/\sin^2\alpha}d\theta\ .$$

The PSF is at the point (u, v, ϕ) in the image region and the integration is over the semi-aperture angle angle α. The coordinates are defined by Figure 5-3.

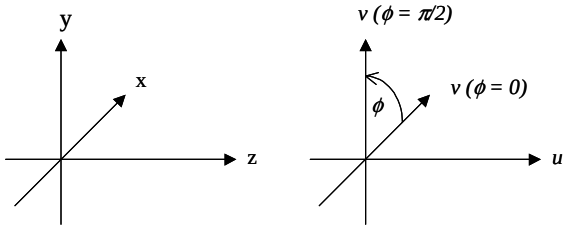

$$u = zk\sin^2\alpha$$
$$v = \sqrt{x^2+y^2}\,k\sin\alpha \qquad (5.5)$$

Figure 5-3. Coordinate system.

The energy density is

$$< w(u,v,\phi) > = \frac{1}{16\pi}(\vec{e}\cdot\vec{e}^{\,*} + \vec{h}\cdot\vec{h}^{\,*}) = \frac{A^2}{8\pi}\left\{|I_0|^2 + 2|I_1|^2 + |I_2|^2\right\}. \qquad (5.6)$$

Therefore the point spread function normalized intensity is $\left\{|I_0|^2 + 2|I_1|^2 + |I_2|^2\right\}$ and the confocal point spread function is $\left\{|I_0|^2 + 2|I_1|^2 + |I_2|^2\right\}^2$. These equations were implemented using Matlab. The Richards and Wolf paper has a table of values for the electric field energy at given v and α values, u and ϕ are set to zero. To test the accuracy

of the Matlab program the electric field energy was calculated at the same *v* and α values. The results can be seen in Table 5-1.

$\alpha = 0$		$\alpha = 30$		$\alpha = 60$		$\alpha = 75$		$\alpha = 90$	
v	value	*v*	Value	*v*	value	*v*	value	*v*	value
0.93	80.22	0.98	80.11	1.16	80.11	1.33	79.99	1.48	79.97
1.4	59.93	1.47	60.07	1.73	60.25	1.95	59.87	2.10	59.94
1.83	40.43	1.94	40.07	2.27	40.46	2.5	40.24	2.63	40.32
2.36	20.05	2.5	20.21	2.93	20.04	3.14	20.03	3.23	20.11
3.38	4.5e-4	4.15	0.88	4.75	0.820	4.75	0.549	4.7	0.376
7.02	8.6e-5	7.03	0.202	8.1	0.199	8.1	0.122	8	0.072

Table 5-1. The values columns match very closely to the values column in Table 1 of Richards and Wolf, which is 80, 60, 40, 20, 1st minimum, and 2nd minimum. The maximum variation for each row is 0.22, 0.25, 0.46, 0.21, 0.88, and 0.202 respectively. This was done specifically to check the Matlab integrations for the I terms.

The three-dimensional point spread function at the objective was computed. Figure 5-4 shows a contour of the three-dimensional point spread function. The point spread function irradiance distribution is symmetric and does not depend on ϕ, the azimuth angle. It only depends on *u* and *v* the radial and axial coordinates. I will use ρ and ζ for the radial and axial components defined by equation 2.6 and 2.10 respectively, which are repeated below. The (ρ, ζ) coordinates are similar to (*u*,*v*) except (ρ, ζ) include (λ/n) the index of the medium and are both in terms of NA.

$$\rho = \frac{2\pi}{\lambda} \cdot r \cdot NA \qquad \zeta = \frac{2\pi}{n\lambda} \cdot z \cdot NA^2 \tag{5.7}$$

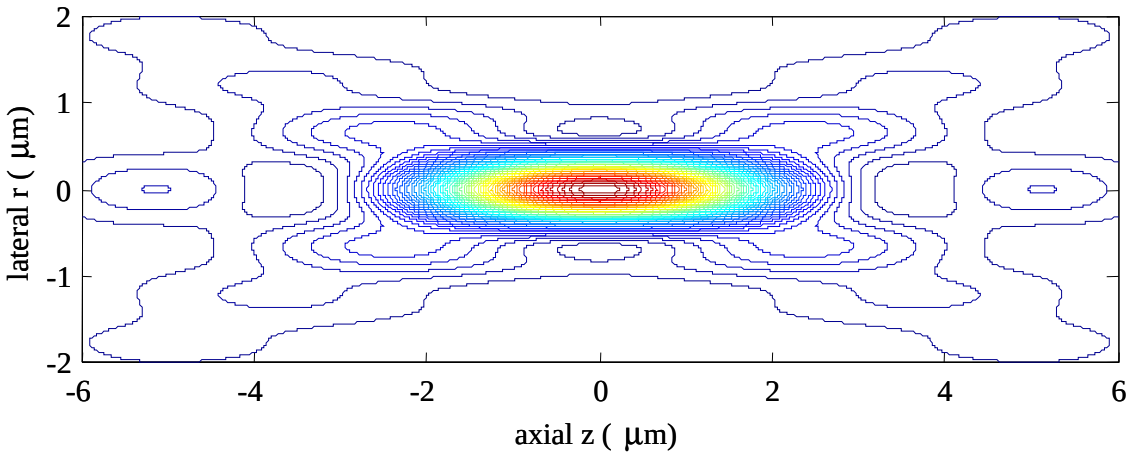

Figure 5-4. Point spread function at the objective lens for 830nm, NA 0.75, and index of refraction of 1.33. The focal point is center at (0,0).

At the objective lens the paraxial approximations for the lateral irradiance is Equation 2.4 and for the axial irradiance is Equation 2.8. Both are repeated below

$$PSF(\rho) \approx \left(2\frac{J_1(\rho)}{\rho} \right)^2, \tag{5.8}$$

$$PSF(\zeta) \approx \left(\frac{\sin(\zeta/4)}{\zeta/4} \right)^2. \tag{5.9}$$

The combined lateral and axial irradiance for the non-paraxial case is

$$PSF(\rho,\zeta) = \left\{ |I_0|^2 + 2|I_1|^2 + |I_2|^2 \right\}, \tag{5.10}$$

and can be seen in Figure 5-4. The confocal point spread function for a point source and a subresel pinhole is the square of equation 5.8, 5.9, and 5.10 since the illumination lens and imaging lens are identical for reflectance confocal. When the pinhole radius divided by the objective lens's magnification is smaller than the point spread function's lateral resolution the pinhole is subresel. The effects of the pinhole can be ignored in the

confocal lateral and axial irradiance distribution if the pinhole radius is subresel, except for a decrease in signal.

$$PSF_{conf}(\rho) \approx \left(2\frac{J_1(\rho)}{\rho} \right)^4, \tag{5.11}$$

$$PSF_{conf}(\zeta) \approx \left(\frac{\sin(\zeta/4)}{\zeta/4} \right)^4, \tag{5.12}$$

$$PSF_{conf}(\rho,\zeta) = \left\{ |I_0|^2 + 2|I_1|^2 + |I_2|^2 \right\}^2. \tag{5.13}$$

The lateral and axial response at the objective for the paraxial and non-paraxial can be seen in

Figure 5-5 for 0.75 NA and Figure 5-6 for 1.2 NA.

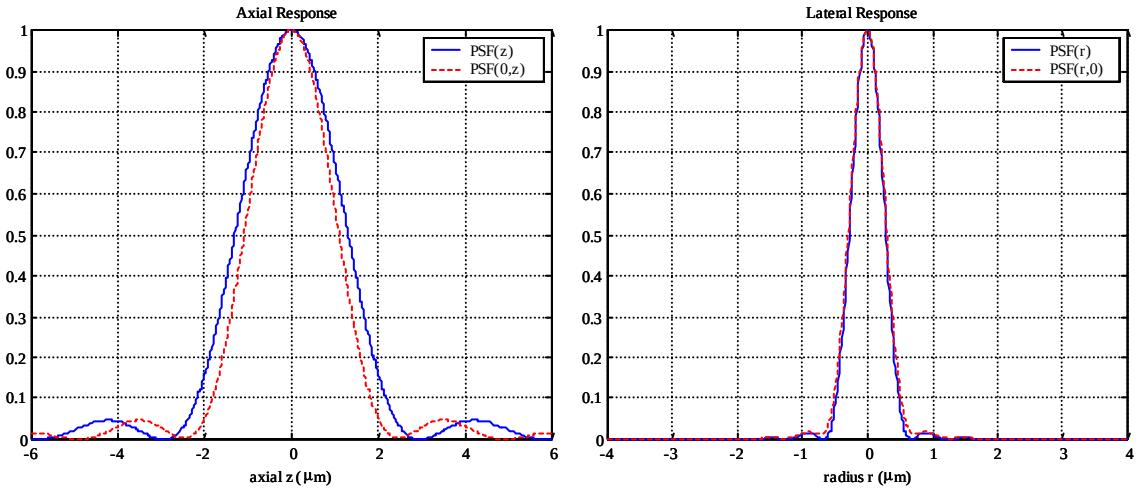

Figure 5-5. Paraxial (solid line) and non-paraxial (dashed line) axial and lateral response at the objective lens through air, at 830nm, and NA of 0.75.

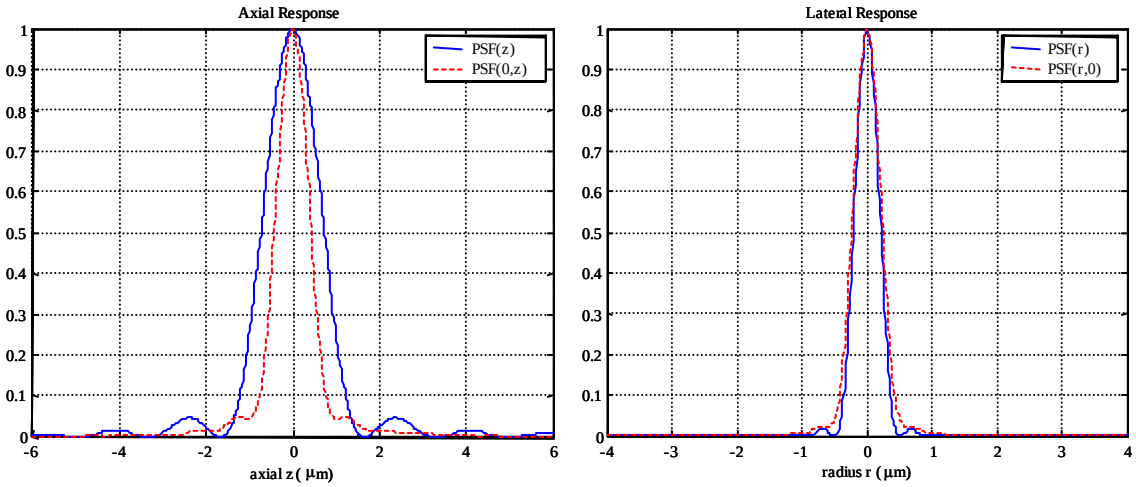

Figure 5-6. Paraxial (solid line) and non-paraxial (dashed line) axial and lateral response at the objective lens through air, at 830nm, and NA of 1.2.

From the graphs above it can be seen that the non-paraxial axial response is narrower, the minima do not all cross zero, and the lateral response is similar to the paraxial. The deviation from the paraxial axial resolution is greater for larger NA.

5.2.2. Resolution with Pinhole

So far we have ignored the effects of the pinhole on the lateral and axial resolutions. The point spread function depends on the NA of the objective lens, the imaging wavelength, and immersion media. If the pinhole is not subresel the lateral and axial resolution are affected by the size of the pinhole. To consider the effects of the pinhole Fourier optics are employed. The object plane is chosen as the plane of reference and objects are scaled to the object plane. The laser source acts as a point source at negative infinity. Assume uniform illumination of the objective's aperture. The non-paraxial PSF is used as the PSF of the objective lens, which is the impulse response of the lens, h(ρ, ζ). For transmission of the laser light to the object plane we have

$$\delta(\rho, \zeta) \otimes psf_1(\rho, \zeta), \tag{5.14}$$

where $\delta(\rho, \zeta)$ is the point source, convolved with the objective lens's PSF. For the receive side we have the scaled pinhole convolved with the objective lens's PSF

$$circ(\rho) \otimes psf_2(\rho, \zeta), \tag{5.15}$$

where circ(ρ) is the de-magnified pinhole. The transmission and receive terms are multiplied at the object plane. See Figure 5-7 for an illustration of the convolution.

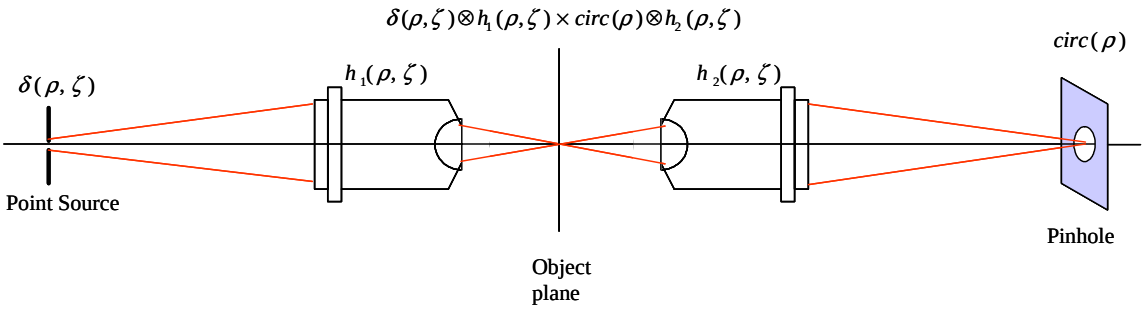

Figure 5-7. Schematic of the convolution of the point source and objective lens's PSF, also the convolution of the scaled pinhole and the objective lens's PSF.

Since the convolution of the point source with PSF_1 is PSF_1 we have

$$psf_1(\rho, \zeta) \times \left[circ(\rho) \otimes psf_2(\rho, \zeta)\right]. \tag{5.16}$$

Also, the objective lenses are same, using reflectance confocal microscopy, $PSF_1 = PSF_2 = PSF$ and $h_1 = h_2 = h$.

Figure 5-8 left and right shows the radius at half width for lateral and axial response, respectively, in optical units (eq 5.7) as a function of pinhole radius (ρ_p). The radius of the lateral response at half width ($\rho_{½}$) is relatively insensitive for pinhole radius ρ_p less than 1 o.u. and $\rho_{½}$ remains around 1.2 o.u. For pinhole radius ρ_p greater than 4 o.u. $\rho_{½}$ remains around 1.65 o.u. Figure 5-8 right shows the axial radius at half width ($\zeta_{½}$) for the axial response as a function of pinhole radius. The axial half-width remains

constant for pinhole radius ρ_p less than 2.5 o.u., therefore the axial discrimination is also constant. For pinhole radius greater than 7.5 o.u the axial half width increases linearly with pinhole size. The results agree closely to that of T. Wilson and A.R. Carlini, 1987.

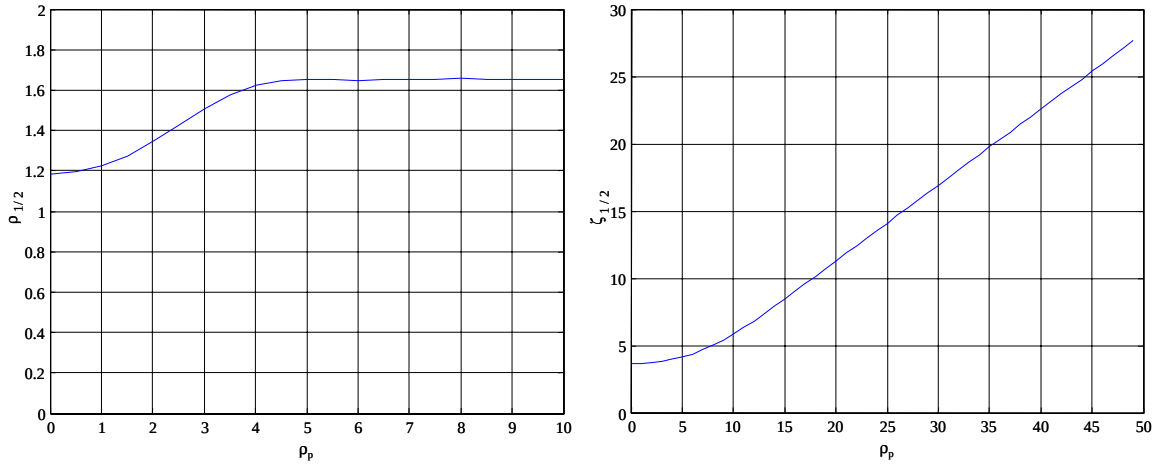

Figure 5-8. The half-width of a point object as a function of the detector pinhole radius in optical units. Left is half-width of the lateral response, right is the half-width of the axial response.

The corresponding curves for the lateral and axial resolution at full-width half-maximum as a function of pinhole diameter in meters can be seen below. The curves are the same but now the values are physical length units. Figure 5-9 is for a wavelength of 830nm, NA of 0.75, and index of refraction of 1.33.

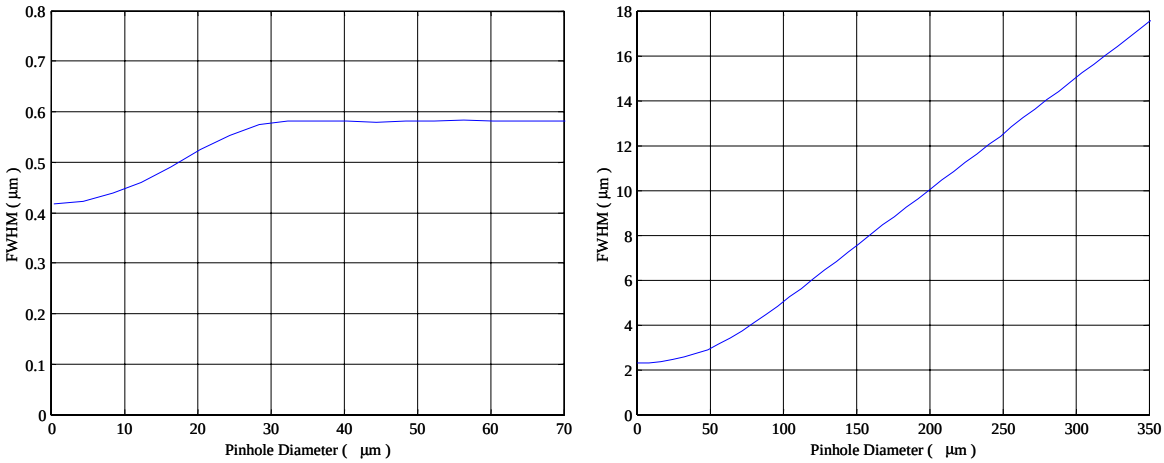

Figure 5-9. The full-width half-maximum of a single point object as a function of pinhole diameter. Left is the FWHM of the lateral resolution, right is the FWHM of the axial resolution.

5.2.3. Measured Resolution

To measure the lateral resolution an edge spread function across a target was imaged, the line spread function was then calculated, and the full-width half-maximum was measured to calculate the lateral resolution. The test targets imaged included chrome on glass USAF resolution chart and the edge of a 170 µm glass slide. The axial resolution was measured by axially moving a mirror through the focus of the objective lens at intervals of about 0.5-1µm and capturing each image. The remitted irradiance versus axial distance was plotted. The full width of the plotted curve at half maximum was used to define the axial resolution.

For the axial measurement a point or an average of points was plotted versus the axial distance traveled by a micrometer. For the lateral measurement the derivative of a single line of the image was plotted verses pixel. The FWHM of pixel length was then converted to meters by multiplying the pixel length by the number of microns per pixel.

The number of microns per pixel was measured by imaging a reticle and was found to be 1.2 microns per pixel.

Figure 5-10 shows the confocal image of the reticle. The squiggly lines are due to vibrations in the confocal system.

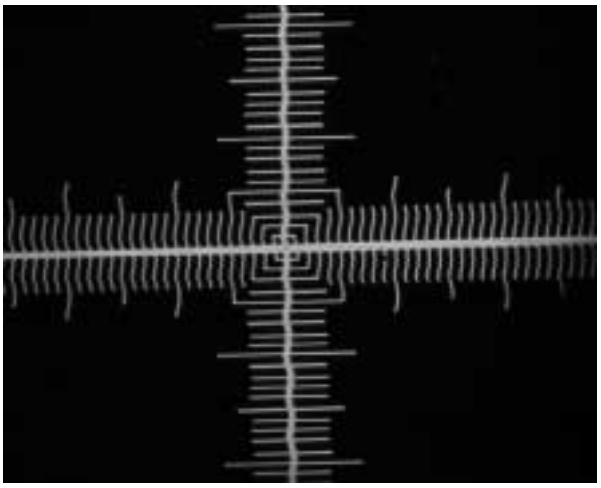

Figure 5-10. Confocal image of 10μm per division reticle.

The measured lateral resolutions were found to be 1.2um for all wavelengths; 830, 660, 650, and 630 nm. The lateral resolution was limited by the number of pixels per micron. The lateral response for 830nm can be seen in Figure 5-11. The confocal image of an edge was imaged, a line through that edge was taken, and then the derivative of that line was calculated. Then FWHM of that line was measured. The other wavelengths lateral resolution was measured the same.

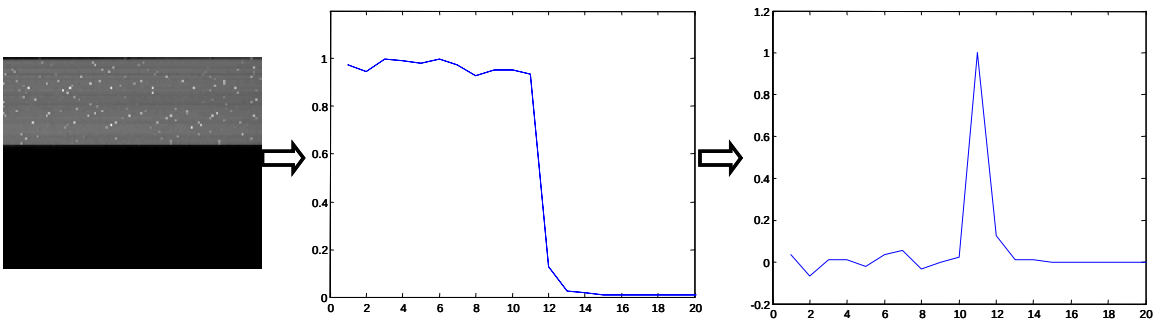

Figure 5-11. Confocal image at 830nm of a USAF bar edge (left), edge spread function (center), and line spread function (right).

The lateral resolution measured compared to the theoretical values for paraxial, non-paraxial, and non-paraxial with a 150 micron pinhole diameter can be seen in Table 5-2. The calculations for paraxial, non-paraxial, and non-paraxial with pinhole are all using an NA of 0.75 and index of 1.33. The calculated confocal lateral resolutions use a point source and a subresel pinhole. The paraxial and non-paraxial FWHM lateral resolution are similar. This is because the angle α is reduced when using an immersion medium, water n = 1.33.

Lateral (nm)	Paraxial (μm)	Non-paraxial (μm)	Non-paraxial w/ 150μm Pinhole (μm)	Measured (μm)
830	0.40	0.41	0.58	1.2
660	0.32	0.33	0.46	1.2
650	0.31	0.32	0.45	1.2
630	0.30	0.31	0.44	1.2

Table 5-2. Lateral resolution theoretical and measured FWHM

The axial response, other than measuring axial resolution, was also used to assess the system alignment. Axial response curves that were significantly asymmetric indicated the system was not aligned properly. The system was re-aligned unit the axial

response curve was more symmetric. Perfect axial response curves were not attainable, as some asymmetry was present, most likely due to small mis-alignment, spherical aberration, and astigmatism [T. Wilson and AR Carlini 1989]. T. Wilson and AR Carlini 1989 have noted that the effects of lens aberration increases with pinhole diameter. For our multi-spectral confocal system the axial response depended on alignment and laser source. The lenses in the system were not changed. The Dye laser beam varied from one wavelength to the other, the beam divergence changed and the beam profile changed. The micrometer used to move the mirror axially was a differential micrometer at about 1 μm per division. The axial resolution curves for the different laser sources and detectors can be seen in Figure 5-12, Figure 5-13, Figure 5-14, and Figure 5-15. The axial curves with the PMT were only measured for the 830nm and 660nm diode lasers.

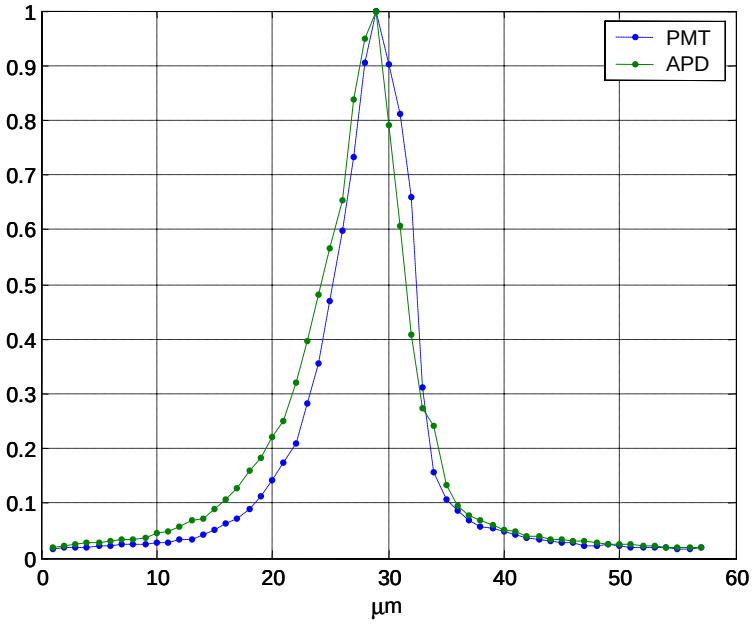

Figure 5-12. Axial curves for 830nm Diode laser with the PMT and APD

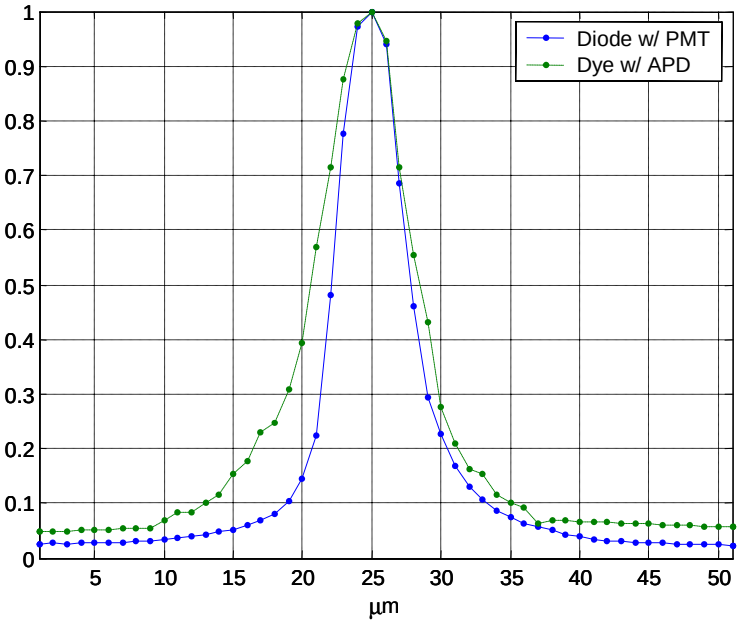

Figure 5-13. Axial curve for 660nm Diode laser w/ PMT and Dye laser at 660nm with APD

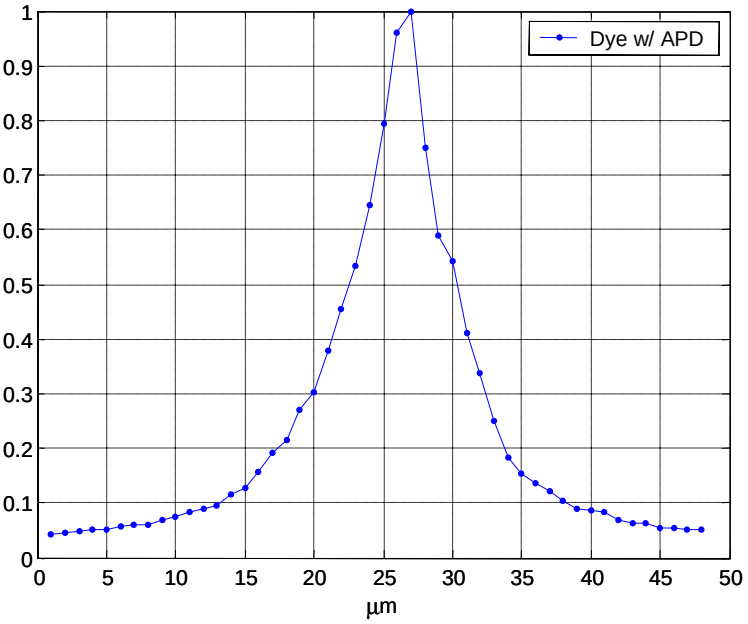

Figure 5-14. Axial curve for Dye laser at 650nm with the APD

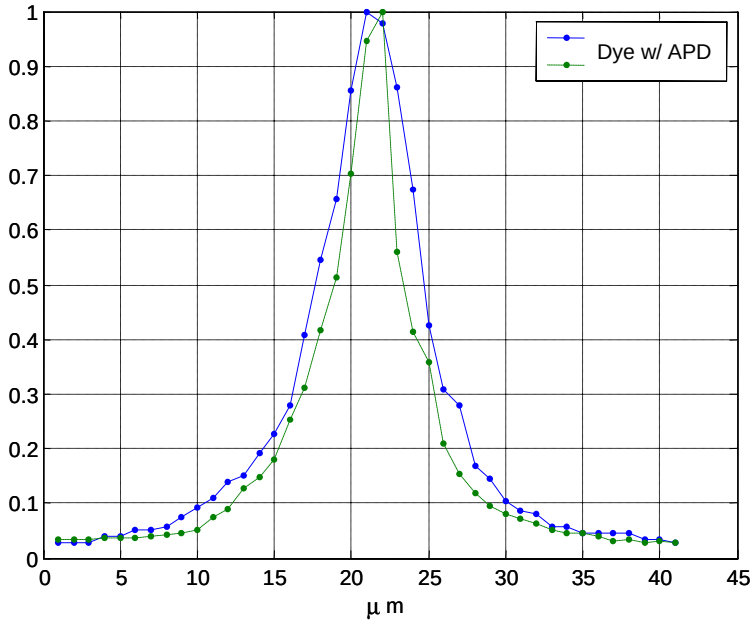

Figure 5-15. Axial curve measured for the Dye laser at 630nm with the APD. The axial resolution is between 5-7 µm.

The measured axial resolution compared to the theoretical values for paraxial, non-paraxial, and non-paraxial with a 150 micron pinhole diameter can be seen in Table 5-3. The calculations for paraxial, non-paraxial, and non-paraxial with pinhole are all using NA of 0.75 and index of 1.33. The calculated confocal axial resolutions use a point source and a subresel pinhole. The axial resolution measured in some instances maybe better than the non-paraxial with the 150µm pinhole. This is possibly due to minor measurement errors, since the measurements were made manually. For a 150µm pinhole the calculated FWHM axial resolution remains at 7.5µm from 830-660nm. This is because the pinhole and axial PSF convolution is dominated by the pinhole for large pinhole diameters relative to the axial PSF. The paraxial and non-paraxial axial resolutions are similar because the angle α is reduced.

Axial (nm)	Paraxial (μm)	Non-paraxial (μm)	Non-paraxial w/ 150μm Pinhole (μm)	Measured (μm)
830	2.5	2.28	7.5	8 - 7
660	1.98	1.81	7.5	8 - 6
650	1.96	1.79	7.5	7 - 6
630	1.9	1.73	7.5	7 - 5

Table 5-3. Axial resolution theoretical and measured FWHM

5.3. Dispersion

The plane of focus shifts slightly for the different wavelengths. The sample being imaged has to be moved down about 7 to 5 microns when switching from 830nm to 660nm, 650nm, or 630nm in order to image the same plane on the sample. The focal plane shift is caused by dispersion and differences in beam divergence. To calculate the dispersion of a simple lens the formula below can be used.

$$n^2(\lambda)-1=\frac{B_1\lambda}{\lambda^2-C_1}+\frac{B_2\lambda}{\lambda^2-C_2}+\frac{B_3\lambda}{\lambda^2-C_3} \tag{5.17}$$

The constants B_1 through C_3 can be obtained from glass manufacturers. The Schott Optical Glass catalog has the constants for many different optical glasses. The Schott Optical Glass constants for glass type BK7 can be found in the Melles Griot catalog. The constants for synthetic fused-silica can also be found in the Melles Griot catalog, which was taken from Malitson. For fused-silica the C constants are squared. The dispersion for BK7 and fused-silica were calculated and the focal length variations for a focal length of 10μm at 830nm were calculated. Focal length versus wavelength, calculated using the simple lens equation, can be seen in Figure 5-16. The difference in focal length can be as great as 90μm from 830nm to 630nm.

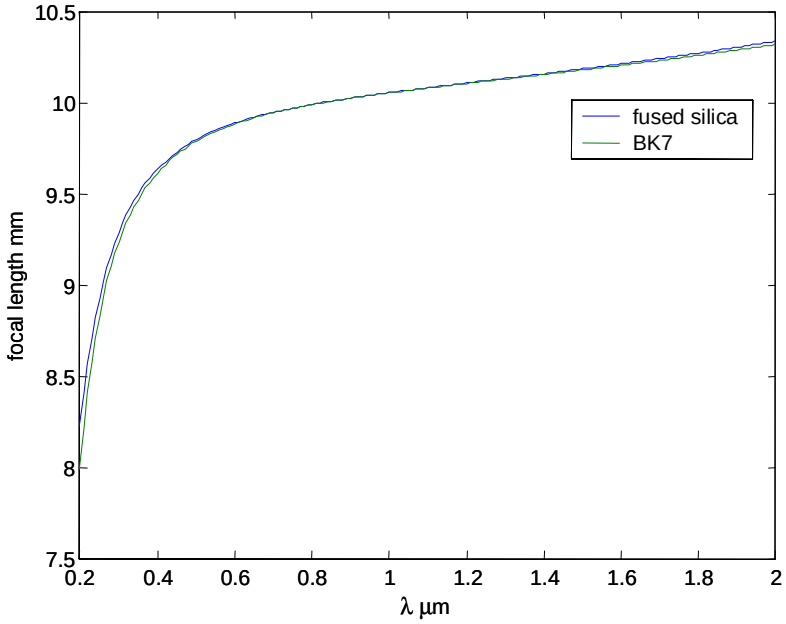

Figure 5-16. Focal length verses wavelength for simple lens

The dispersion for a thin lens is obviously greater compared to an objective lens corrected for chromatic dispersion. The objective lens used for our multi-spectral confocal system is a Nikon CFI Plan Fluor, which is corrected for chromatic dispersion. Out of the wavelengths used in our system, the objective lens's focal length deviation from 830nm is greatest for 660nm. This information was obtained from Nikon. In order to know the maximum focal length deviation for the multi-spectral system the focal length variation was measured from 830nm to 660nm. Calculating the dispersion for each optical element would prove to be very difficult and may not lead to the true focal length deviation. The axial curve for 830nm and 660nm for both diode lasers (which have similar divergence) was measured, see Figure 5-17. The maximum deviation was found to be about 7 microns.

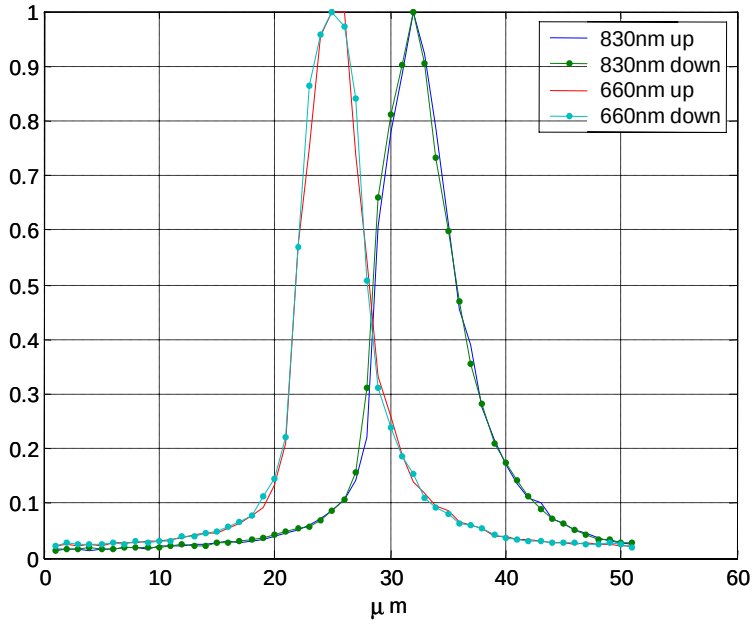

Figure 5-17. Axial curves for 830nm and 660nm showing dispersion in the system. The curves were obtained by moving a mirror axially up and then down for each wavelength.

6. Imaging Experiments

The tissue preparation involved rinsing the frozen tissue from Mohs surgery, staining the sample with either MB or TB, rinsing the sample with saline, and staining with acetic acid. The tissue samples were then imaged with the multi-spectral confocal microscope. To achieve optimal dye (MB and TB) uptake variations in the contrast agent's concentration and staining/rinsing time were tested on the excised skin tissue. Mosaics of the confocal images were created and compared to each other and histology.

6.1. Tissue Preparation and Handling

Discarded fresh-frozen tumor tissue was received from a Mohs surgeon. The tissue was rinsed in Dulbecco's Phosphate Buffered Saline with calcium and magnesium (DPBS w/ Ca & Mg) to remove OCT (Optimal Cutting Temperature) compound. OCT is

the embedding medium used to prepare frozen tissue for cutting. Once the tissue rinsed it was submerged in a dye solution of either MB or TB and rinsed again in DPBS. Some of the tumors were briefly rinsed in 3% acetic acid and then imaged with the multi-spectral confocal system at 830nm, 660nm, 650nm, or 630nm. The images were then processed and compared with each other and histology. Tumor samples imaged immediately imaged best. On some occasions it was not possible to image immediately and the samples had to be fixed with formalin. After fixing the samples became stiff and did not flatten as well. The tissue edges could not always be imaged. Overall the fixing did not have a significant impact as long as the samples were imaged within a reasonable time. Tissue structures could still be seen and tumors margins were still distinguishable. To see the value added by using the contrast agents in multi-spectral confocal microscopy, images of the tumors with and without contrast agents were taken and compared. Multi-spectral confocal images were taken with the tissue stained with either MB or TB and acetic acid.

6.2. Processing of Images

To compare the confocal images with the full histology slide of the excised tumor mosaics of the confocal images were created using the VivaScope software. The mosaics also aided in the registration of the confocal images with histology. The VivaScope software saves each individual image used to create a low resolution mosaic on the display but does not correctly save the mosaic. Matlab was used to create high resolution mosaics by piecing together the individual images. A Matlab function was created to read in individual images acquired by the VivaScope mapping software, remove predetermined overlapping pixels, and correctly map the images. The mosaics are

composed of 144 individual images each of size 480x640 and each image is about 600um by 800um. The mosaic size is 4860x6323 and covers a field of view of about 6mm by 7.5mm. The images are then registered with each other by inspection and evaluated.

7. Results

Ex-vivo multi-spectral confocal images of excised non-melanoma skin cancer were imaged with a lateral resolution of 1.2μm at 830, 660, 650, and 630 nm and axial resolution between 5-8μm for 660, 650, 630 nm and 7-8μm for 830nm light. The measured resolutions agree closely with the calculated. Water was used as the immersion medium for the objective lens. The samples were moved axially to correct for focal length shifts when switching the imaging wavelength.

Mosaics were taken to register the confocal images with histopathology, to orientate the images and match morphology details. Mosaics and single images were compared to histology. Figures 7-14 to 7-23 have their corresponding hematoxylin and eosin (H&E) images, histology slide image. The H&E images were scanned or imaged with a microscope to obtain a digital copy of the H&E image. Other images that do not have a corresponding H&E image are shown as well. Those images are compared to each other to show the differences in contrast in the tumor areas. Figure 7-3 shows an image of paper stained with MB to demonstrate dye absorption with red light and not in 830 nm. Figure 7-24 is an *in-vivo* image of mouse tissue to demonstrate the potential capability to image *in-vivo.* Figure 7-10 is the only image taken with the 660nm diode laser and PMT detector. The VivaScope electronics board induced noise onto the PMT circuit. The noise from the PMT circuit measured using an oscilloscope was about 200mV peak to peak, which corresponds to an average digital count of 15. A dark image

captured with the PMT detector had a maximum digital count of 14, average of 1.67, and standard deviation of 2.17. Further use of the PMT detector was discontinued because of the noise.

The images that follow show multi-spectral confocal images of BCC, BCC infiltrative, BCC nodular, and SCC stained with either MB or TB and in some instances rinsed with acetic acid.

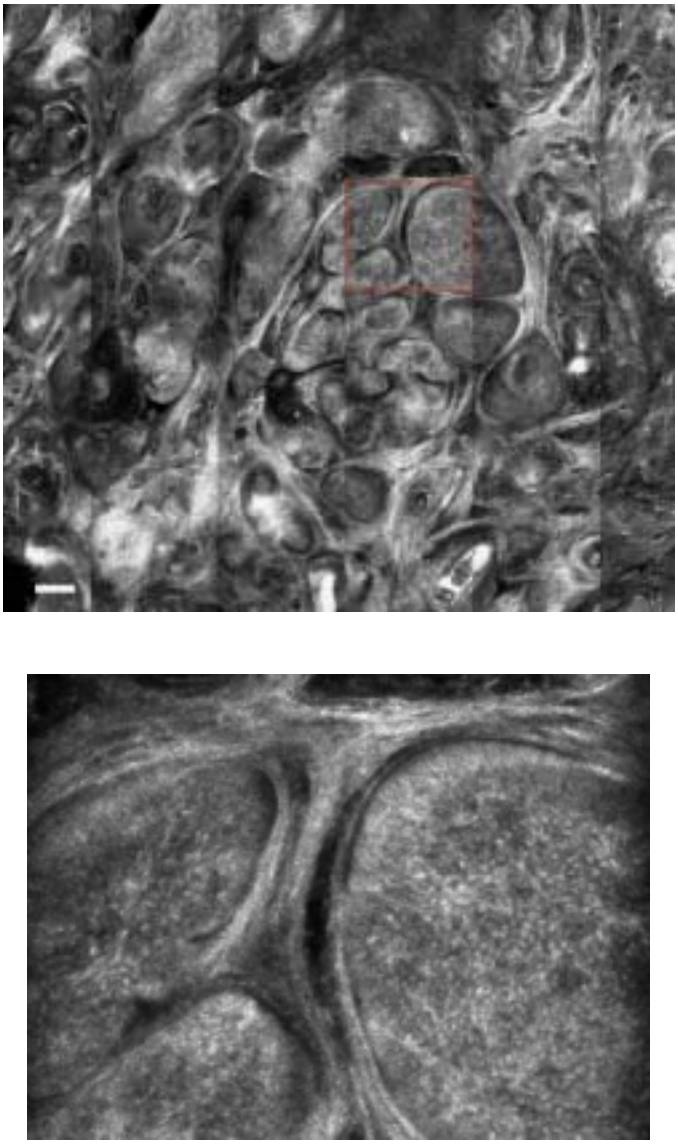

Figure 7-1

This image demonstrates the stitch of the confocal images to create a mosaic. This is an image of BCC, stained with MB 0.1 mg/ml, imaged at 830nm, and was excised from the right nasal slope. The scale bar on the mosaic is 200μm. The bottom image is a single image, which is the outlined square on the mosaic. Tumor lobules are clearly visible on the confocal image.

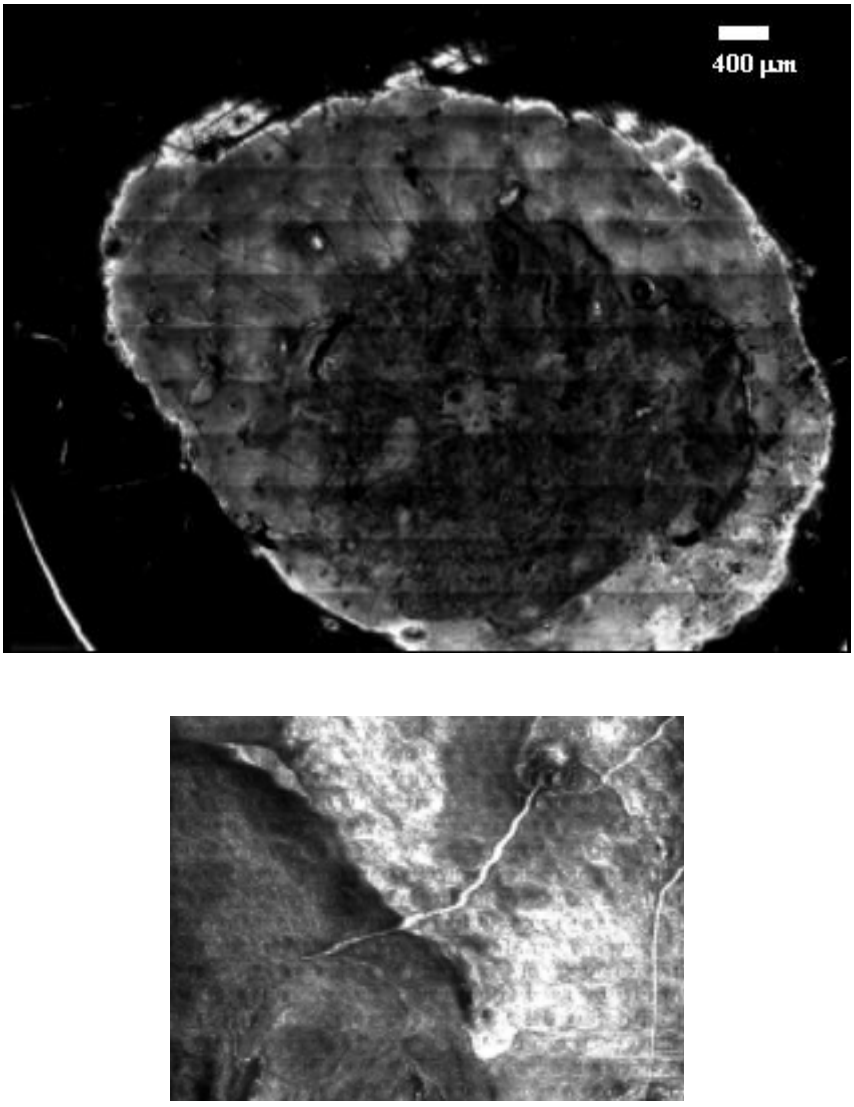

Figure 7-2

The tumor margin is clearly visible in the image above. This is a confocal image of tissue with micro-nodular BCC, stained with MB 0.1 mg/ml, imaged at 633nm, and excised from the left chin. The tumor is in the center of the tissue. The tumor area is darker than the healthy tissue. This is a trivial case. The tumor would also be distinguishable at 830nm. The dye gives additional contrast from the tumor to the healthy tissue. The image on the bottom is a single image taken closer to the surface of the tissue.

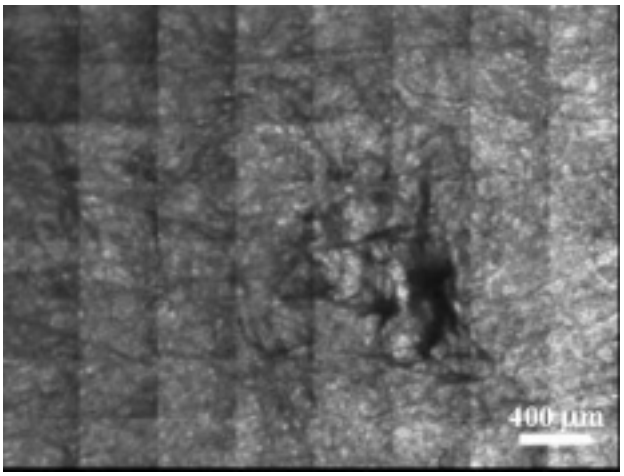

830 nm

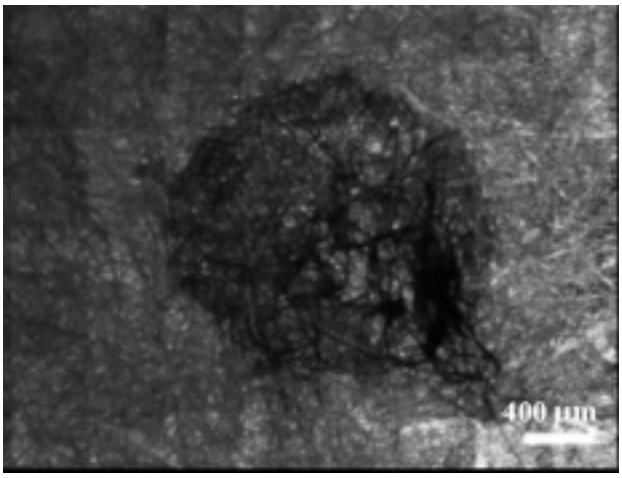

630 nm

Figure 7-3

Clear white paper was stained with 0.25 mg/ml of MB in order to test and demonstrate the dye localization capability of the multi-spectral confocal microscope. The area where the dye was applied absorbs the 630nm light and not the 830nm light. A tiny dot of MB was applied to the paper using a syringe. The diameter of the spot is about 1.2mm. The dot is clearly visible at 630nm and at 830nm the impact of the syringe on the paper is visible but not the circle containing the MB dye.

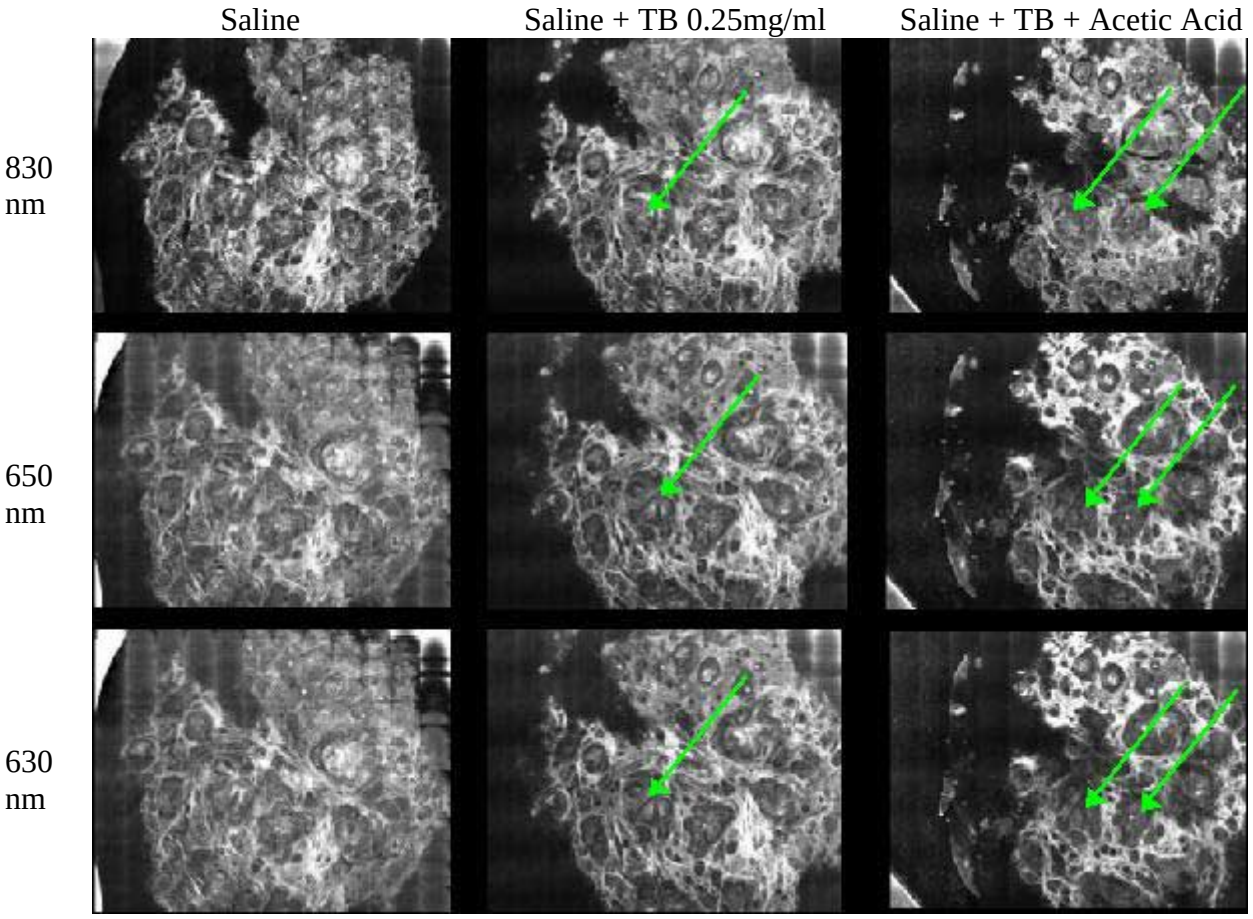

Figure 7-4

Tissue with BCC was imaged at 830, 650, and 630 with only saline, then the same tissue was stained with 0.25 mg/ml of TB and imaged, and finally the same tissue was rinsed in 3% acetic acid and imaged. The orientation and depth was maintained as closely as possible throughout the imaging process. The tumor is in the center of the tissue, the green arrows point to an area where the dye was retained and imaged darker with 650 and 630 nm light compared to 830 nm light. There is an increase in contrast in the saline and TB image, but the contrast is best in the saline, TB, and acetic acid image. Acetic acid increases scattering from the tissue increasing tumor and collagen contrast in the 650 and

630 nm images. The areas that imaged darker in 650 and 630 compared to 830 nm are possible tumor areas, but would need further morphological detail to verify it is tumor. Sebaceous glands were found to image dark as well with red wavelength light. This sample was taken from the left part of the nose and the nose is known to has large sebaceous glands.

Figure 7-5

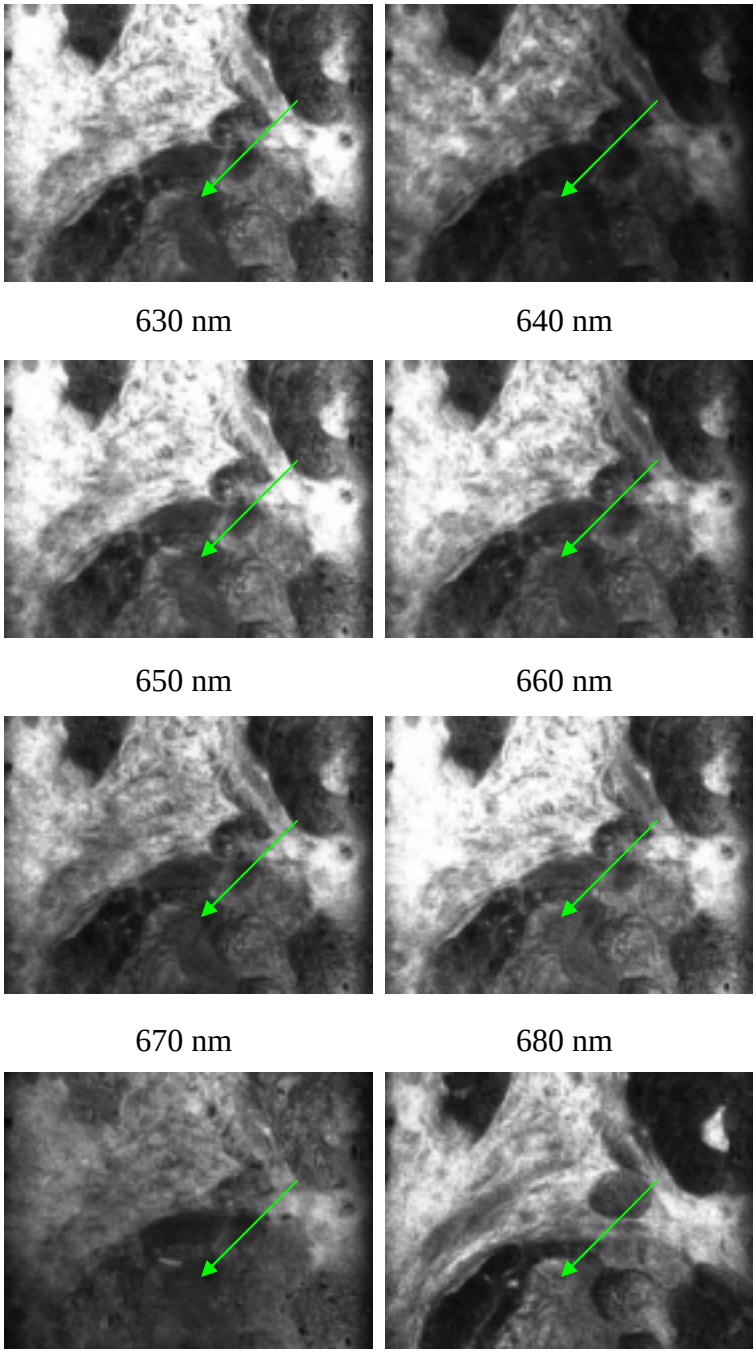

The multi-spectral confocal microscope is capable of imaging with 630 to 690 nm light using the Dye laser. Multi-spectral confocal images were taken from 630 to 690 nm and with 830 nm light. The lasers output power was measured and kept equal for the different wavelengths. The Dye laser is also capable of imaging with 620 nm light, but the output power was to low. The tissue was moved axially to adjust for focal length shifts due to chromatic aberrations. These confocal images are from excised tissue with SCC, stained with TB at a concentration of 0.15 mg/ml,and rinsed with acetic acid.

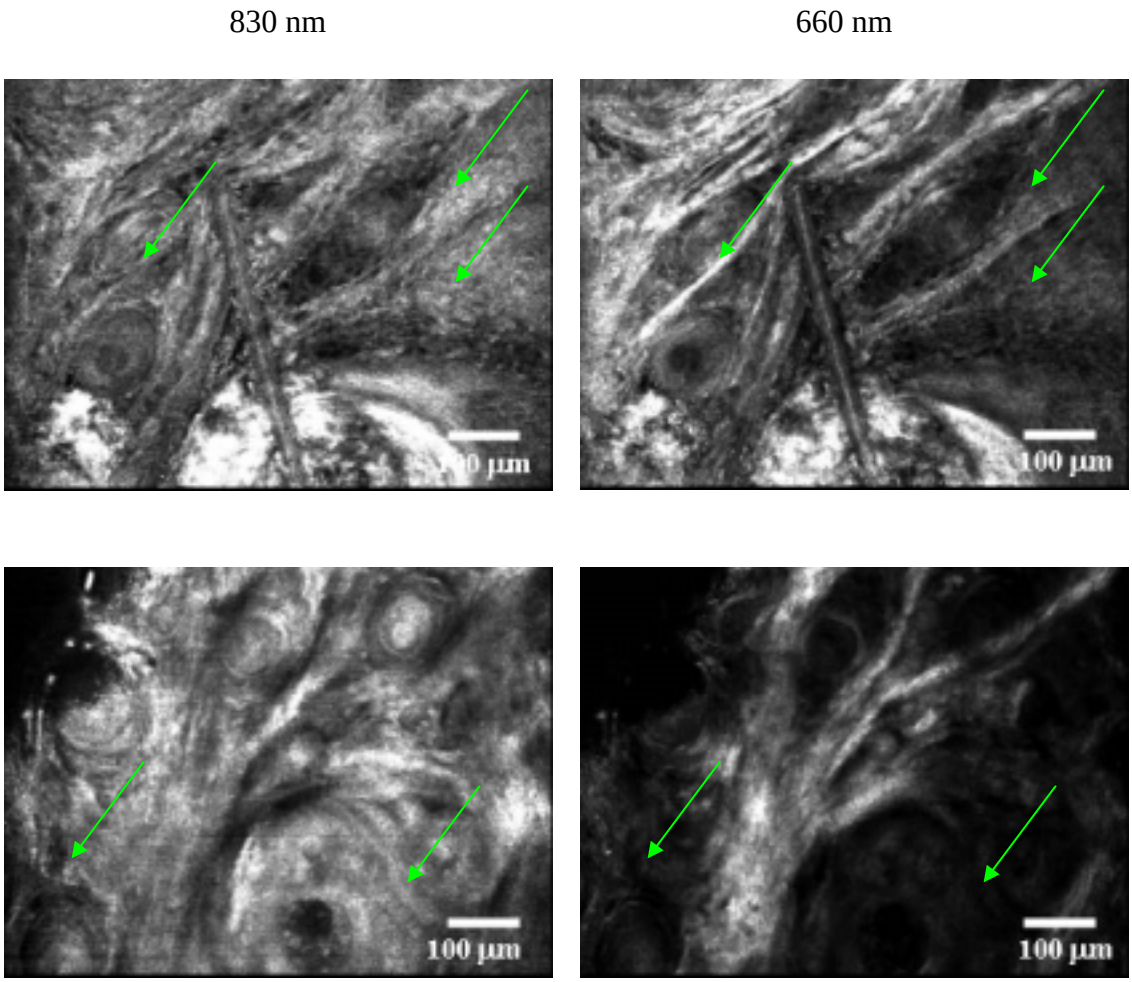

Figure 7-6

These multi-spectral confocal images show that hair follicles and hair shafts image similarly with red light and 830 nm light and demonstrates dye localization. Collagen strains can be seen more clearly in the 660 nm image compared to the 830 nm image (top image). This is probably because there is more scattering with 660 nm than 830 nm. This tissue sample has BCC stained with 0.15 mg/ml of TB and rinsed in acetic acid. The tumor lesion was from the left nasal. The green arrows point out differences in brightness and darkness in the top and bottom images. The areas where the TB is localized is clearly visible in the bottom image.

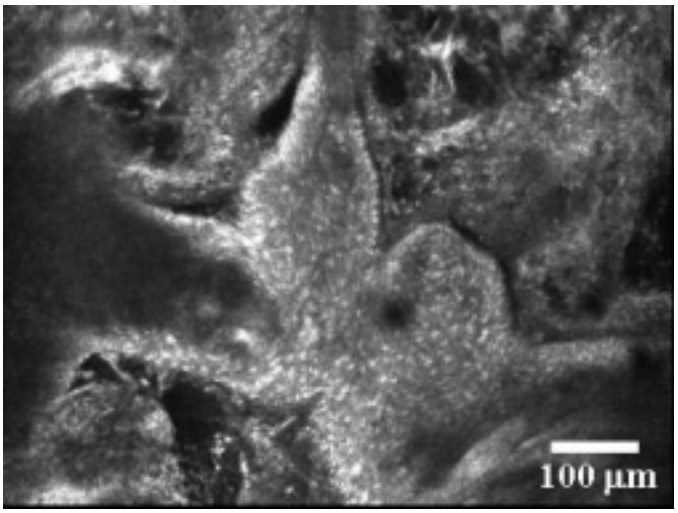

830 nm

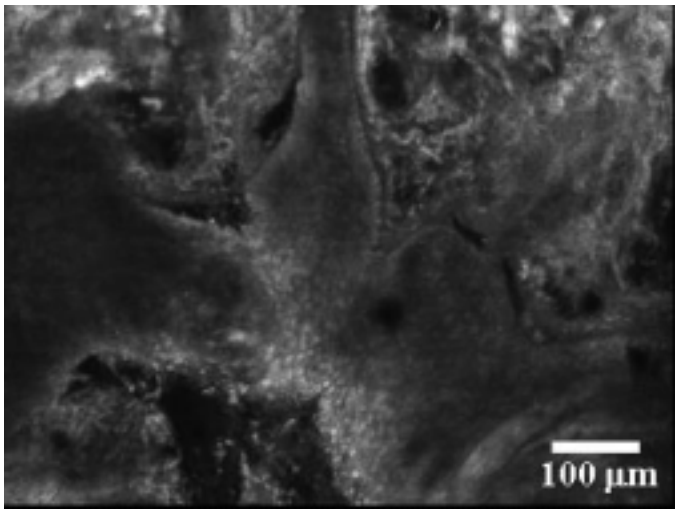

630 nm

Figure 7-7

Confocal image of infiltrative BCC stained with 0.12 mg/ml of MB and rinsed with acetic acid. The tumor lesion was from the right temple. The confocal images above show dye uptake and aceto whiting. The cell nuclei appear bright in the 830 nm confocal image. When imaged with 630 nm light the cell nucleus is still visible but do not appear as bright, because the dye is localized in the cell's cytoplasm.

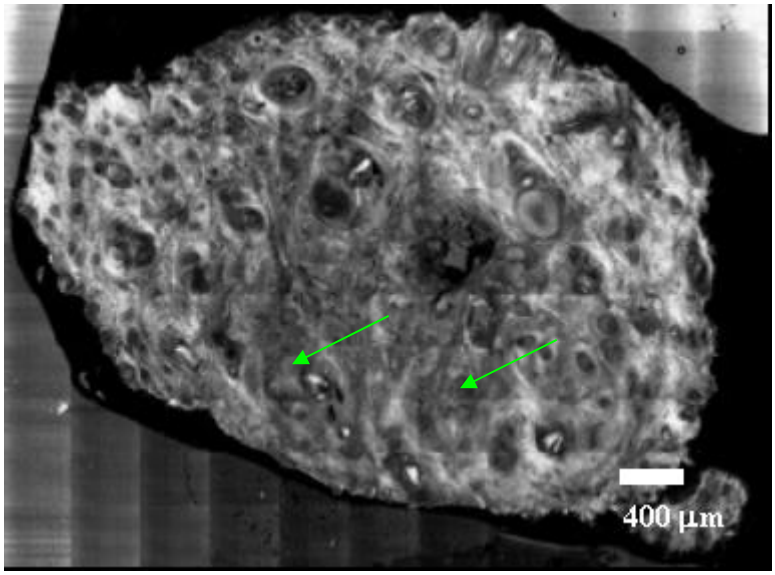

830 nm

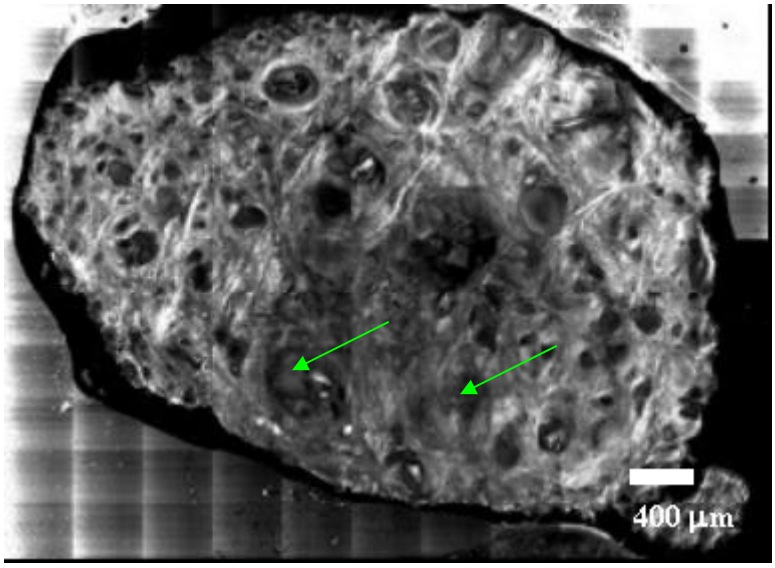

660 nm

Figure 7-8

Confocal image of tissue with BCC, stained with 0.15mg/ml of TB. The arrows points to areas where the dye is localized. The tumor is in the center of the tissue, which is dark with 830 nm and slightly darker with 660 nm compared to the rest of the tissue.

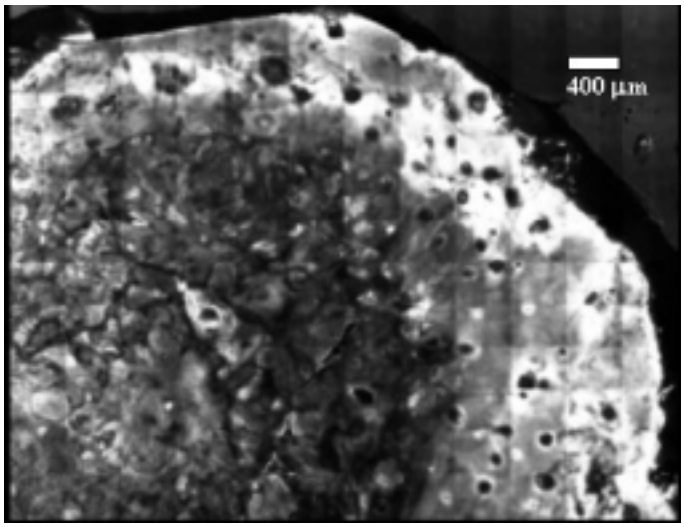

830 nm

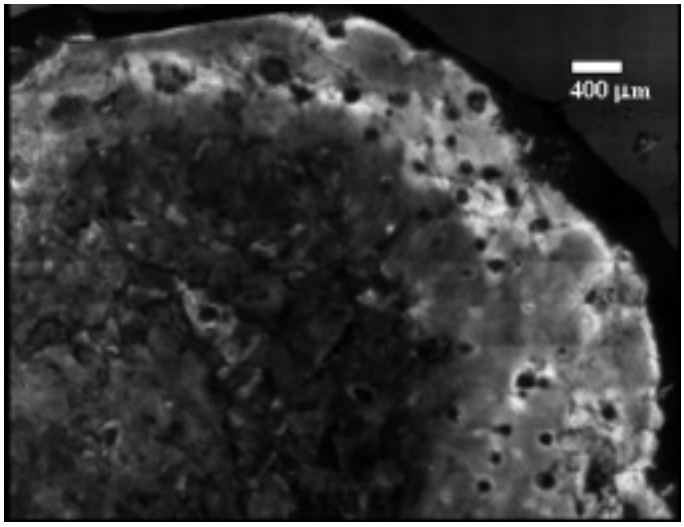

650 nm

Figure 7-9

Confocal image of tissue excised from the mid forehead with BCC that was stained with 0.1 mg/ml of MB. The tumor is in the center of the sample. The tumor images dark in both 830 and 650 nm light, but the tumor is darker in the 650 nm image compared to the 830 nm image because of the dye absorption of 650 nm light.

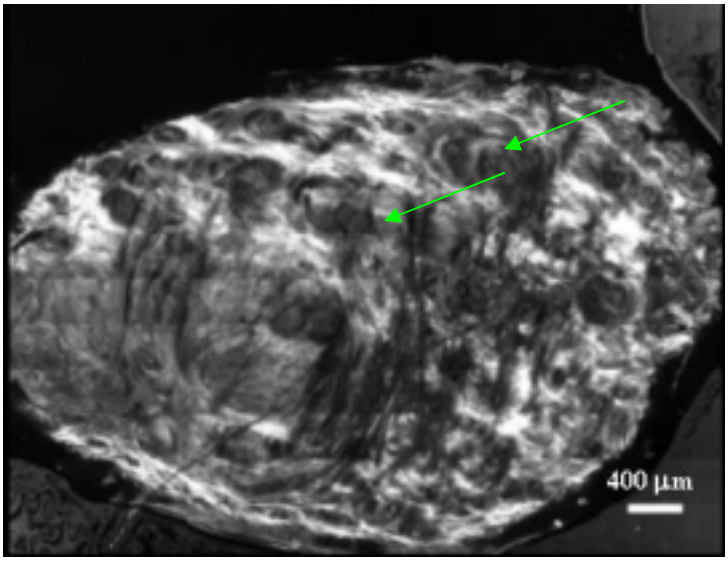

830 nm

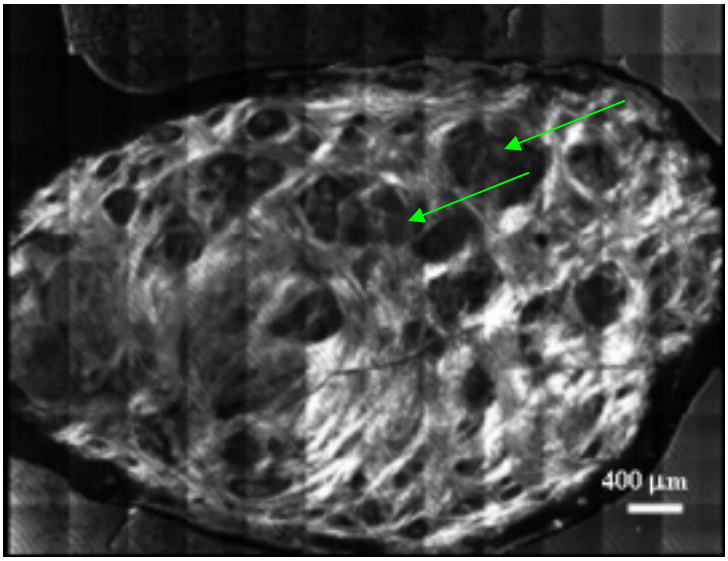

660 nm
Diode laser

Figure 7-10

Confocal image of skin with BCC, stained with 0.15 mg/ml of MB. The arrows point to areas where the dye is localized. Those areas image darker at 660 nm compared to the 830 nm image. The laser source used was the 660 nm Lepton II diode laser and the detector was the PMT.

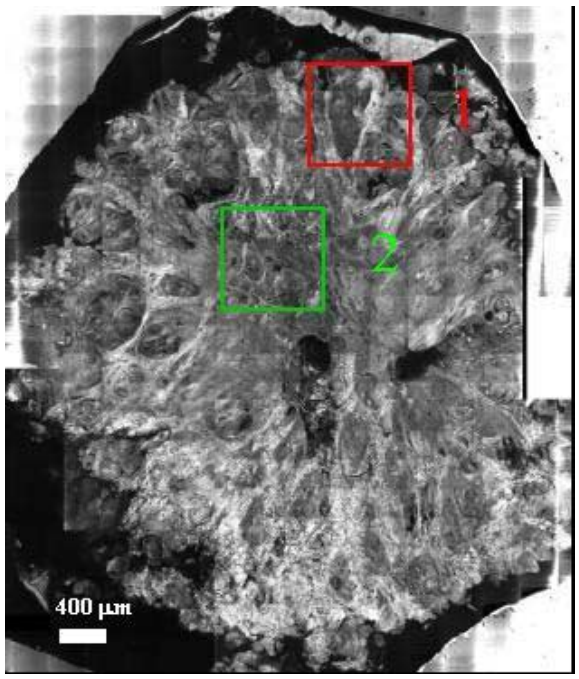

830 nm

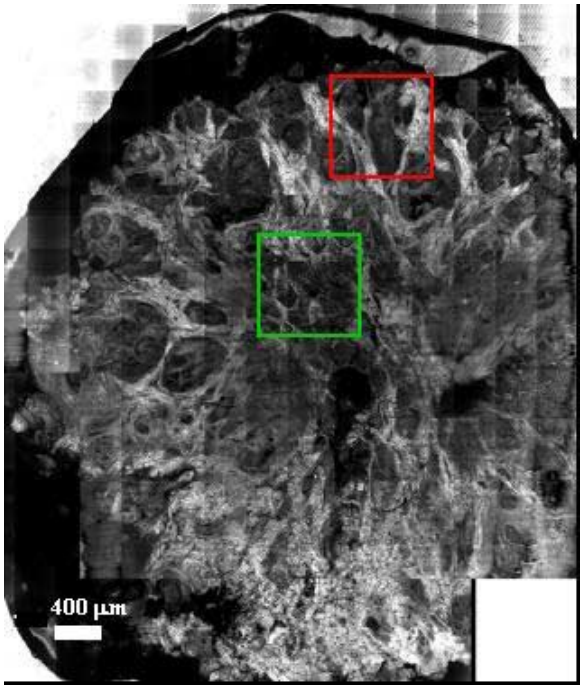

630 nm

Figure 7-11

Confocal image of tissue with infiltrative and nodular BCC stained with TB 0.1mg/ml.

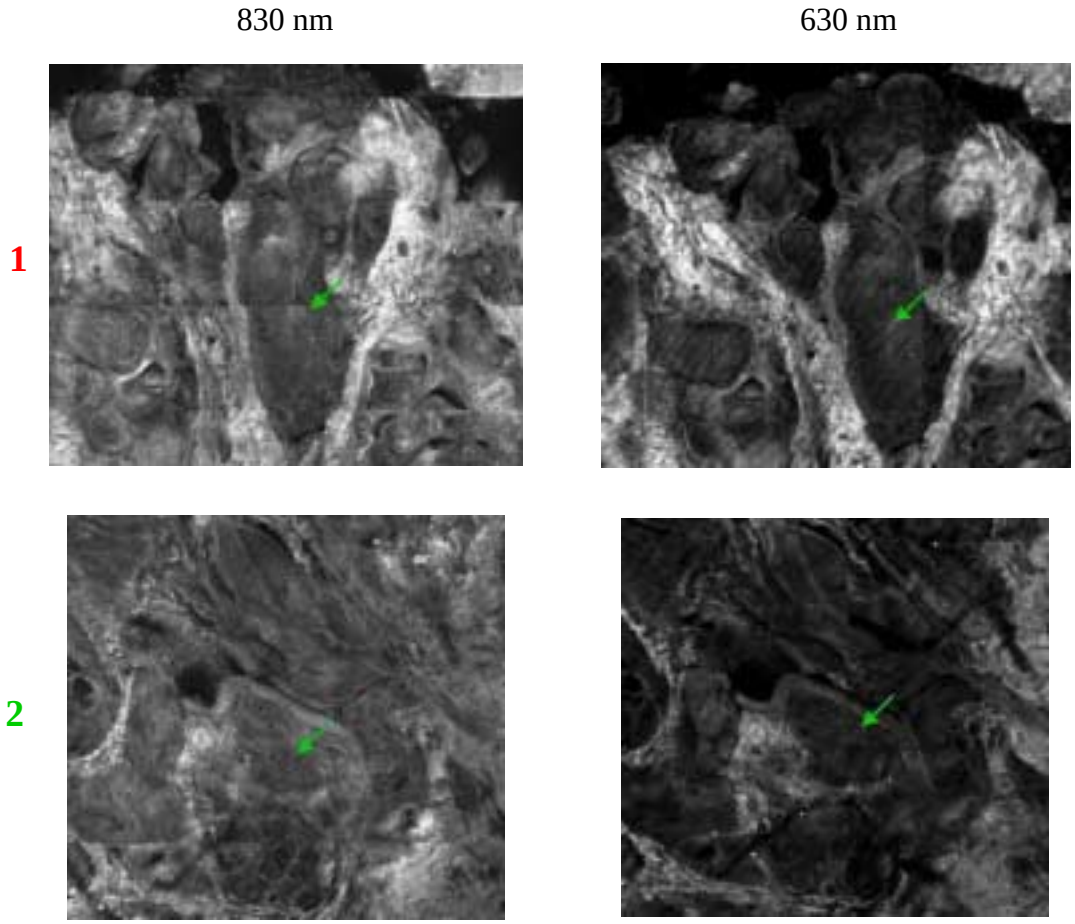

Figure 7-12

These two sets of confocal images are zoomed in images from square 1 and square 2 outlines of Figure 7-11. The arrows point out tumor lobules that are darker in the 630 nm images compared to the 830 nm images, due to the localization of the dyes in the tumor. This sample was preserved in formalin and imaged two days later. Confocal images of tissue that was imaged immediately imaged best but was not always possible. Tissue that was stored in a refrigerator in a veil with formalin imaged fairly well as long as they were imaged within a few days.

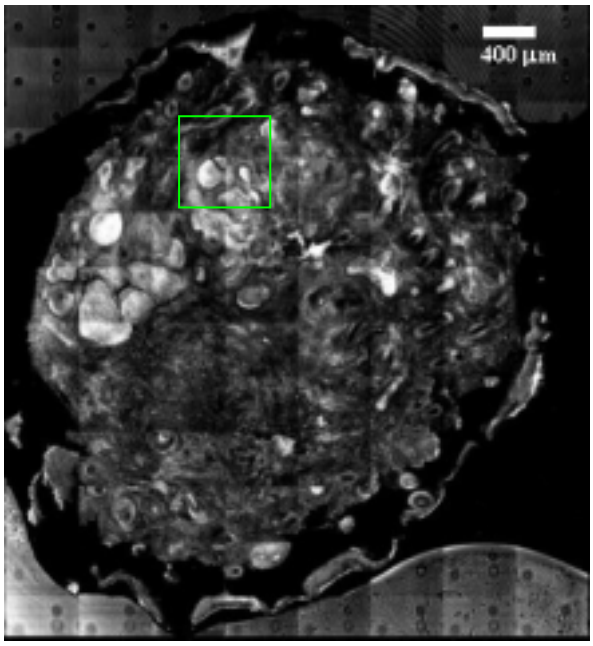

830 nm

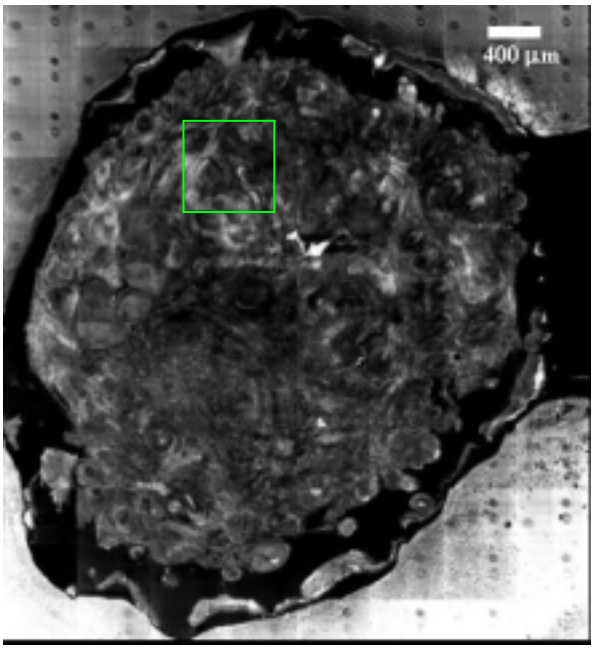

630 nm

Figure 7-13

Confocal image of skin with BCC stained with 0.1 mg/ml of MB 0.1 and then rinsed in acetic acid.

Figure 7-14

These confocal images are taken from the mosaic of Figure 7-13, from within the square outline. The lesion was from the left eyelid. The arrows point to tumor lobules, which appear darker in the 630 nm image compared to the 830 nm image. The same tumor lobules can be seen in the H&E image. The tumor specimens we received from the Mohs surgeon are after the Mohs sections for histology slides. Therefore the histology slides are at a different plane and the tissue has been processed for Mohs. We have also processed the tissue for imaging with the multi-spectral confocal microscope. Therefore the size and shape of the tumor is different.

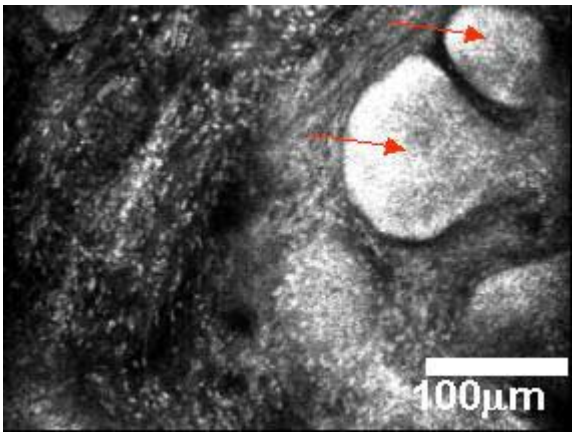

830 nm

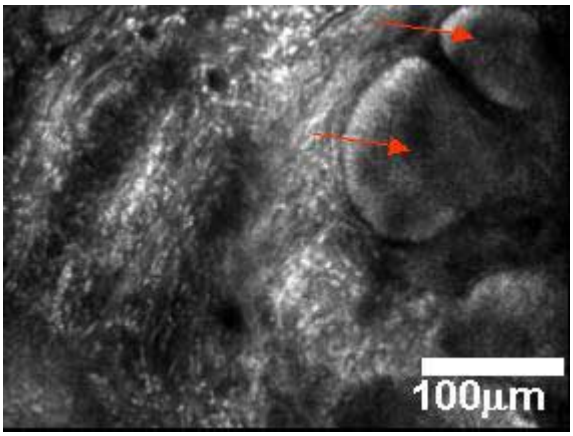

630 nm

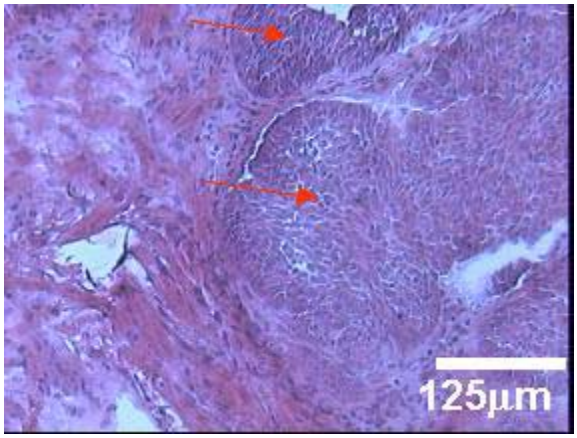

H&E

Figure 7-15

Confocal image of infiltrative BCC stained with 0.2 mg/ml of MB. The arrow points to a location where there is a tumor lobule, which appears darker in the 630 nm image compared to the 830 nm image. There is more contrast in the 630 nm image. The fingers of the infiltrative tumor can be seen in the 630 nm confocal image and the corresponding H&E image. The same tumor lobules in the confocal images can be seen in the H&E image.

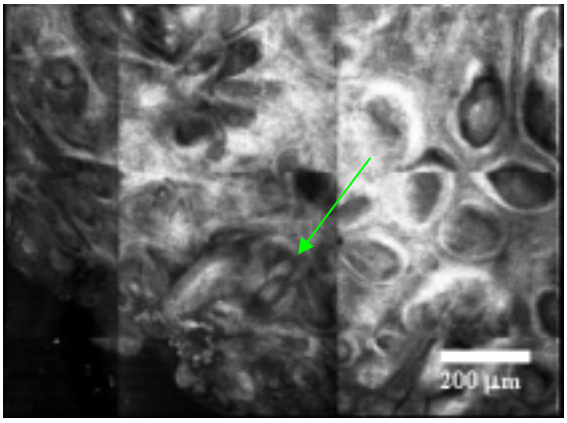

830 nm

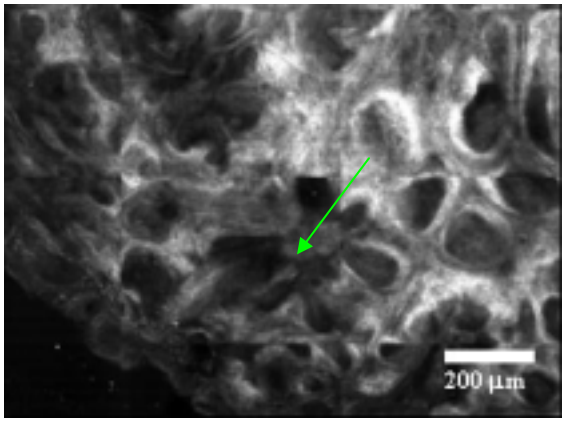

630 nm

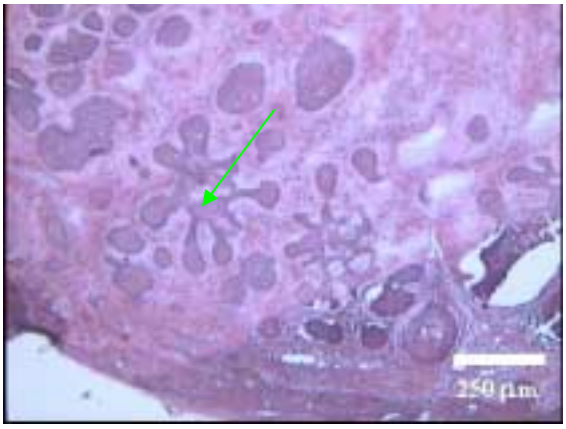

H&E

Figure 7-16

Confocal image of BCC stained with 0.2 mg/ml of MB. The red arrow points to a location where there is a tumor lobule, which appears darker in the 630 nm image compared to the 830 nm image. The dye retained in the tumor and rinsed from the healthy tissue. The area surrounding the tumor, imaged similarly in both 830 nm and 630 nm confocal images. The green arrow points to a sebaceous gland which images dark in both 830 nm and 630 nm images. The same tumor and sebaceous gland can be seen in the H&E image.

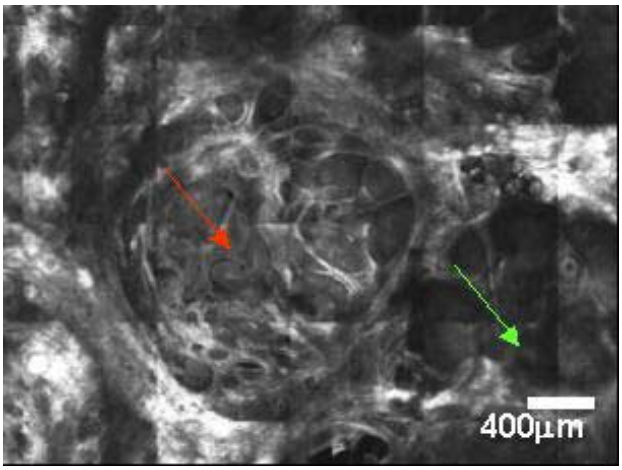

830 nm

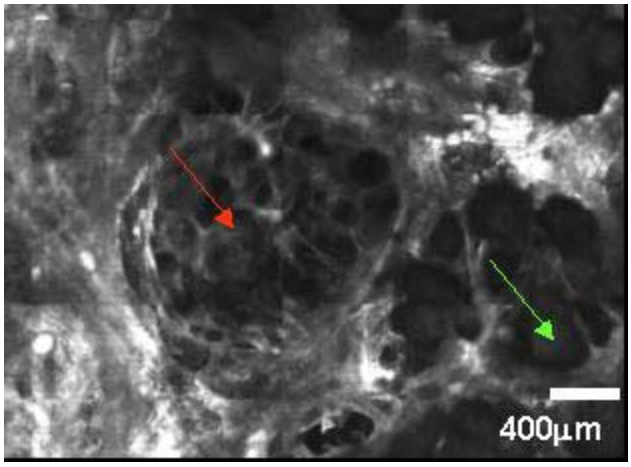

630 nm

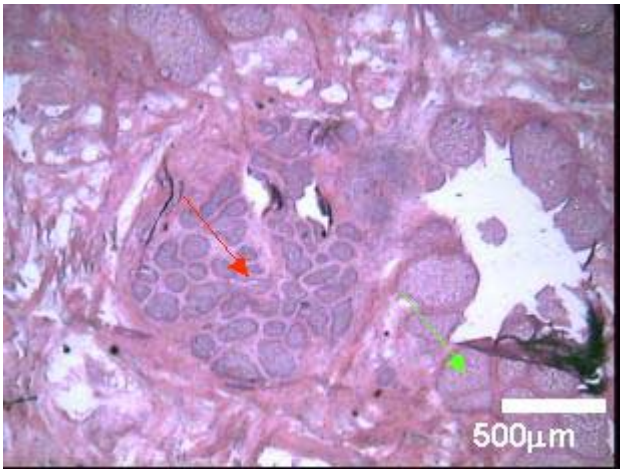

H&E

Figure 7-17

Confocal mosaic of infiltrative BCC stained with 0.2 mg/ml of MB. The H&E image outlines the tumor margin. The 630 nm shows the margins of the tumor with good agreement with histology image. The tumor margin is darker in the 630 nm image compared to the 830 nm image. The tumor consumes most of the tissue. This tissue sample was excised from the right upper lip.

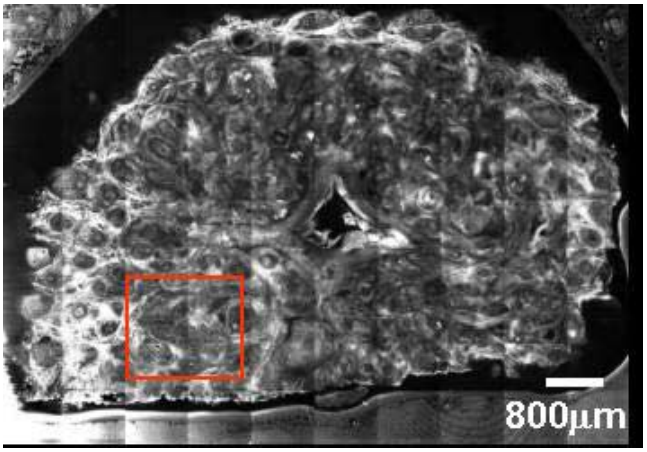

830 nm

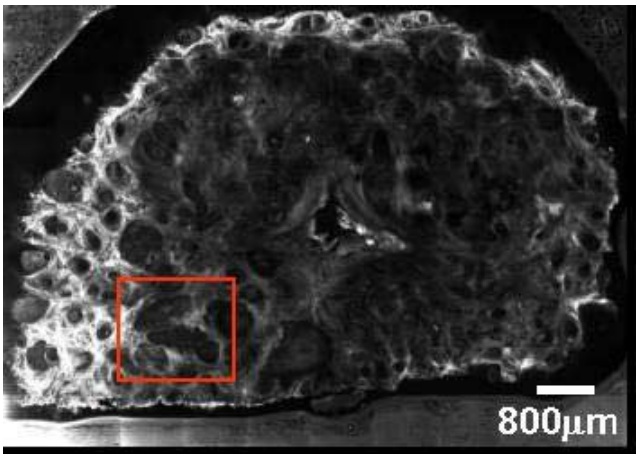

630 nm

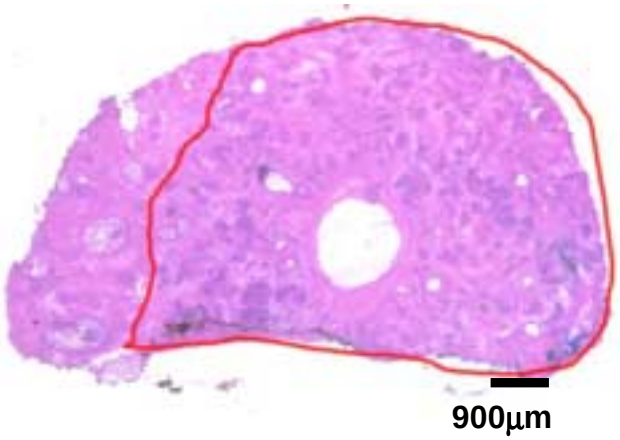

H&E

Figure 7-18

These confocal images were taken from the square drawn in Figure 7-19. The tumor appears darker in the 630 nm image compared to the 830 nm image. The tumor can be seen in all three images 830, 630, and H&E. The added contrast by the dye in the 630 nm image makes the tumor margins more visible than the same tumor in the 830 nm image. Again the H&E images are at a different plane and therefore have slightly a different shape.

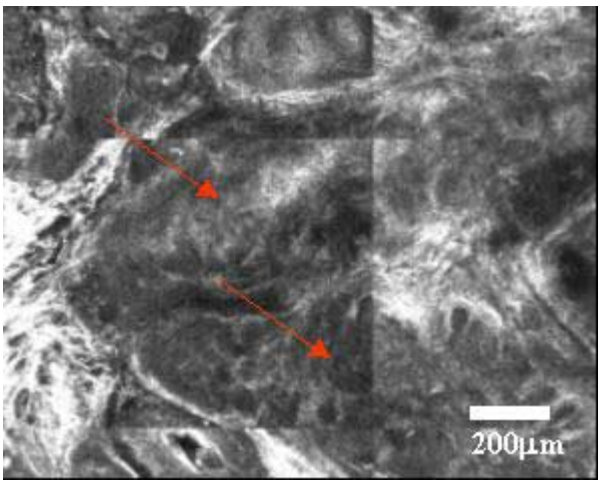

830 nm

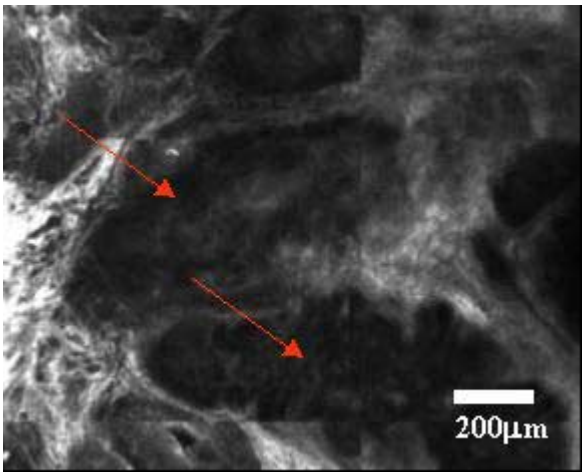

630 nm

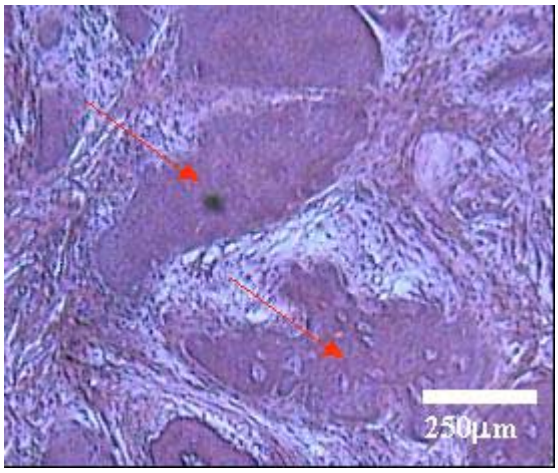

H&E

Figure 7-19

Confocal mosaic of excised skin with BCC, from the nasal tip. This sample was stained with 0.25 mg/ml of toluidine blue dye and then rinsed in acetic acid. The H&E image is of the highlighted area. The tumor imaged darker in the 650nm image than 830nm image.

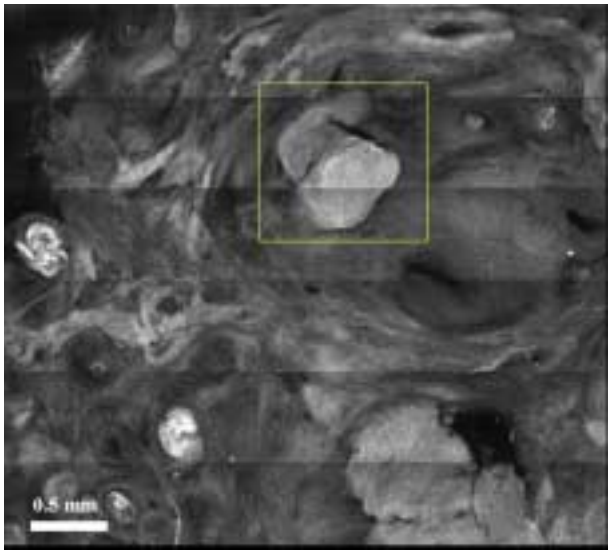

830 nm

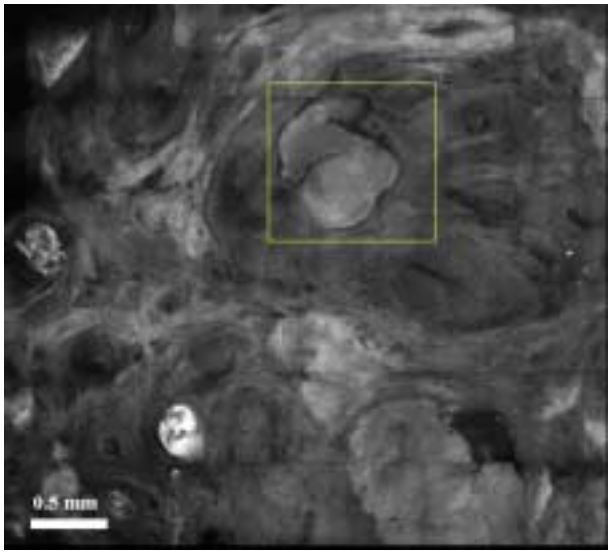

650 nm

H&E

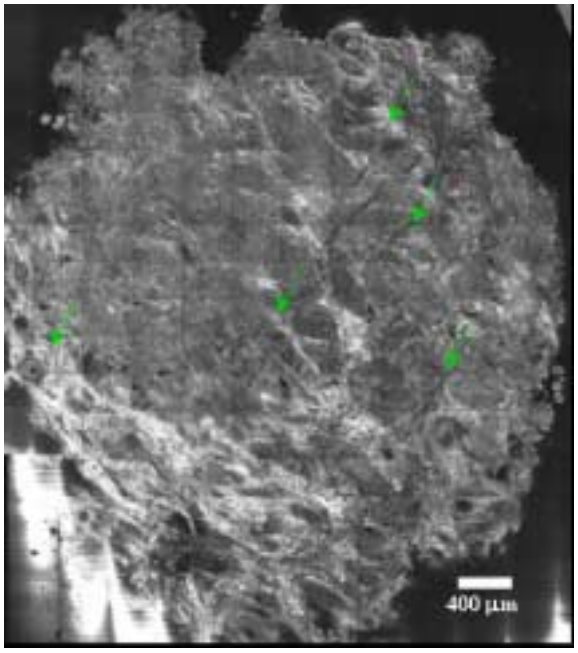

830 nm

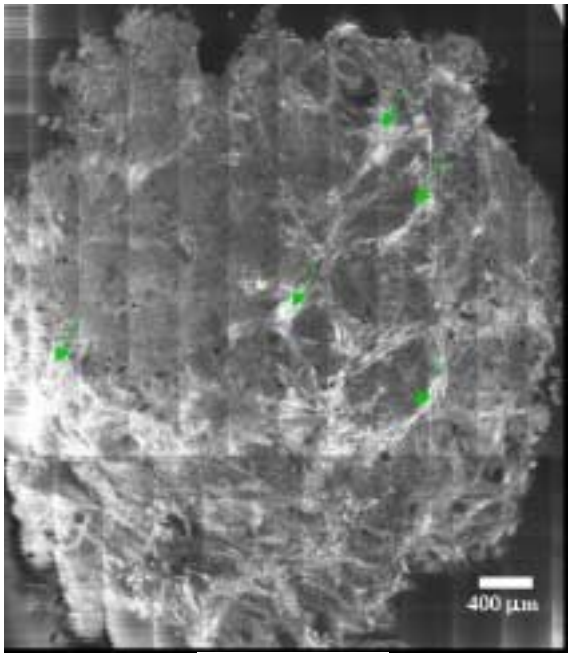

630 nm

Figure 7-20

Confocal image of excised skin with BCC, stained with 0.05 mg/ml of TB. This sample was kept in formalin and imaged two days later. The tumor is outlined in the H&E image. The arrows in the 830 nm and 630 nm images show areas where there are differences in the images. There is more tumor contrast in the 630 nm image.

H&E

Figure 7-21

Confocal image of excised skin with BCC, stained with 0.15 mg/ml of TB. The H&E image outlines the tumor margin. The tumor is visible in both the 830 nm and 630 nm image. There is not much visible difference between the 830 nm and 630 nm confocal images. This sample was over stained with TB and then imaged without the dye completely rinsing away from the healthy tissue. The tumor also imaged dark in the 830 nm image as well.

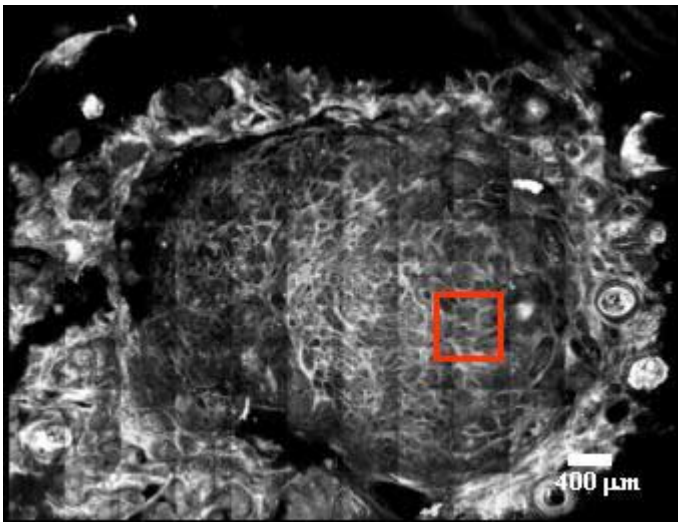

830 nm

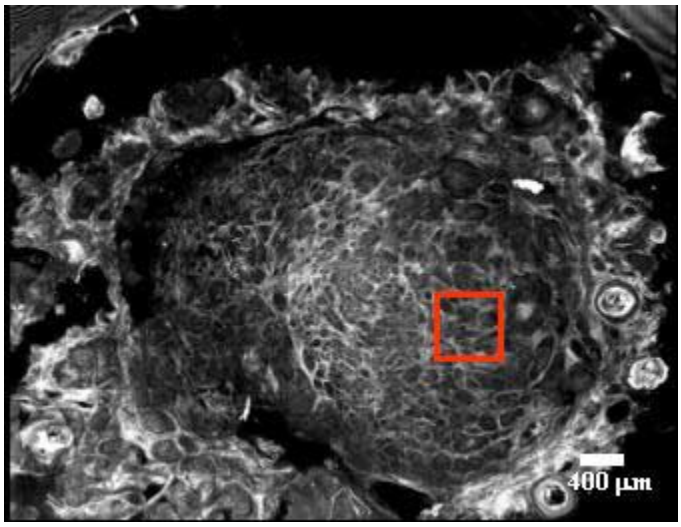

660 nm

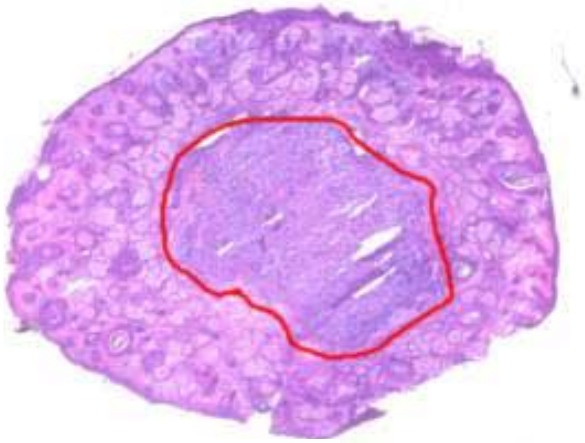

H&E

Figure 7-22

These confocal images were taken from the mosaic of Figure 7-21, from within the outline of the square. By zooming in it can be seen that the 660 nm and 630 nm imaged darker and there is slight improvement in contrast. The arrows point to a tumor lobule.

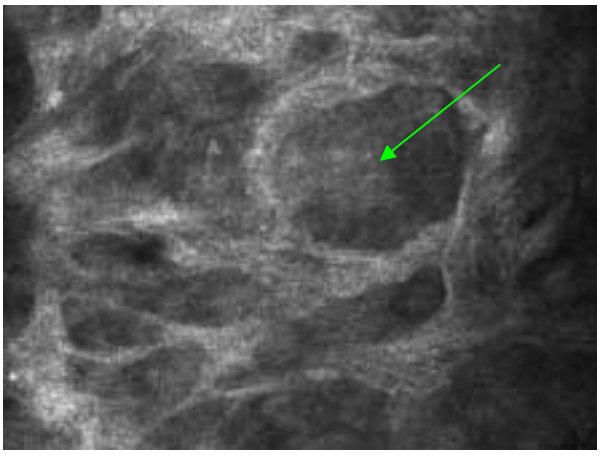

830 nm

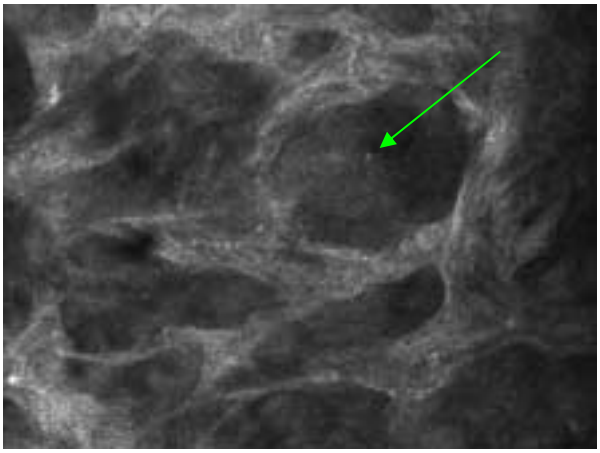

660 nm

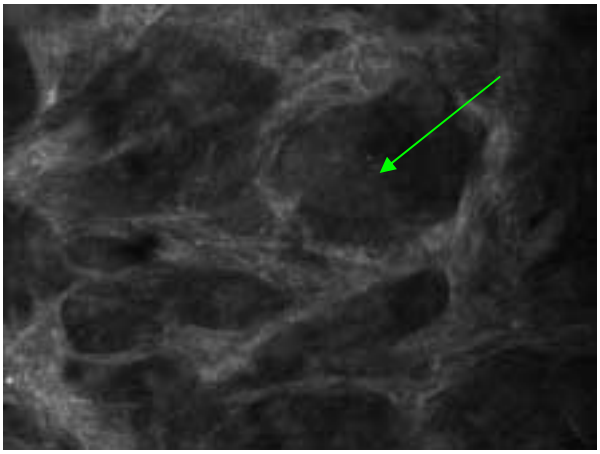

630 nm

830 nm 660 nm

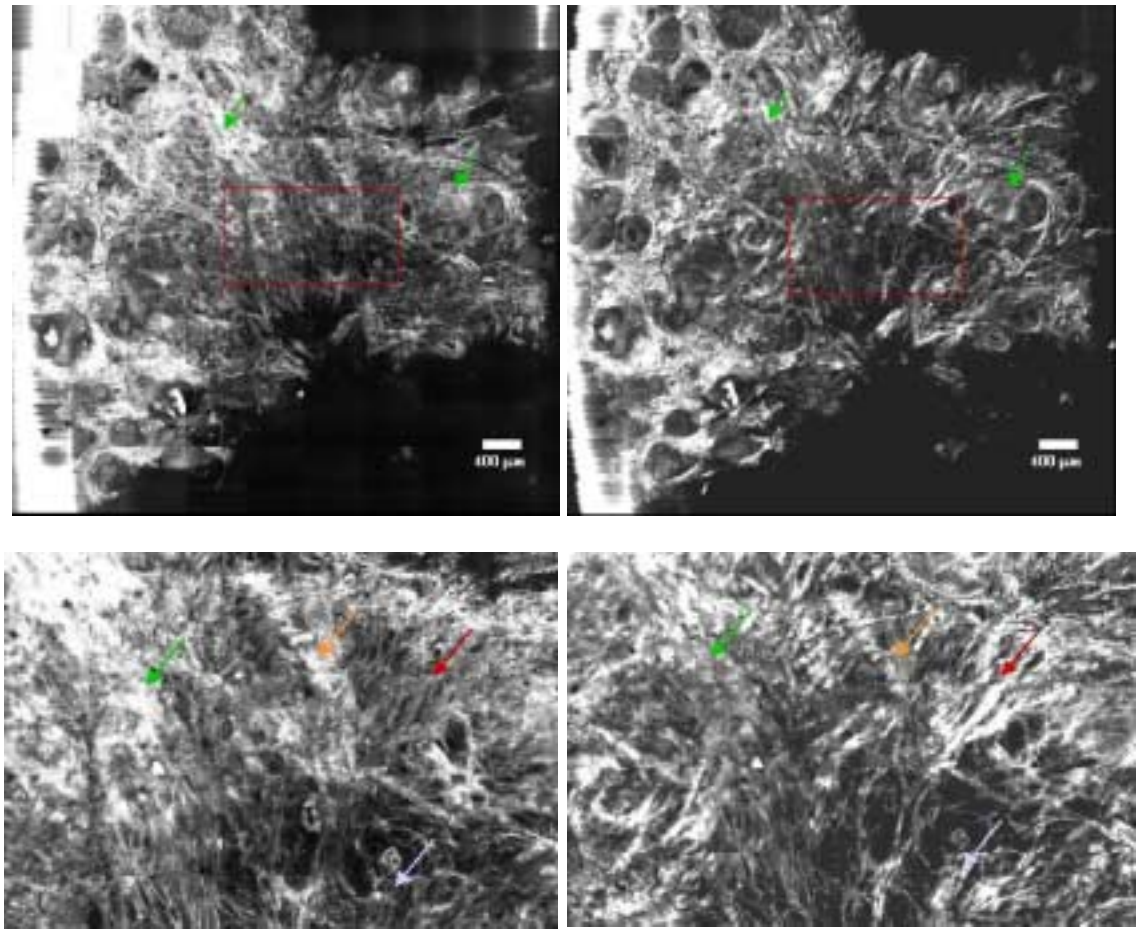

Figure 7-23

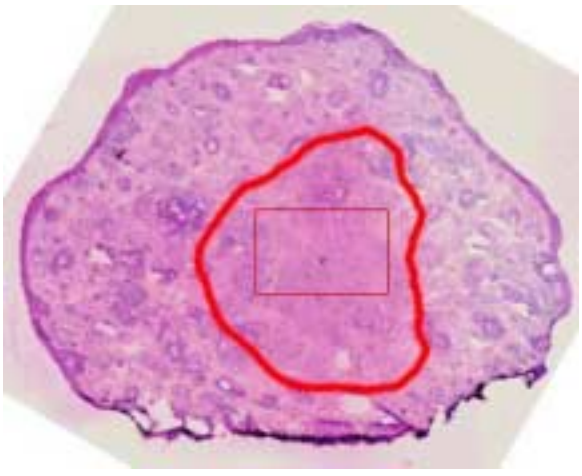

The top confocal images are from part of a mosaic and the bottom confocal images are from the square outline of the top images. The tumor type is infiltrative BCC, excised from the nose, and stained with 0.01 mg/ml of TB. The arrows point to differences in the 830 nm and 660 nm images. The H&E image outlines the tumor. The confocal images are within the outlined tumor region.

Mouse skin *in-vivo* at 830 nm

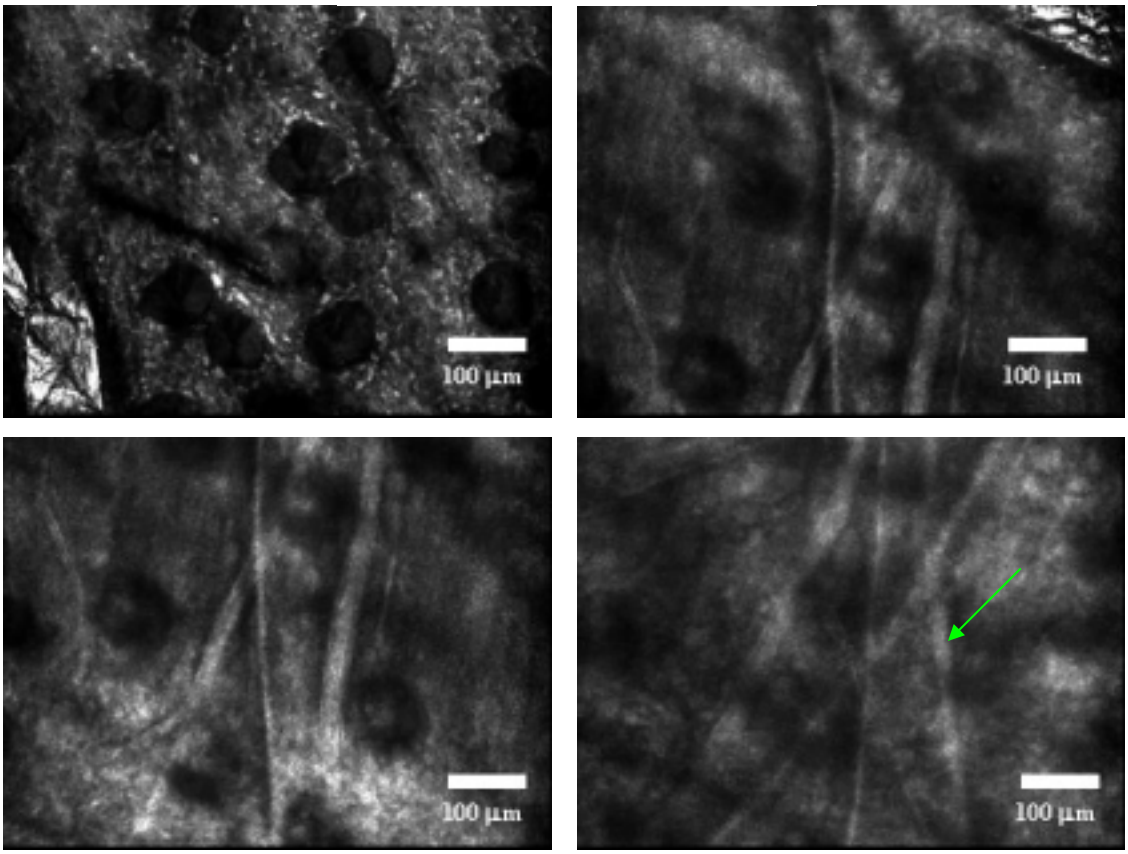

Figure 7-24

A mouse was anesthetized and secured to the VivaScope stage. The ear of the mouse was imaged *in-vivo* with 830 nm light. Blood flow from tiny blood vessels could be seen in real time with the confocal microscope. The green arrow points to a blood vessel. Confocal images with 660, 650, and 630 nm wavelengths were not possible, there was insufficient returned light from the tissue to generate sufficient signal with the APD detector in place. Also 660, 650, and 630 nm light do not image as deep as 830 nm light. The working distance of the 20x objective lens is 300 microns and the cover slip thickness is 170 microns. This left 130 microns of mouse tissue that could be imaged.

8. Conclusions

8.1. Summary

In this project a multi-spectral confocal microscope that operates at selectable wavelengths between 620 to 690 nm and 830 nm was developed. The operator selects the imaging wavelength without having any major impact on the system. The wavelengths between 620 nm to 690 nm were chosen with the intent to target the absorption band of methylene blue and toluidine blue. The 830 nm source was used as a comparison to the 620 to 690 nm images, since it is not in the absorption band of the dyes. A Dye laser was used to provide the 620 to 690 nm wavelength operation. A 660 nm diode laser was also used but required a PMT detector to measure the returned low intensity light. Only one image is shown with the 660 nm diode laser and PMT detector, the rest were taken with the Dye laser and APD detector.

Tumor tissues were stained with various dye concentrations. Specimens stained with methylene blue with concentrations between 0.1 to 0.3 mg/ml and toluidine blue with concentrations between 0.01 to 0.25 mg/ml are presented in the results. Tumor tissue stained with low dye concentrations were found to image best using the multi-spectral confocal microscope. The tumor staining and rinsing process was closely monitored. The tissue was checked frequently to prevent excessive dye uptake, over stained tissue took longer to rinse. The staining time depended on the tissue dye uptake, which varied from tissue to tissue, but in general was kept within 10 minutes or less.

The tissue staining and rinsing process was sometimes followed by a brief rinse in acetic acid. The following was used as a guide to when to rinse tissue in acetic acid. Excised tissue with tumor near the epidermis was not rinsed in acetic acid. Tumor well

in the dermis was rinsed in acetic acid. Patterns of cells in the dermis are most likely tumor and are more visible when rinsed in acetic acid.

Multi-spectral confocal images of excised non-melanoma tumor tissue showed improvement in contrast when dye and acetic acid was applied. By scanning the dye laser wavelengths, it was found that the images taken at 630 nm, 650 nm, and 660 nm gave the best contrast. Tissue stained with TB imaged best with 660nm and tissue stained with MB imaged best with 630 nm. Localization of the dyes retained in the tumor was possible with the multi-spectral confocal microscope. The tumor margins imaged darker with 630 nm, 650 nm, or 660 nm light compared to the 830 nm light. Morphological detail with an imaging lateral resolution of 1.2 microns and axial resolution between 5 to 8 microns can be used to further investigate the area in question. The 830 nm laser source can be used to image deeper in the tissue to gain addition structural detail. Tissue structures such as sebaceous glands were found to image dark in red light and 830 nm light. Morphological details would be needed to differentiate them from tumor, especially in the nose where they can be very large. Tumor lobules that do not have basal cells imaged dark with 830 nm light as well, but imaged darker with red light. The tumor lobules with basal cells imaged bright with 830 nm light due to the cell's nucleus and imaged dark with red light due to the dye uptake in the cells. The localization of TB and MB can be seen in the results and the demarcation of the tumor margins is evident in the results with the corresponding histology images.

This work contributed to the publication of [Yaroslavsky 2005], in the Journal of Biomedical Optics, 10(1), 2005. The manuscript can be seen in Appendix D.

8.2. Future Work

The multi-spectral confocal microscope developed in this work has been shown to localize methylene blue and toluidine blue in non-melanoma skin cancer. This method of imaging is not limited to the localization of these dyes in excised non-melanoma tumor. Preliminary confocal images of mouse tissue indicate it is possible to use the multi-spectral confocal microscope to image *in-vivo* as well. Potentially, mouse tissue with non-melanoma skin cancer stained with MB or TB topically or intravenously can be imaged *in-vivo*. This could lead to the imaging of stained human non-melanoma skin cancer *in-vivo*.

Improvements to the system such as the addition of a PMT detector will increase light sensitivity. This would allow imaging with low power laser sources and also the detection of fluorescents by exciting the dyes. Diode laser sources with high power (greater than 60mW) are not readily available in the red wavelengths. The Dye laser beam output used for the imaging experiments is not consistent from wavelength to wavelength, power output fluctuates and the beam characteristic varies. A diode laser would provide more flexibility in terms of portability and be more stable. The use of a PMT detector would allow use of commercially available laser sources. The PMT circuit that was assembled is being redesigned to isolate it from electrical noises that may be present in the operating environment.

Multi-spectral confocal images with higher magnification objective lenses will reveal where exactly in the cell the dyes localize. The highly magnified multi-spectral confocal images may show a dark cytoplasm with a bright nucleus, when the tissue is stained with either MB or TB and rinsed with acetic acid. The second telescope system

magnification would have to be reduced to not lose light by excessively overfilling the entrance aperture of the objective lens. Also the objective lens's entrance aperture has to be at the focal length of the last lens in the telescope tube (See Figure 5-2).

9. References

1 American Cancer Society. Statistics-Cancer Facts and figures 2003. Available at: http://www.cancer.org/docroot/STT/content/STT_1x_Cancer_Facts__Figures_2003.asp. Accessibility verified March 30, 2004.

2 Autier P, Boniol M, Severi G, Dore JF, European Organization for Research and Treatment of Cancer Melanoma Co. Quantity of sunscreen used by European students. *British Journal of Dermatology*. 144:288-291, 2001.

3 Barbosa JG, Castanzo M, DiMarzio CA: Hyperspectral Techniques and Subsurface Imaging. CenSSIS Research and Industrial Collaboration Conference, Poster January 2002, and National Science Foundation Site Visit, May 2002.

4 Born M, Wolf E: Principles of Optics 7th Edition. Cambridge UniversityPress, United Kingdom, 1999.

5 Brancaleon L, Durkin AJ, Tu JH, Menaker G, Fallon JD, Kollias N: *In vivo* fluorescence spectoscopy of nonmelanoma skin cancer. *Photochemistry and Photobiology*. 73(2):178-183, 2001.

6 Canto MI, Setrakian S, Petras RI, Blades E, Chak A, Sivak MV Jr: Methylene blue selectively stains metaplasia in Barrett's esophagus. *Gastrointestinal Endoscopy*. 44(1):1-7, 1996.

7 Centers for Disease Control and Prevention (CDC), The Department of Health and Human Services. Available at http://www.cdc.gov. Accessibility verified December 9, 2004.

8 Cheng PC, Kriete A, "Image contrast in confocal light microscopy", in: Handbook of Biological Confocal Microscopy. Pawley JB (ed), 2nd Edition. Plenum Press, New York, p281-310, 1995.

9 Cogswell CJ, Larkin KG, "The specimen illumination path and its effect on image quality", in: Handbook of Biological Confocal Microscopy. Pawley JB (ed), 2nd Edition. Plenum Press, New York, p127-137, 1995.

10 Corle TR, Chou CH, Kino GS: Depth response of confocal optical microscopes. *Optical Letters*. 11:770-772, 1986.

11 Dunn AK, Smithpeter C, Welch AJ, Richard-Kortum R. Finite-Difference Time-Domain simulation of light scattering from single cells. *Journal of Biomedical Optics*. 2(3):262-266, July 1997.

12 Dunn AK, Smithpeter C, Welch AJ, Richards-Kortum R: Sources of contrast in confocal reflectance imaging. *Applied Optics*. 35(19):3441-3446, July 1996.

13 Dwyer PJ: Hyperspectral imaging for blood oxygen saturation measurement in human skin. Northeastern University. 1997

14 Fedorak IJ, Ko TC, Gordon D, Flisak M, Prinz RA: Localization of islet cell tumors of the Pancreas: A Review of Current Techniques. *Surgery*. 113(3):242-249, March 1993.

15 Fowles GR: Introductins to Modern Optics 2nd Edition. Dover Publications Inc., New York, 1989.

16 Gasparro FP, Mitchnick M, Nash F: A review of sunscreen safety and efficacy. *Photochemistry and Photobiology*. 68(3):243-256, 1998

17 Gaston DA, Naugle C, Clark DP: Mohs Micrographic Surgery Refferal Patterns: The University of Missouri Experience. *Dermatologic Surgery*. 25:862-867, 1999

18 Gill WB, Huffman JL, Lyon ES, Bagley DH, Schoenberg HW, Straus FH II: Selective surface staining of bladder tumors by intravesical methylene blue with enhanced endoscopic identification. *Cancer*. 53(12):2724-2727, June 1984.

19 González S, Gonzalez E, White WM, Rajadhyaksha M, Anderson RR: Allergic contact dermatitis: Correlation of *in vivo* confocal imaging to routine histology. *Journal of the American Academy of Dermatology*. 40(5):708-713, May 1999.

20 González S, Rajadhyaksha M, Halpern AC, "*In vivo* reflectance confocal scanning laser microscopy", in: Principles of Dermoscopy. Malvehy J and Puig S (eds). Metado de Menzies. In: Principios de Dermatoscopia (Spanish Edition). 2001.

21 González S, Rajadhyaksha M, Rubinstein G, Anderson RR. Characterization of psoriasis in vivo by reflectance confocal microscopy. *Journal of Medicine (J Medicine Clin Exper Molec).* 30(5&6):337-356, 1999.

22 Goodman JW. Introduction to Fourier Optics 2nd Edition. McGraw-Hill Companies Inc., Singapore, 1996.

23 Humphreys TR, Nemeth A, McCrevey S, Baer SC, Goldberg LH: A pilot study comparing toluidine blue and hematoxylin and eosin staining of basal cell and squamous cell carcinoma during Mohs surgery. *Dermatol Surg*. 22:693-697, 1996.

24 Inoué S, "Foundations of confocal scanned imaging in light microscopy", in: Handbook of Biological Confocal Microscopy. Pawley JB (ed), 2nd Edition. Plenum Press, New York, p1-14, 1995.

25 Kaisary AV, F.R.C.S: Assesment of radiotherapy in invasive bladder carcinoma using *in vivo* methylene blue staining technique. *Urology*. 28(2):100-102, Aug 1986.

26 Koenig F, González S, White MW, Lein M, Rajadhyaksha M: Near-infrared confocal laser scanning microscopy of bladder tissue *in vivo*. *Urology*. 53(4), 1999.

27 Lord Rayleigh: *Phil. Mag*. (5), 8:261, 1879.

28 Malitson IH: Interspecimen Comparison of the Refractive Index of Fused Silica. *Journal of the Optical Society of America*. 55(10)1205-1209. October 1965.

29 Martinez JC, Otley CC: The management of melanoma and nonmelanoma skin cancer: A Review for the primary care physicin. *Clinics: Dermatology*. 76(12):1253-1265, Dec 2001.

30 Minsky M.: Microscopy Apparatus, U.S. Patent 3013467. 19 December 1961, filed 7 November 1957.

31 Niebel HH, Chomet B: *In vivo* staining test for delineation of oral intraepithelial neoplastic change: Preliminary report. *JADA*. 68:801-805, 1965.

32 Pawley JB (ed.) Handbook of Biological Confocal Microscopy, 2nd Edition. Plenum Press, New York, 1995.

33 Pinnell SR: Cutaneous Photodamage, Oxidative stress, and topical antioxidant protection. *Journal of the American Academy of Dermatology*. 48(1):1-19, Jan 2003.

34 Rajadhyaksh M, Menaker G, Gonzalez S. Confocal microscopy of excised human skin using acetic acid and crossed polarization: Rapid detection of non-melanoma skin cancers. In: Lasers in Surgery: Advanced Characterization, Therapeutics, and Systems X. Proceedings of SPIE. Vol. 3907, 2000

35 Rajadhyaksha M, Anderson RR, Webb RH: Video-rate confocal scanning laser microscope for imaging human tissues *In vivo*. *Applied Optics*. 38:2105-2115, April 1999.

36 Rajadhyaksha M, González S, "Real-time *in vivo* confocal fluorescence micrcoscopy", in: Handbook of Biomedical Fluorescence. Mycek MA and Pogue BW (eds), Marcel Dekker Inc., 2003.

37 Rajadhyaksha M, Gonzalez S, Zavislan JM, Anderson RR, Webb RH: *In* vivo confocal scanning laser microscopy of human skin II: Advances in instrumentation and comparison with histology. *The Journal of Investigative Dermatology*. 113(3), Sept 1999.

38 Richard RM: A clinical staining test for *in vivo* delineation of dysplasia and carcinoma *in situ*. *Am J Obstet Gyneol*. 86:703-711, 1963.

39 Richards B, Wolf W: Electomagnetic diffraction in optical systems II. Structure of the image field in an aplanatic system. *Proc. R. Soc.* A 253:358-379, 1959.

40 Smithpeter C, Dunn AK, Drezek R, collier T, Richards-Kortum R: Near real time confocal microscopy of cultured Amelanotic cells: Sources of signal, contrast agents and limits of contrast. *Journal of Biomedical Optics*. 3(4):429-436, Oct 1998.

41 Steinman HK, Gross KG, "Basic Mohs Technique", in Mohs Surgery: Fundamentals and Techniques. Rapini RP (ed). Elsevier Science, p7-14, Aug 1998.

42 Stelzer EHK, "The intermediate optical system of laser-scanning confocal microscopes", in: Handbook of Biological Confocal Microscopy. Pawley JB (ed), 2nd Edition. Plenum Press, New York, p139-153, 1995.

43 Strasswimmer J: Non-Melanoma Skin Cancer. Wellman Research Seminar. Dec 2002.

44 Tsao H: The Dark Side of Light I&II: Non-melanoma Skin Cancer. Wellman Research Seminar. Nov 2002.

45 Webb RH: Confocal optical microscopy. Rep. Prog. Phys. 59:427-471, 1996.

46 Weinstock MA, "Epidemiology of ultraviolet radiation", In: Cutaneous Oncology: Pathopysiology, Diagnosis, and Treatment. Miller SJ, Maloney ME (eds), Blackwell Science, Inc., Malden Mass., p121-128, 1998.

47 Wennberg AM, Gudmundson F, Stenquist BO, Ternesten A, Mölne L, Rosén A, Larkö O: *In Vivo* ddetection of basal cell carcinoma using imaging spectroscopy. *Acat Derm Venereol*. 79:54-61, 1999.

48 White MW, Rajadhyaksha M, González S, Fabian RL, Anderson RR: Noninvasive imaging of human oral mucosa *in vivo* by confocal reflectance microscopy. *The Laryngoscope.* 109: October 1999.

49 Wilson T (ed). Confocal Microscopy. Academic Press, San Diego, 1990

50 Wilson T, "The role of the pinhole in confocal imaging system", in: Handbook of Biological Confocal Microscopy. Pawley JB (ed), 2nd Edition. Plenum Press, New York, p167-182, 1995.

51 Wilson T, Carlini AR: Size of the detector in confocal imaging systems. *Optics Letters*. 12(4):227-229, April 1987.

52 Wilson T, Carlini AR: The effect of aberrations on the axial response of confocal imaging systems. *Journal of Microscopy*. 154(3):243-256, June 1989.

53 Wilson T, Carlini: Three-dimensional imaging in confocal imaging systems with finite sized detectors. *Journal of Microscopy*. 149(1):51-66, January 1988.

54 Yaroslavsky AN, Barbosa J, Neel V, DiMarzio C, Anderson RR. "Combining Multi-Spectral Polarized-Light Imaging and Confocal Microscopy for Localization of Nonmelanoma Skin Cancer," J Biomed Opt, 10(1), 2005.

55 Yaroslavsky AN, Neel V, Anderson RR: Demarcation of nonmelanoma skin cancer margins in thick excisions using multispectral polarized light imaging. *The Journal of Investigative Dermatology*. 121(2)259-266, August 2003

56 Zuluaga AF, Drezek R, Collier T, Lotan R, Follen M, Richards-Kortum R: Contrast agents for confocal microscopy: how simple chemical affect confocal images of normal and cancer cells in suspension. *Journal of Biomedical Optics*. 7(3):398-403, July 2002.

Appendix A Losses and Quarter Wave Plate Analysis

The equation used to calculate the losses through the beam splitter and quarter wave plate (eq 4.1) is expanded below. It is assumed that the light that propagates through the quarter wave plate is totally reflected back, the product is shown below.

$$\begin{bmatrix} 1 & 0 \\ 0 & e^{2i\Delta\phi} \end{bmatrix} = \begin{bmatrix} 1 & 0 \\ 0 & e^{i\Delta\phi} \end{bmatrix} \cdot \begin{bmatrix} 1 & 0 \\ 0 & 1 \end{bmatrix} \cdot \begin{bmatrix} 1 & 0 \\ 0 & e^{i\Delta\phi} \end{bmatrix}, \qquad \text{A.1}$$

where

$$\Delta\phi = \frac{2\pi\ell\Delta n}{\lambda} \qquad \ell\Delta n = \frac{N\lambda_o}{4}. \tag{A.2}$$

N depends on the order of the quarter wave plate. N equal to 1 is zero order and the higher orders are N = 3 and N = 5. The calculations for power received were made for p-polarized beam propagation through the beam splitter, quarter wave plate at a 45º degree angle, returning through the quarter wave plate, and reflecting off the beam splitter.

$$F = \begin{bmatrix}1 & 0\end{bmatrix}\cdot\begin{bmatrix}\tau_p^* & 0\\ 0 & \tau_p^*\end{bmatrix}\cdot\begin{bmatrix}c & -s\\ s & c\end{bmatrix}\cdot\begin{bmatrix}1 & 0\\ 0 & e^{-2i\Delta\phi}\end{bmatrix}\cdot\begin{bmatrix}c & s\\ -s & c\end{bmatrix}\cdot\begin{bmatrix}\rho_p^* & 0\\ 0 & \rho_p^*\end{bmatrix}\cdot \tag{A.3}$$
$$\begin{bmatrix}\rho_p & 0\\ 0 & \rho_p\end{bmatrix}\cdot\begin{bmatrix}c & -s\\ s & c\end{bmatrix}\cdot\begin{bmatrix}1 & 0\\ 0 & e^{2i\Delta\phi}\end{bmatrix}\cdot\begin{bmatrix}c & s\\ -s & c\end{bmatrix}\cdot\begin{bmatrix}\tau_p & 0\\ 0 & \tau_p\end{bmatrix}\cdot\begin{bmatrix}1\\ 0\end{bmatrix}$$

The top half of equation A.3 is the conjugate equation and the total percentage of power received by the detector is F. By leaving out the [1 0] the percentage of power in s and p polarization is calculated.

With the new beam splitter the calculated fraction of power at the detector is 72% for 630nm light and 79% for 660 nm light. Figure A-1 shows the percentage of power received by the detector as a function of quarter wave plate angle. Power received will be less if the quarter wave plate is misaligned and the fast axis is not at 45 degrees.

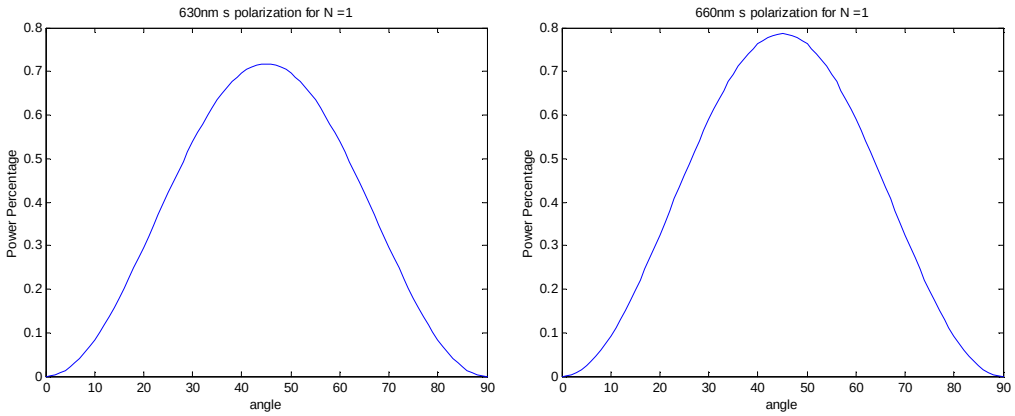

Figure A-1. Percentage of power received by the detector versus the quarter wave plate angle, 630nm left and 660nm right.

To determine the order of the quarter wave plate a 632.8nm HeNe and 533nm YAG laser was used. The configuration of Figure A-2 was used to measure the percentage of returned p and s polarized light. The second polarizer was rotated to allow either p or s polarized light through. The percentage of light that was returned using the configuration of Figure A-2 was also calculated for N = 1, 3, and 5. The calculated results are shown in Table A-1.

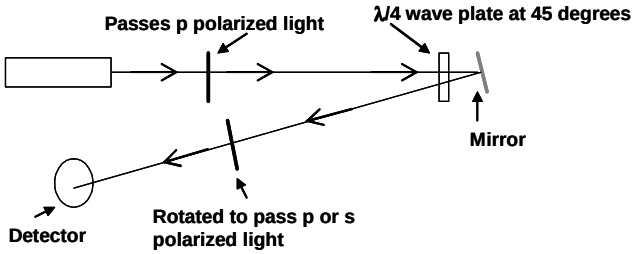

Figure A-2. Setup used to measure order of quarter wave plate

The measured s and p polarized light using the YAG and HeNe laser agreed best with the zero order calculated returned power.

	N		
HeNe	1	3	5
p	22%	98%	41%
s	77%	1.04%	59%
YAG			
p	58%	24%	89%
s	41%	75%	10%

Table A-1. Calculated returned percentage of power

Appendix B PMT Dark Noise

With high gains of about 10^6 the PMT produces noticeable anode dark current. This dark current noise gets integrated by the amplifier and shows as bright spots on the images. The dark noise current from the photomultiplier tube and socket shows up as pulses on an oscilloscope. The pulses are 3 to 5 nanoseconds and are in the millivolt range with 50 ohms of termination.

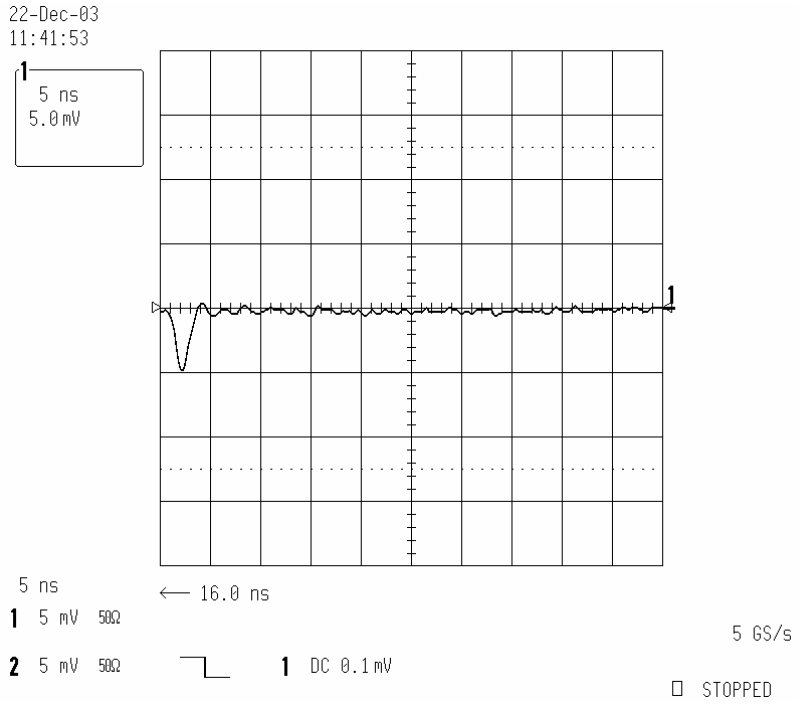

Figure B-3. Dark noise from PMT

Appendix C Matlab Scripts

```
**********************************************************
% Reads images in to calculate axial resolution

function [x,y,fwhm] = axial_res(filename,numfiles);

% Display images 1, 5, and 10 to choose area to
% perform calculations
filenamet = strcat(filename,num2str(1));
data = imread(filenamet,'bmp');
figure;imagesc(data),colormap('gray')

filenamet = strcat(filename,num2str(5));
data = imread(filenamet,'bmp');
figure;imagesc(data),colormap('gray')

filenamet = strcat(filename,num2str(10));
data = imread(filenamet,'bmp');
figure;imagesc(data),colormap('gray')

rows = input('Enter rows: ');
cols = input('Enter cols: ');

numpixels = length(rows)*length(cols);
% read in the points or average of points
for i = 1:numfiles
   filenamet = strcat(filename,num2str(i));
   data = imread(filenamet,'bmp');
   points(i) = sum(sum(data(rows,cols)))/numpixels;
end

normpoints = points/max(points);
y = normpoints;
x = 1:length(normpoints);
fwhm = zeros(size(x));
fwhm(:) = 1/2;
figure;plot(x,y,x,fwhm,x,y,'o'),grid
```

```
%*****************************************************
% calculate laterial resolution
% Measured 8 pixels = 10um, so about 1.2um/pixel

function [x,lsf,esqr]=later_res(filename,sign)

data = imread(filename,'bmp');
figure;imagesc(data),axis image,colormap('gray')
row = input('Enter row: ');
col = input('Enter col: ');
esf = double(data(row,col));
esf = esf/size(esf,1);
lsf = diff(esf);

x = 1:length(lsf);
esqr = zeros(size(x));
esqr(:) = (1/exp(2));
lsf = sign*(lsf/max(sign*lsf));
y = lsf;
figure;plot(x,lsf,x,esqr);
```

```
%*****************************************************************
% Creat map without desampling
% crops 42 pixels for top and bottom of image
% also crops for left and right of images not on edges

function imd = mosaic();
clc
mapgrid = [133:1:144;132:-1:121;109:1:120;108:-1:97;85:1:96;84:-1:73; ...
61:1:72;60:-1:49;37:1:48;36:-1:25;13:1:24;12:-1:1];

mapgridn = reshape(mapgrid',1,prod(size(mapgrid)));
[x,y]=size(mapgrid);
rp = 42;
cp = 59;
rowend = 480-rp-rp; % 396 for rp = 42
colend = 640-cp-cp; %stopped here JGB
rows = [1+rp:480-rp];

k = 1;
for i=1:x
   cols = [1+cp:640-cp];
   for j=1:y
      if (  exist(strcat('map',num2str(mapgridn(k)),'.bmp'),'file') == 0  )
         data = uint8(zeros(480,640));
         fprintf('map%d.bmp is missing \n',mapgridn(k));
      else
         data = imread(strcat('map',num2str(mapgridn(k))),'bmp');
      end

      if (i == 1)
         imd(1:480-rp,cols) = data(1:480-rp,1+cp:640-cp);
      elseif (i == x)
         imd(rows(1):rows(length(rows))+rp,cols) = data(1+rp:480,1+cp:640-cp);
      else
         imd(rows,cols) = data(1+rp:480-rp,1+cp:640-cp);
      end
      cols = cols + colend;
      k = k+1;
   end
   rows = rows + rowend;
end

cd ..
fprintf('Saving Mosaic');
imwrite(imd,'mosaic.bmp','bmp');
```

```
%*********************************************************************
% Places a scale bar on imported image and saves the image with the
% same name but adds an sc at the end of the filename
% before the extension. For mosaic or single images

% pixel length of 333 is 400um
% pixel length of 83 is 100um
function scale_bar(filename,pixel_length,type)

data = imread(filename,'bmp');

if (type == 'mosaic')  % for mosaic image
   data(4400:4475,5500:5500+pixel_length)=255;
else                   % for single image
   data(415:425,520:520+pixel_length)=255;
end

imagesc(data), axis image,colormap('gray')
imwrite(data,strcat(filename,'sc.bmp'),'bmp');
```

```
%*********************************************************************
% Calculates the precentage of power received at the detector
% going through the VivaScope polarize beam splitter (for 830nm)
% and quarter wave plate (for 830nm) using the HeNe laser.
clear,clc
% change T and R to 1 and 0 for new beam splitter
Tp      = 0.95;%0.40; % With 630nm measured 40% transmission for p
Ts      = 0;%0.008;  % With 630nm measured 0.8 % transmission for s
Rp      = 0;%0.50;   % With 630nm measured 50% reflection for p
Rs      = 0.98;%0.90;   % With 630nm measured 90% reflection for s
theta   = pi/4;
c       = cos(theta);
s       = sin(theta);
N       = 1;           % for zero order waveplate
lambda_diode    = 830;  % in nanometers
lambda_HeNe     = 630;%660;
delta_phi       = (2*pi/4)*(N*lambda_diode/lambda_HeNe);

E = [1 0]';
Trans = [sqrt(Tp) 0;0 sqrt(Ts)];
Rforward = [c s;-s c];
quarter_wave_sq = [1 0; 0 exp(2i*delta_phi)];
Rreverse = [c -s;s c];
Refl = [sqrt(Rp) 0; 0 sqrt(Rs)];

Ftemp = Refl*Rreverse*quarter_wave_sq*Rforward*Trans*E;
F = [abs(Ftemp(1))^2;abs(Ftemp(2))^2 ]

% shows maximum s reflection vs theta
angle_range = [0:90];
for angle = 0:90
   theta2   = angle*pi/180;
   c       = cos(theta2);
   s       = sin(theta2);
   Rforward = [c s;-s c];
   Rreverse = [c -s;s c];
   Ftemp = Refl*Rreverse*quarter_wave_sq*Rforward*Trans*E;
   F = [abs(Ftemp(1))^2;abs(Ftemp(2))^2 ];
   Fs(angle+1) = F(2);
   Fp(angle+1) = F(1);
end

figure;plot([0:90], Fs),xlabel('angle'),ylabel('Power Percentage'), ...
  title(strcat('s polarization for N = ',num2str(N)))
figure;plot([0:90], Fp),xlabel('angle'),ylabel('Power Percentage'), ...
  title(strcat('p polarization for N = ',num2str(N)))
```

```
%*****************************************************************
% Estimates the order of the 830nm quarter wave plate
% Using 632.8nm light and YAG 533nm YAG light
% N = 1 zero order, and higher order N = 3, and N = 5;

N       = 1; %3; 5; % change to 1, 3, and 5
theta   = pi/4;
c       = cos(theta);
s       = sin(theta);
lambda_diode    = 830;  % in nanometers
lambda_HeNe     = 632.8;
lambda_YAG      = 533;
E = [1 0]';             % p polarization
Rforward = [c s;-s c];
Rreverse = [c -s;s c];
delta_phi       = (2*pi/4)*(N*lambda_diode/lambda_HeNe);
%delta_phi       = (2*pi/4)*(N*lambda_diode/lambda_YAG);
quarter_wave = [1 0; 0 exp(2i*delta_phi)];
Ftemp = Rreverse*quarter_wave*Rforward*E;
F = [abs(Ftemp(1))^2;abs(Ftemp(2))^2 ]
```

```
%*********************************************************************
% Creates the Airy point spread function, for paraxial conditions
% (small NA)

function [Airy_psf,Airy_psf_conf] = airy_psf(NA,lambda,INDEX)
clc
lambda = lambda/1000; %in microns
alpha = asin(NA/INDEX);
incr = 0.01;
r = [-4:incr:4];     %in microns
k = 2*pi*INDEX/lambda;
p = r*k*sin(alpha);
% The 1st dark fringe is at 1.22*pi = 2*pi*r*NA/lambda
firstzero = 0.61*lambda/NA;
conf_res = 0.46*lambda/NA;
fprintf('\nZero crossing at r = %f\n',firstzero)
fprintf('Confocol res at r = %f\n\n',conf_res)

% create the 3-D Ariy pattern
x=[0:length(r)-1];
center = floor(length(x)/2);
[X,Y]=meshgrid(x,x);
rp = sqrt( (X-center).^2 + (Y-center).^2 );
rp = rp*incr;
vp = rp*k*(NA/INDEX);
Airy_psf = (2*besselj(1,vp)./vp).^2;
p = isnan(Airy_psf);
index = find(p == 1);
Airy_psf(index) = 1;
L = length(rp);
X = [-( (L+1)/2 -1 ):(L-1)/2]*incr;
Y = X;
Airy_psf_conf = Airy_psf.^2;

figure;
plot(X,Airy_psf((length(rp)-1)/2,:),...
   X,Airy_psf_conf((length(rp)-1)/2,:)),xlabel('radius (um)'),...
   title('Lateral/Transverse plane psf'),grid
legend('psf','confocal psf')

figure;
imagesc(X,Y,Airy_psf),title('psf'),xlabel('X (um)'),...
   ylabel('Y (um)');
figure;
imagesc(X,Y,Airy_psf_conf),title('confocal psf'),xlabel('X (um)'),...
   ylabel('Y (um)');
```

```
%*********************************************************************
% Creates the sinc squared axial point spread function,
% for paraxial conditions (small NA)

function [sinc_psf,sinc_psf_conf] = sinc_psf(NA,lambda,INDEX)
clc

lambda = lambda/1000; %in microns
alpha = asin(NA/INDEX);
incr = 0.01;
z = [-6:incr:6];
k = 2*pi*INDEX/lambda;
zeta = z*k*((NA/INDEX)^2);

% The 1st dark fringe is at +-4pi = z*2*pi*(NA^2)/(INDEX*lambda)
firstzero = 2*INDEX*lambda/(NA^2);
conf_res = 1.4*INDEX*lambda/(NA^2);
fprintf('\nZero crossing at z = %0.4f um\n',firstzero);
fprintf('Confocal res at z = %0.4f um\n\n',conf_res);

sinc_psf = (sin(zeta/4)./(zeta/4)).^2;
sinc_psf_conf=sinc_psf.^2;
plot(z,sinc_psf,z,sinc_psf_conf),xlabel('z (um)'),...
   title('Axial psf'),grid
legend('psf','confocal psf')
```

```
%*************************************************************************
**
% Shows the 26.5% dip in the Airy pattern for conventional and confocal

clear,clc
NA = .4;
lambda = 830/1000; %in microns
INDEX = 0.5;

alpha = asin(NA/INDEX);
incr = 0.01;
r = [-3:incr:3];     %in microns
k = 2*pi*INDEX/lambda;
p = r*k*sin(alpha);

firstzero = 0.61*lambda/NA;
conf_res = 0.46*lambda/NA;
fprintf('\nZero crossing at r = %f\n',firstzero)
fprintf('Confocol res at r = %f\n\n',conf_res)

lat_psf = (2*real(besselj(1,p))./p).^2;
NaNpoint = isnan(lat_psf);
index=find(NaNpoint == 1);
lat_psf(index)=1;

%shift next Airy pattern by 1.22pi
pp = p - 1.22*pi;
lat_psf2 = (2*real(besselj(1,pp))./pp).^2;
NaNpoint = isnan(lat_psf2);
index=find(NaNpoint == 1);
lat_psf2(index)=1;

figure;
plot(lat_psf),hold on,plot(lat_psf2,'g'),...
   plot(lat_psf+lat_psf2,'r'),hold off
   title('Conventional Airy')

% Confocal transverse psf
lat_psf_conf = lat_psf.^2;
pp = p - 2.77;
lat_psf2 = (2*real(besselj(1,pp))./pp).^2;
NaNpoint = isnan(lat_psf2);
index=find(NaNpoint == 1);
lat_psf2(index)=1;
lat_psf_conf2 = lat_psf2.^2;
figure;
```

```
plot(lat_psf_conf),hold on,plot(lat_psf_conf2,'g'),...
   plot(lat_psf_conf+lat_psf_conf2,'r'),hold off
   title('Confocal Airy')

 % Sinc squared psf
z = [-10:incr:10];
k = 2*pi*INDEX/lambda;
zeta = z*k*((NA/INDEX)^2); %=z*k*(sin(alpha))^2

% The 1st dark fringe is at +-4pi = z*2*pi*(NA^2)/(INDEX*lambda)
firstzero = 2*INDEX*lambda/(NA^2);
conf_res = 1.4*INDEX*lambda/(NA^2);
fprintf('\nZero crossing at z = %0.4f um\n',firstzero);
fprintf('Confocal res at z = %0.4f um\n',conf_res);

% Axial psf
axial_psf = (sin(zeta/4)./(zeta/4)).^2;
% Shift second psf by 4pi
zeta2 = zeta - 4*pi;
axial_psf2 = (sin(zeta2/4)./(zeta2/4)).^2;
figure;
plot(axial_psf),hold on, plot(axial_psf2,'g'),...
   plot(axial_psf+axial_psf2),hold off,grid
   title('Conventional sinc')
axial_psf_conf=axial_psf.^2;
% Shift confocal psf
zeta2 = zeta - 9.1;
axial_psf2 = (sin(zeta2/4)./(zeta2/4)).^2;
axial_psf_conf2=axial_psf2.^2;
figure;
plot(axial_psf_conf),hold on, plot(axial_psf_conf2,'g'),...
   plot(axial_psf_conf+axial_psf_conf2),hold off,grid
   title('Confocal sinc')
```

```
%*********************************************************
% Calculates the psf at given coordinates of r and z
% from Rob Webb, and Born and Richard's paper

function psf = jose_psf(r,z,NA,LAMBDA,INDEX)

lambda = LAMBDA/1000;
theta = asin(NA/INDEX);
dalpha = theta/100;
alpha = [0:dalpha:theta];

kp = 2*pi*INDEX/lambda;
salpha = sin(alpha);
calpha = cos(alpha);
cqalpha = sqrt(calpha);
rp = r*kp*salpha;
zp = z*kp*calpha;

A = besselj(0,rp).*cqalpha.*salpha.*(1+calpha)...
   .*exp(i*z.*kp.*calpha);
B = besselj(1,rp).*cqalpha.*salpha.*salpha...
   .*exp(i*z.*kp.*calpha);
C = besselj(2,rp).*cqalpha.*salpha.*(1-calpha)...
   .*exp(i*z.*kp.*calpha);

Io = trapz(alpha,A);
I1 = trapz(alpha,B);
I2 = trapz(alpha,C);

psf= abs(Io)^2 + 2*abs(I1)^2 + abs(I2)^2; % psf(r,z)
```

```
%*****************************************************************
% Calculates the psf at given coordinates of r and z
% and returns the psf in normalized optical coordinates
% v, u from Rob Webb, and Born and Richard's paper
function psf = jose_psf_uv(r,z,NA,LAMBDA,INDEX)
clc

lambda = LAMBDA/1000;
alpha = asin(NA/INDEX);
dtheta = alpha/100;
theta = [0:dtheta:alpha];
k = 2*pi*INDEX/lambda;
v = r*k*sin(alpha);
u = z*k*(sin(alpha))^2;
s = sin(theta);
c = cos(theta);
c_sq_r = sqrt(c);
s_sq = sin(theta).^2;
J0 = besselj(0,v*s/sin(alpha));
J1 = besselj(1,v*s/sin(alpha));
J2 = besselj(2,v*s/sin(alpha));
expon = exp(i*u*c./(sin(alpha))^2);

A = c_sq_r.*s.*(1+c).*J0.*expon;
B = c_sq_r.*s_sq.*J1.*expon;
C = c_sq_r.*s.*(1-c).*J2.*expon;

Io = trapz(theta,A);
I1 = trapz(theta,B);
I2 = trapz(theta,C);

%psf = (abs(Io)^2 + 4*abs(I1)^2*(cos(phi))^2 + abs(I2)^2 ...
%       + 2*cos(2*phi)*real(Io*conj(I2)));

psf = abs(Io)^2 + 2*abs(I1)^2 + abs(I2)^2;
```

```
%*************************************************
% Generates the 3D lateral and axial psf
% in meters (r,z)

NA = 0.75;
LAMBDA = 830;
INDEX = 1.33;
lambda = LAMBDA/1000; % in microns
incr = 0.1;
radius = 10; % radius of geometric shadow evaluated
z_dist = 10; % distance of geometric shadow evaluated
r = [-radius:incr:radius];
z = [-z_dist:incr:z_dist];

resel_r = 0.61*lambda/NA;
fprintf('\nlateral resel = %0.4f um\n',resel_r);
resel_z = 2*INDEX*lambda/(NA^2);
fprintf('\naxial resel = %0.4f um\n\n',resel_z);

Z = zeros(length(r),length(z)); % r rows (y), z cols (x)
h  = waitbar(0,'For loops take forever','resize','on');
for  row = 1:length(r) % x/row loop
          for col = 1:length(z) % y/col loop

     Z(row,col) = jose_psf(r(row), z(col),NA,LAMBDA,INDEX);
     %keyboard
   end
   waitbar(row/length(r),h);
end
close(h);
norm = max(max(Z));
Z = Z/norm;
rc = (length(r)+1)/2;
zc = (length(z)+1)/2;
Ideal_do = (20*2.5*lambda)/(NA*pi);
%jose_confshow;
```

```
%*********************************************************************
% Generates the 3D lateral and axial psf
% in optical coordinates (v,u)

NA = 0.75;
LAMBDA = 830;
INDEX = 1.33;
lambda = LAMBDA/1000; % in microns
incr = 0.1;
radius = 10; % radius of geometric shadow evaluated
z_dist = 10; % distance of geometric shadow evaluated
r = [-radius:incr:radius];
z = [-z_dist:incr:z_dist];

resel_r = 0.61*lambda/NA;
fprintf('\nlateral resel = %0.4f um\n',resel_r);
resel_z = 2*INDEX*lambda/(NA^2);
fprintf('\naxial resel = %0.4f um\n\n',resel_z);

alpha = asin(NA/INDEX);
k = 2*pi*INDEX/lambda;
v = r*k*sin(alpha);
u = z*k*(sin(alpha))^2;

Z = zeros(length(r),length(z)); % r rows (y), z cols (x)
h  = waitbar(0,'For loops take forever','resize','on');
for  row = 1:length(r) % x/row loop
          for col = 1:length(z) % y/col loop

     Z(row,col) = jose_psf_vu(r(row), z(col),NA,LAMBDA,INDEX);
     %keyboard
   end
   waitbar(row/length(r),h);
end
close(h);
norm = max(max(Z));
Zvu = Z/norm;
vc = (length(v)+1)/2;
uc = (length(u)+1)/2;
```

```
%*************************************************************
% Generates the 2D lateral and axial psf curves
% in meters (r,z)

NA = 0.75;
LAMBDA = 660;
INDEX = 1.33;
lambda = LAMBDA/1000; % in microns
incr = 0.001;
radius = 10; % radius of geometric shadow evaluated
z_dist = 10; % distance of geometric shadow evaluated
r = [-radius:incr:radius];
z = [-z_dist:incr:z_dist];

resel_r = 0.61*lambda/NA;
fprintf('\nlateral zero crossing = %0.4f um\n',resel_r);
resel_z = 2*INDEX*lambda/(NA^2);
fprintf('\naxial zero crossing = %0.4f um\n\n',resel_z);

h  = waitbar(0,'For lateral curve','resize','on');
for  i = 1:length(r) % x/row loop
    Zr(i) = jose_psf(r(i), 0, NA, LAMBDA, INDEX);
    waitbar(i/length(r),h);
end
close(h);
Zr = Zr/max(Zr);
k = 2*pi*INDEX/lambda;
v = r*k*NA/INDEX;
figure;
plot(r,Zr),xlabel('r ({\mu}m)')

h  = waitbar(0,'For axial curve','resize','on');
for  i = 1:length(z) % x/row loop
    Zz(i) = jose_psf(0, z(i), NA, LAMBDA, INDEX);
    waitbar(i/length(z),h);
end
close(h);
Zz = Zz/max(Zz);
k = 2*pi*INDEX/lambda;
u = z*k*((NA/INDEX)^2);
figure;
plot(z,Zz),xlabel('z ({\mu}m)')
```

```
%*********************************************************
% Generates the lateral and axial psf curves
% in optical coordinates (v,u)

NA = 0.75;
LAMBDA = 830;
INDEX = 1.33;
lambda = LAMBDA/1000; % in microns
incr = 0.001;
radius = 10; % radius of geometric shadow evaluated
z_dist = 10; % distance of geometric shadow evaluated
r = [-radius:incr:radius];
z = [-z_dist:incr:z_dist];

resel_r = 0.61*lambda/NA;
fprintf('\nlateral zero crossing = %0.4f um\n',resel_r);
resel_z = 2*INDEX*lambda/(NA^2);
fprintf('\naxial zero crossing = %0.4f um\n\n',resel_z);

h  = waitbar(0,'For lateral curve','resize','on');
for  i = 1:length(r) % x/row loop
    Zv(i) = jose_psf_vu(r(i), 0, NA, LAMBDA, INDEX);
    waitbar(i/length(r),h);
end
close(h);
Zv = Zv/max(Zv);
k = 2*pi*INDEX/lambda;
v = r*k*NA/INDEX;
figure;
plot(v,Zv),xlabel('v (o.u)')

h  = waitbar(0,'For axial curve','resize','on');
for  i = 1:length(z) % x/row loop
    Zu(i) = jose_psf_vu(0, z(i), NA, LAMBDA, INDEX);
    waitbar(i/length(z),h);
end
close(h);
Zu = Zu/max(Zu);
k = 2*pi*INDEX/lambda;
u = z*k*((NA/INDEX)^2);
figure;
plot(u,Zu),xlabel('u (o.u)')
```

```
%*************************************************************************
% Tests the implementation of the 3-D psf to compare to Table 1 of
% Richards and Wolf 1959.  For the energy density in the electric
% field. Alpha and the row for v_n have to updated each time.
clear,clc
alpha =90*pi/180; % alpha = 0.01 radians, 30,60,75,90 degrees
v_n = [.93,1.40,1.83,2.36,3.83,7.02;
       .98,1.47,1.94,2.50,4.15,7.03;
      1.16,1.73,2.27,2.93,4.75,8.1;
      1.33,1.95,2.50,3.14,4.75,8.1;
      1.48,2.10,2.63,3.23,4.70,8.0];
u=0;
phi=0;

for i=1:6
   v = v_n(5,i) %(row,col)
   dtheta = alpha/100;
   theta = [0:dtheta:alpha];
   s = sin(theta);
   c = cos(theta);
   c_sq_r = sqrt(c);
   s_sq = sin(theta).^2;
   J0 = besselj(0,v*s/sin(alpha));
   J1 = besselj(1,v*s/sin(alpha));
   J2 = besselj(2,v*s/sin(alpha));
   expon = exp(i*u*c./(sin(alpha))^2);

   A = c_sq_r.*s.*(1+c).*J0.*expon;
   B = c_sq_r.*s_sq.*J1.*expon;
   C = c_sq_r.*s.*(1-c).*J2.*expon;

   Io = trapz(theta,A);
   I1 = trapz(theta,B);
   I2 = trapz(theta,C);

   we = (abs(Io)^2 + 4*abs(I1)^2*(cos(phi))^2 + abs(I2)^2 ...
      + 2*cos(2*phi)*real(Io*conj(I2)));
   % normalize to 100
   %we = 100*we/(9.9993e-009) % value at u=0,v=0 for alpha = 0.01
   %we = 100*we/0.0626 % value at u=0, v=0 for alpha = 30 degrees
   %we = 100*we/0.5779 % value at u=0, v=0 for alpha = 60 degrees
   %we = 100*we/0.9316 % value at u=0, v=0 for alpha = 75 degrees
   we = 100*we/1.1368 % value at u=0, v=0 for alpha = 90 degrees
end
```

```
%*************************************************************************
% Displays the 3D psf

rc = (length(r)+1)/2;
zc = (length(z)+1)/2;
figure
        plot(r,Z(:,zc)),grid
        title('lateral profile')
        xlabel('lateral, units are microns');

figure
        plot(z,Z(rc,:)),grid
        title('axial profile')
        xlabel('axial, units are microns');

figure
        contour(z,r,Z,32); axis image % option 'k' black and white
        xlabel('axial, units are microns');
        ylabel('lateral, units are microns');

figure
        imagesc(z,r,Z,[0 1]); axis image
        xlabel('axial, units are microns');
        ylabel('lateral, units are microns');
```

```
%*****************************************************************
% loads and plots saved non-paraxial lateral and axial curves

clear,clc
load 830psfrz_curves.mat
figure; plot(z,Zz.^2),title('Axial 830'), grid
figure; plot(r,Zr.^2),title('Lateral 830'), grid

clear,clc
load 660psfrz_curves.mat
figure; plot(z,Zz.^2),title('Axial 660'), grid
figure; plot(r,Zr.^2),title('Lateral 660'), grid

clear,clc
load 650psfrz_curves.mat
figure; plot(z,Zz.^2),title('Axial 650'), grid
figure; plot(r,Zr.^2),title('Lateral 650'), grid

clear,clc
load 630psfrz_curves.mat
figure; plot(z,Zz.^2),title('Axial 630'), grid
figure; plot(r,Zr.^2),title('Lateral 630'), grid
```

```
%*************************************************************
% Compares the paraxial and nonparaxial lateral and axial
% response

%load 830_psf_6x4_n1 % for NA of 0.75
load 830_psf_6X4_1-2NA_n1 %for NA of 1.2

[Airy_psf,Airy_psf_conf] = airy_psf(NA,LAMBDA,INDEX);
figure
plot(r,Airy_psf(rc,:),r,Z(:,zc),'--r');
xlabel('radius r ({\mu}m)');
title('Lateral Response'),grid
legend('PSF(r)','PSF(r,0)');

[sinc_psf,sinc_psf_conf] = sinc_psf(NA,LAMBDA,INDEX);
figure
plot(z,sinc_psf,z,Z(rc,:),'--r');
xlabel('axial z ({\mu}m)');
title('Axial Response'),grid
legend('PSF(z)','PSF(0,z)')
```

```
%*************************************************************
% Calculates the FWHM vs pinhole size, non-paraxial
% in r and z (meters)
clear,clc
load 830psfrz_curves % 830nm, NA = 0.75, n = 1.33
%load 630psfrz_curves % 630nm, NA = 0.75, n = 1.33
%load 650psfrz_curves % 650nm, NA = 0.75, n = 1.33
%load 660psfrz_curves % 660nm, NA = 0.75, n = 1.33


rp = [0.01:0.1:2]; %radius
h  = waitbar(0,'For lateral convolution','resize','on');
for i=1:length(rp)
   index1 = find(r <= rp(i) & r >= -rp(i));
   aper = zeros(1,length(r));
   aper(index1(1):index1(length(index1)))=1;
   con = conv(Zr,aper);
   lat_psf_pinhole = Zr.*con(10001:30001);
   n_psf = lat_psf_pinhole/max(lat_psf_pinhole);
   index2=find(n_psf >= 0.5);
   rhalf(i) = r(index2(length(index2)));
   waitbar(i/length(rp),h);
end
close(h);
figure;plot(rp*2*32,rhalf*2),xlabel('Pinhole Diameter ( {\mu}m )'),...
   ylabel('FWHM ( {\mu}m )')

rpp = [0.01:0.2:9];
Zz_sq = Zz.^2;
h  = waitbar(0,'For axial convolution','resize','on');
for i=1:length(rpp)
   index1 = find(r <= rpp(i) & r >= -rpp(i));
   aper = zeros(1,length(r));
   aper(index1(1):index1(length(index1)))=1;
   con = conv(Zz_sq,aper);
   ax_psf_pinhole = con(10001:30001);
   n_psf_ax = ax_psf_pinhole/max(ax_psf_pinhole);
   index2=find(n_psf_ax >= 0.5);
   zhalf(i) = z( index2(length(index2)));
   waitbar(i/length(rpp),h);
end
close(h);
figure;plot(rpp*2*32,zhalf*2),xlabel('Pinhole Diameter ( {\mu}m )'),...
   ylabel('FWHM ( {\mu}m )')
```

```
%*************************************************************
% Calculate the FWHM verses pinhole size, non-paraxial
% in v and u optical units
clear,clc
load 830psfvu_curves % 830nm, NA = 0.75, n=1.33, in o.u.


vp = [0.01:0.5:10.5]; %radius
h  = waitbar(0,'For lateral convolution','resize','on');
for i=1:length(vp)
   index1 = find(v <= vp(i) & v >= -vp(i));
   aper = zeros(1,length(v));
   aper(index1(1):index1(length(index1)))=1;
   con = conv(Zv,aper);
   lat_psf_pinhole = Zv.*con(10001:30001);
   n_psf = lat_psf_pinhole/max(lat_psf_pinhole);
   index2=find(n_psf >= 0.5);
   vhalf(i) = v(index2(length(index2)));
   waitbar(i/length(vp),h);
end
close(h);
figure;plot(vp,vhalf),xlabel('vp'),ylabel('v_{1/2}')


vpp = [0.01:1:50];
Zp = Zu.^2;
h  = waitbar(0,'For axial convolution','resize','on');
for i=1:length(vpp)
   index1 = find(v <= vpp(i) & v >= -vpp(i));
   aper = zeros(1,length(v));
   aper(index1(1):index1(length(index1)))=1;
   con = conv(Zp,aper);
   ax_psf_pinhole = con(10001:30001);
   n_psf_ax = ax_psf_pinhole/max(ax_psf_pinhole);
   index2=find(n_psf_ax >= 0.5);
   uhalf(i) = u( index2(length(index2)));
   waitbar(i/length(vpp),h);
end
close(h);
figure;plot(vpp,uhalf),xlabel('vp'),ylabel('u_{1/2}')
```

```
%*************************************************************
% Dispersion curve for thin len with BK7 and synthetic
% fused silica
clear,clc

f830 = 10; %mm
n830_fs = 1.45281564625;
n830_bk7 = 1.51020190012417;

lambda = [.2:.01:2]; % um
B1bk = 1.03961212;
B2bk = 2.31792344*10^-1;
B3bk = 1.01046945;
C1bk = 6.00069867*10^-3;
C2bk = 2.00179144*10^-2;
C3bk = 1.03560653*10^2;

B1fs = 0.6961663;
B2fs = 0.4079426;
B3fs = 0.8974794;
C1fs = 0.0684043;
C2fs = 0.1162414;
C3fs = 9.896161;

nfs =  sqrt((B1fs*lambda.^2)./(lambda.^2 - C1fs^2) + ...
          (B2fs*lambda.^2)./(lambda.^2 - C2fs^2) + ...
          (B3fs*lambda.^2)./(lambda.^2 - C3fs^2) + 1);
nbk7 = sqrt((B1bk*lambda.^2)./(lambda.^2 - C1bk) + ...
          (B2bk*lambda.^2)./(lambda.^2 - C2bk) + ...
          (B3bk*lambda.^2)./(lambda.^2 - C3bk) + 1);

f_fs = f830*(n830_fs - 1)./(nfs - 1);
f_bk = f830*(n830_bk7 - 1)./(real(nbk7) - 1);

figure;
plot(lambda,f_fs,lambda,f_bk),ylabel('focal length mm'), ...
   xlabel('{\lambda} {\mu}m'),legend('fused silica', 'BK7')

%table_fs = [(lambda*10^3)' nfs'];
%table_bk = [(lambda*10^3)' nbk7'];

index630 = find(lambda == .630);
index650 = find(lambda == .650);
index660 = find(lambda == .660);

diff630fs = f830 - f_fs(index630)
```

diff650fs = f830 - f_fs(index650)
diff660fs = f830 - f_fs(index660)
diff630bk = f830 - f_bk(index630)
diff650bk = f830 - f_bk(index650)
diff660bk = f830 - f_bk(index660)

Appendix D J Biomed Opt Paper Manuscript

Combining Multi-Spectral Polarized-Light Imaging and Confocal Microscopy for Localization of Nonmelanoma Skin Cancer

Anna N. Yaroslavsky[1*], Jose Barbosa[1,2], Victor Neel[1], Charles DiMarzio[2], R. Rox Anderson[1]

[1]Wellman Laboratories of Photomedicine, Massachusetts General Hospital, Harvard Medical School, Boston, MA

[2] Department of Electrical and Computer engineering, Northeastern University, Boston, MA

Corresponding Author:

Anna N. Yaroslavsky, PhD

Wellman Laboratories of Photomedicine,

Department of Dermatology,

55 Fruit Street,

02114, Boston, MA USA

Tel: (617) 726 – 1590,

Fax: (617) 724 – 2075

e-mail: yaroslav@helix.mgh.harvard.edu

Abstract

Multi-spectral polarized light imaging (MSPLI) enables rapid inspection of a superficial tissue layer over large surfaces, but does not provide information on cellular microstructure. Confocal microscopy (CM) allows imaging within turbid media with resolution comparable to that of histology, but suffers from a small field of view. In practice, pathologists use microscopes at low power and high power, to view tumor margins and cell features, respectively. Therefore we studied the combination of CM and MSPLI for demarcation of nonmelanoma skin cancers. Freshly excised thick skin samples with nonmelanoma cancers were rapidly stained with either toluidine or methylene blue dyes, rinsed in acetic acid, and imaged using MSPLI and CM. MSPLI was performed at 630 nm, 660 nm, and 750 nm. The same specimens were imaged by reflectance CM at 630 nm, 660 nm, and 830nm. Results indicate that CM and MSPLI images are in good correlation with histopathology. Cytological features were identified by CM, and tumor margins were delineated by MSPLI. Combination of MSPLI and CM appears to be complementary. This combined *in situ* technique has a potential to guide cancer surgery more rapidly, and at lower cost than conventional histopathology.

Key Words: multi-spectral imaging /confocal microscopy/ skin cancer /dyes

1 Introduction

Advances in the development of optical imaging modalities[1, 2, 3] have facilitated efforts to employ these techniques for noninvasive detection and treatment guidance of different pathological conditions. In general, the turbidity of tissue creates major challenges for optical *in vivo* spectroscopy and imaging. However, reflectance imaging techniques, like multi-spectral polarized light macro-imaging and confocal microscopy are well suited for skin cancer detection and demarcation. Confocal reflectance microscopy was introduced to the field of dermatology in the nineties.[4] Since then it has been used to study different skin disorders.[5, 6] Confocal microscopy is a technique where the specimen is pointwise illuminated by a focused beam of light. An image is recorded by scanning the beam focus through a plane in the specimen, and the reflected light from the specimen is focused onto a small detector aperture. The light source, the illuminated spot and the detector aperture are placed in optically conjugated focal planes. ”Optical sectioning" occurs as out-of-focal-plane back-scattered light is rejected by a pinhole placed in front of a detector. Optical sectioning makes it possible to record images of thin layers within tissue. Confocal microscopy allows imaging within turbid media with high resolution (lateral ~ 1 μm, axial (section thickness) ~ 3-5 μm), which is comparable to histology. The major disadvantage of confocal microscopy as a detection and guidance tool for cancer surgery is its small field of view (typically, up to about 0.3 mm). By sacrificing axial resolution up to ~30 μm it is possible to enlarge the field of view up to 2 mm. But even a 2-mm field of view is much smaller than the size of most lesions. To examine the entire suspected cancerous area using CM, a sequence of images must be

captured and stitched together. This process takes time and motion artifacts may distort the resulting image.

Multi-spectral polarized light imaging (MSPLI)[7] is a simple and inexpensive technique for skin tumor imaging. The technique provides the means to differentiate effectively between endogenous (blood, melanin, etc) and exogenous (dye) chromophores absorbing in different spectral domains and is capable of obtaining superficial images (~150 μm in the visible spectral range) of thick tissue layers. It is relatively insensitive to small shifts in the position of the imaged object. Combination of the large field-of-view and sufficient lateral resolution enables rapid examination of large surfaces, thus facilitating tumor margin delineation. However, morphology of individual cells and fine structures cannot be resolved using MSPLI. Thus, the multi-spectral polarized light imaging approach naturally lends itself to a combination with confocal reflectance microscopy technique, which can be used by a pathologist in the cases when high-resolution images of small suspicious areas are required. Such combination may become a powerful tool for cancer detection and demarcation.

In this study the possibility of combining multi-spectral polarized light macro-imaging and confocal microscopy for delineating nonmelanoma skin cancers, i.e. basal cell carcinoma (BCC) and squamous cell carcinoma (SCC), was investigated. 23 freshly excised thick skin samples with nonmelanoma skin cancers were stained with either toluidine blue O (TB) or methylene blue (MB), rinsed in acetic acid (AA), and imaged using CM and MSPLI systems. The acquired images were processed and compared to each other and to histopathology. The ability of this combined technique to delineate tumor margines and distinguish different tissue structures was evaluated.

2 Materials and Methods

2.1 Multi-Spectral Polarized Light Imaging

A schematic of the multi-spectral polarized light imaging system is presented in Figure 1. We used a xenon arc lamp (Lambda LS, Sutter Inc., Novato, CA) combined with interference filters as a narrow-band light source and a CCD camera (CoolSNAP Monochrome Photometrics, Roper Scientific Inc., Tuscon, AZ) as an imaging device. Linearly polarizing filters were introduced into the pathways of incident light and light collected by the camera to enable imaging using co- and cross-polarized scattered light. The automated system provided rapid image acquisition and processing at multiple wavelengths, large field of view (maximum: 2.9 cm X 2.7 cm), and lateral resolution of approximately 30 μm. The incident power density did not exceed 150 μW/cm^2.

To image a superficial tissue layer of approximately 150 - 200μm [7,12], two images were acquired using the remitted light polarized in the directions parallel ($I_{\parallel}$) and perpendicular ($I_{\perp}$) to the polarization of incident light[7,12]. It has been shown previously that the difference image ($I_{\delta} = I_{\parallel} - I_{\perp}$) is produced mainly by single scattered light.[12, 13, 7] The images were acquired from the dermal side of the specimens at the wavelengths of the phenothiazine dyes absorption, 630 nm and 660 nm, and at the reference wavelength of 750 nm. The acquired images were processed in the following way. The difference images, I_{δ}, were calculated for each wavelength. To reject the background signal, the resulting superficial macro-images, $I_{\Delta}^{\lambda} = I_{\delta}^{\lambda} - I_{\delta}^{\lambda_r}$, for λ= 630 nm, 660 nm; λ_r=750 nm, were computed, analyzed, and compared to CM images and histopathology.

2.2 Confocal Microscopy

A schematic of the confocal imaging system is presented in Figure 2. For the experiments, a commercial reflectance CM (Vivascope 2000, Lucid Inc., Henrietta, NY) was modified in the following way. In addition to the existing infrared laser diode (λ=830nm) the light from an argon-ion laser (Innova 100, Coherent, CA) pumped dye laser (Coherent 599, Coherent, CA) was coupled into the microscope. To optimize broad band visible and infrared light transmission through the system several optical components of the original configuration, i.e. polarizing beam splitter, lenses, and quarter waveplate were replaced by high-performance substitutes. Integration of an additional light source allowed imaging in the wavelength range from 600 nm to 830 nm and enabled localization of MB and TB in thick skin excisions with nonmelanoma cancers. Confocal images were acquired at the wavelengths of 630 nm, 660 nm, and 830 nm. Water immersion 20X/0.75 objective (Nikon, Japan) was used in all experiments. The system provided an axial resolution of 5 – 6 μm, and lateral resolution of 1.2-1.5 μm in the range from 620 nm to 830 nm. The incident power for each wavelength was adjusted not to exceed 12 mW. Confocal images were acquired from the dermal side of the samples at the depth of 10 to 40 μm beneath the surface of the tissue. The depth of confocal imaging was chosen based on location, size, and surface curvature of the investigated part of the specimen. Single confocal images covered the area of 800 μm X 600 μm. To compare the results with macroscopic polarized light images, confocal mosaics were created from single confocal images. These mosaics covered an area of 8 mm X 6 mm. The resulting confocal images and mosaics were compared to MSPLI and histopathology.

2.3 Tissue Preparation

Fresh thick skin specimens containing nonmelanoma cancer were obtained from Mohs micrographic surgeries. In total 23 samples were used for the experiments. The study was performed according to a protocol approved by the institutional review board of Massachusetts General Hospital. Discarded tumor material that remained after Mohs histological analysis was used. The tissue was frozen in the microcryotome and thawed immediately before the experiment. Several contrast agents including methylene blue, toluidine blue O, and acetic acid were applied to the tissue in order to enhance the contrast of a lesion with respect to the healthy tissue. MB and TB are preferentially retained in carcinoma cells.[8] These dyes have similar chemical structures and physicochemical properties. Absorption band in the 550 nm – 700 nm region determines blue color of MB and TB. Acetic acid is often applied for confocal examination of different cancer types.[6,9] Washing with acetic acid leads to chromatin compaction inside the cell nuclei. Compacted chromatin increases light scattering by the nuclei, thus enhancing the contrast of the image. For the experiments each specimen was submerged for 10 - 20 minutes in isotonic DPBS (Dulbecco's phosphate-buffered solution) of MB or TB and for 2 minutes in 5% AA. 13 samples were stained using MB and AA (11 BCC and 2 SCC) and 10 samples using TB and AA (7 BCC and 3 SCC). After the excessive dye was rinsed off the samples, the intact tissue was imaged using CM and MSPLI systems. For imaging, cancer specimens were placed on a glass slide and covered with a cover slip. A drop of saline solution was added to prevent drying of the sample. To enable comparison of the results to histopathology, the images were acquired from the dermal side of the specimens.

2.4 Comparison of the Images to Histopathology

The resulting MSPLI and CM images were qualitatively compared to each other and to the last histological frozen section processed during Mohs surgery. Preparation of histological horizontal sections is described in detail elsewhere.[10, 11] Ideally, the last frozen section generated during surgery should reproduce the features of reflectance polarization image acquired from the remaining discarded piece of tissue that we use for the experiments (see Figure 3). However, the thickness of an optical section is approximately 150 - 200 μm. It is 30 - 40 times thicker than the histological section, which is only 5 μm thick. This difference in the thickness may contribute to the quantitative discrepancies in the size of the tumors determined from the MSPLI and histopathology. Confocal images were acquired from the depth of 10-40 μm below the surface of the tissue. Therefore they should closely resemble the last histological frozen section processed during Mohs surgery. However, the ideal correlation can not be expected as the spatial "gap" of 10 - 40 μm between the frozen and confocal sections is on the order of one to several cell dimensions. For these reasons quantitative comparison of the images to histopathology could not be done in a straightforward manner and was not attempted in this work. However, due to the obvious similarities of the tissue features present in histological slides, CM and MSPLI images, visual qualitative comparison of the tumor shape, size, and margins was performed.

3 Results and Discussion

Nodular basal cell carcinoma is the most frequently occurring type of nonmelanoma skin cancers. Confocal and polarized light superficial images of a representative specimen with nodular basal cell carcinoma stained in 0.2 mg/ml aqueous solution of MB acquired at 660 nm are presented in Figures 4 a and 4b, respectively. Contrast of the tumor with respect to normal tissue was sufficient for reliable delineation of the cancer margins in both CM and MSPLI images. CM and MSPLI images, presented in Figures 4a and 4b, correlate well with corresponding histopathology, presented in Figure 4 c. Comparison of the images in Figures 4a and 4b shows that a CM mosaic provides more information than MSPLI on the arrangement and structure of separate tumor lobules but is not capable of visualizing the complete sample, whereas an MSPLI image provides a larger field of view, but does not show single tumor nests. The differences in resolution can be explained mainly by a difference in the optical section thickness between CM and MSPLI. The optical section thickness of each confocal image is ~5-6 μm, approximately 30 – 40 times less than that of each MSPLI macro-image. Skin tumor excisions are thicker in the center and thinner at the edges. Therefore it is usually not feasible to create CM mosaic over the whole sample including the boundaries whereas in the superficial macro-image the complete sample is visualized. Another practical factor limiting confocal imaging is that CM requires the imaged sample surface to be held flat, which is difficult to achieve for a large surgical tissue sample. In contrast, MSPLI imaging does not require the sample surface to be flattened.

Infiltrative BCC tumors are a common variant of BCC, that typically have thin strands or cords of tumor cells extending into the surrounding dermis. This type of tumor

is usually hard to delineate. A surgical excision specimen with an infiltrative BCC was stained using aqueous solution of TB (0.2 mg/ml) and imaged at the wavelength of 630 nm, which is within the absorption band of the dye, and at 830 nm, where absorption of the dye is negligible. Confocal mosaics of the acquired images are presented in Figures a and b. It is difficult to localize the dye in Figure 5a (confocal mosaic at 830 nm), while the dark areas in Figure 5b (confocal mosaic at 630 nm) clearly demarcate areas of high dye concentration, corresponding to tumor. As in the case shown in Figure 4 of a nodular BCC stained in MB, the confocal mosaic at 630 nm and the superficial polarized light image acquired at the same wavelength (figure 5c) are remarkably similar. Comparison of these two images with the last frozen section processed during Mohs surgery, presented in Figure 5d, demonstrates good correlation with histopathology. However, due to inherently lower resolution, the separate tumor lobules that are clearly visible in the CM mosaic can hardly be seen in the superficial macro-image. This case illustrates the value of combining CM and MSPLI in order to see both the small tumor lobules and the wider field tumor borders, respectively.

Confocal images presented in Figures 6 a and b are taken from the squares outlined in the CM mosaics at 830 nm and 630 nm, shown in Figures 5 a and b. Corresponding histopathology is shown in Figure 6 c. These confocal images were acquired at the margin of the tumor and contained several tumor lobules (red arrows) mixed with areas of healthy tissue. Margins of the tumor can hardly be delineated in the image acquired at 830 nm, whereas in the image acquired at 630 nm the tumor is much darker than healthy tissue and can be easily demarcated. Comparison of the image at 630 nm (Fig. 6b) to

frozen H&E section (Fig. 6c) confirms that position and shape of single tumor lobules is determined correctly by confocal microscopy.

In Figure 7 images of invasive squamous cell carcinoma, stained using 0.1 mg/ml aqueous solution of TB are presented. Polarized macro-image acquired at 630 nm and corresponding histological section are shown in Figures 7a and b. The shape and the size of the tumor that appears dark in the macro-image correspond well to that outlined with red marker in histology. Confocal image of the part of cancerous area acquired at 630 nm and corresponding histopathology are presented in Figures 7c and d, respectively. Morphological appearance of the tumor micro-structure is very similar in the confocal image and histology. Tumor cells appear bright due to scattering enhanced by acetic acid. Location and shape of the tumor lobules correlates well with those in H&E stained frozen section. This example shows that combination of topical staining using phenothiazine dyes and rinsing in AA may further enhance the similarities in the appearance of the acquired images and histopathology, thus simplifying interpretation of macro- and confocal images.

In Figure 8a polarized light macro-image of basal cell carcinoma specimen stained in 0.2 mg/ml aqueous solution of MB acquired at 660 nm is presented. Two strongly stained islands of BCC can be clearly delineated in the image. Magnified confocal images of the BCC lobule, that is outlined in red in Figure 8a, acquired at 660 nm (strong absorption by MB) and 830 nm (negligible absorption by MB) are shown in Figures 8b and c, respectively. Detailed evaluation of confocal images taken at 660 nm and 830 nm demonstrates that one part of the suspicious area (marked with green arrow) appears dark in both images, whereas another part (marked with red arrow) is much darker in 660 nm,

as compared to 830 nm image. Therefore, the area that is clearly darker in the 630 nm image than in the 830 nm image, contains significant amount of the dye and can be presumed to be a tumor. However, the suspicious area that is dark at both wavelengths implies a structure with low scattering, and comparatively low dye uptake. In skin, sebaceous glands appear as such lower-scattering structures. Comparison of the images to histology, presented in Figure 8d confirms that these dark areas contain a tumor lobule and a sebaceous gland (red and green arrows, respectively).

In total, we have investigated 23 thick surgical excisions of nonmelanoma skin cancer, including 18 basal cell carcinoma (nodular and infliltrative) and 5 invasive squamous cell carcinoma samples. The lateral size of the nonmelanoma skin cancer specimens varied from 4 to 36 mm and the thickness from 3 to 18 mm, respectively. The lateral sizes of the tumors ranged from 0.5 mm to 15 mm. For 13 tumors with the lateral sizes less than 8 mm X 6mm, confocal mosaics were created and qualitatively compared to superficial macro-images and histopathology (representative images are shown in Figures 4 and 5). In all the cases the locations of the tumors were correctly determined in the superficial macro-images and in the confocal images, acquired at 630 nm and at 660 nm for the samples stained in TB and MB, respectively. The shape and the size of the tumor lobules found in confocal and superficial macro-images correlated well with corresponding histopathology. For all the samples the interesting features, such as tumor lobules, sebaceous glands, hair follicles, etc were identified and compared to histopathology (see representative images presented in Figures 6, 7, and 8). The comparison confirmed that tissue structures have similar appearance in the images and histopathology.

This study demonstrates that polarized light marcro-imaging and confocal mosaics are a useful combination for delineation of nonmelanoma skin cancer margins in both BCC and SCC. Polarized light macro-imaging is better than CM for macroscopic assessment as it gives a larger field of view (~2.9 cm X 2.7 cm) almost instantaneously (~ 100 msec), does not require scanning or contact with tissue, and is not susceptible to patient movement. Confocal images acquired at a wavelength within the absorption band of a tumor specific dye allows delineation of single tumor lobules, with contrast and resolution comparable to those of conventional histopathology. Rapid acquisition of confocal images at several wavelengths helps to discriminate cancer lobules with high dye concentration from healthy tissues with comparatively low scattering. It is not difficult to localize small structures in the tissue using confocal microscopy after a high contrast dye-enhanced macro-image has been acquired. Synergy between these two optical techniques implies that the combination could be successfully used for intraoperative assessment of nonmelanoma skin cancer margins. Similar appearance of different tissue structures in histological sections and our images simplifies the process of image understanding. It ensures that image interpretation can be performed by a pathologist without any assistance.

In conclusion, MSPLI enables rapid imaging of large surfaces, but does not provide information on cellular microstructure. CM allows imaging with resolution comparable to histology, but suffers from small field of view. The combination of MSPLI and CM offsets the specific limitations of each technique alone, and may in practice rival conventional histopathology. By allowing the tumor to be delineated *in situ*, this approach may decrease the cost and time of cancer surgery.

Acknowledgements

We thank Milind Rajadyaksha, PhD and Salvador Gonzalez, MD, PhD, for helpful discussions. Technical support of Lucid, Inc (Henrietta, NY) is gratefully acknowledged.

This research is supported in part by National Institutes of Health (R01 EB002423-01).

References

1. Rajadhyaksha M, Anderson RR, Webb RH: Video-rate confocal scanning laser microscope for imaging human tissues *in vivo*. *Appl.Opt.* **10**:2105-2115, 1999
2. Wagnieres G, Star W, Wilson BC: *In vivo* fluorescence spectroscopy and imaging for oncological applications. *Photochem. Photobiol*. **68**:603-632, 1998
3. Boppart SA, Bouma BE, Pitris C, Tearney GJ, Southern JF, Brezinski ME, Fujimoto JG: Intraoperative assessment of microsurgery with three-dimensional optical coherence tomography. *Radiology.* **208**:81-6, 1998
4. New KC, Petroll WM, Boyde A et al.: In vivo imaging of human teeth and skin using real-time confocal microscopy. *Scanning* **13**:369-372, 1991
5. Rajadhyaksha M, Grossman M, Esterowitz D, Webb RH, Anderson RR: In vivo confocal scanning laser microscopy of human skin: melanin provides strong contrast. *J. Invest. Dermatol.* **104**:946-952, 1995.
6. Rajadhyaksha M, Menaker G, Dwyer PJ, Flotte TJ, González S: Confocal examination of nonmelanoma cancers in skin excisions to potentially guide Mohs micrographic surgery without frozen histopathology. *J. Invest. Dermatol.* **117**: 1137-1143, 2001.

7. Yaroslavsky AN, Neel V, Anderson RR. Demarcation of nonmelanoma skin cancer margins using multi-spectral polarized-light imaging. *J. Invest. Dermatol.* **121**:259-266, 2003
8. Oseroff AR, Ohuoha D, Ara G, McAuliffe D, Foley J, Cincotta L: Intramitochondrial dyes allow selective *in vitro* photolysis of carcinoma cells. *Proc. Natl. Acad. Sci. USA*, **83**: 9729-9733, 1986
9. Drezek RA, Collier T, Brookner CK, Malpica A, Lotan R, Richards-Kortum RR: Laser scanning confocal microscopy of cervical tissue before and after application of acetic acid. *Am. J. Obstet. Gynecol*. **182**:1135-1139, 2000
10. Mohs FE: Chemosurgery – a microscopically controlled method of cancer excision. *Arch.Surg*. **42**: 279-295, 1941
11. Gross KG, Steinman HK, Rapini RP ed. Mohs Surgery: Fundamentals and Techniques. Mosby, Inc., 1999
12. Jacques SL, Roman JR, Lee K: Imaging superficial tissues with polarized light. *Las.Surg.Med.* 2000; **26**:119-129
13. Backman V, Wallace M, Perelman LT, et al. Detection of Preinvasive Cancer Cells. Early-Warning Changes in Precancerous Epithelial Cells Can Now be Spotted In Situ. Nature 2000;406,6791:35-36.

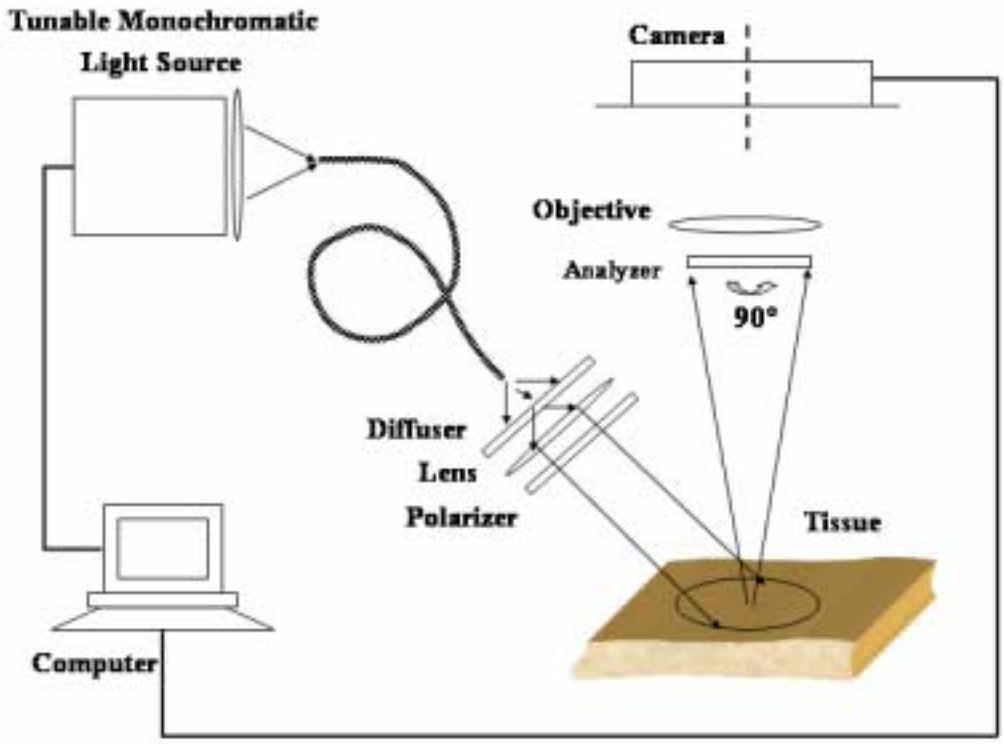

Figure 1. Schematic diagram of multi-spectral polarized light imaging system.

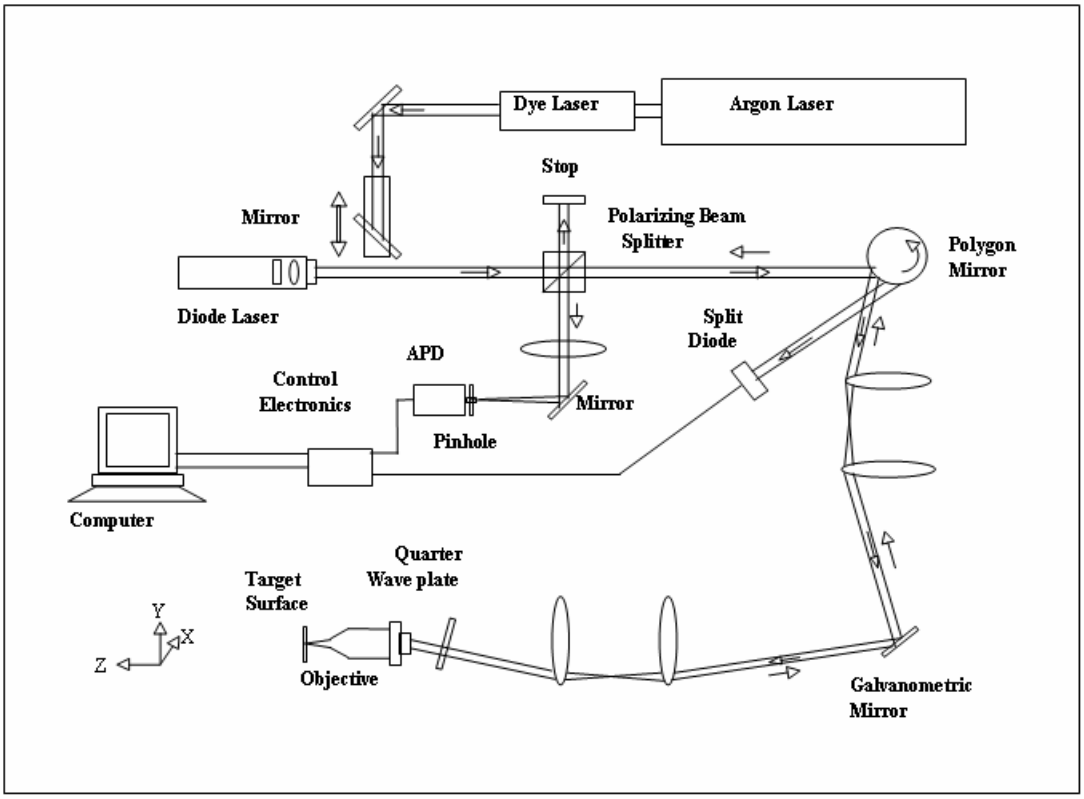

Figure 2. Schematic diagram of the confocal microscope.

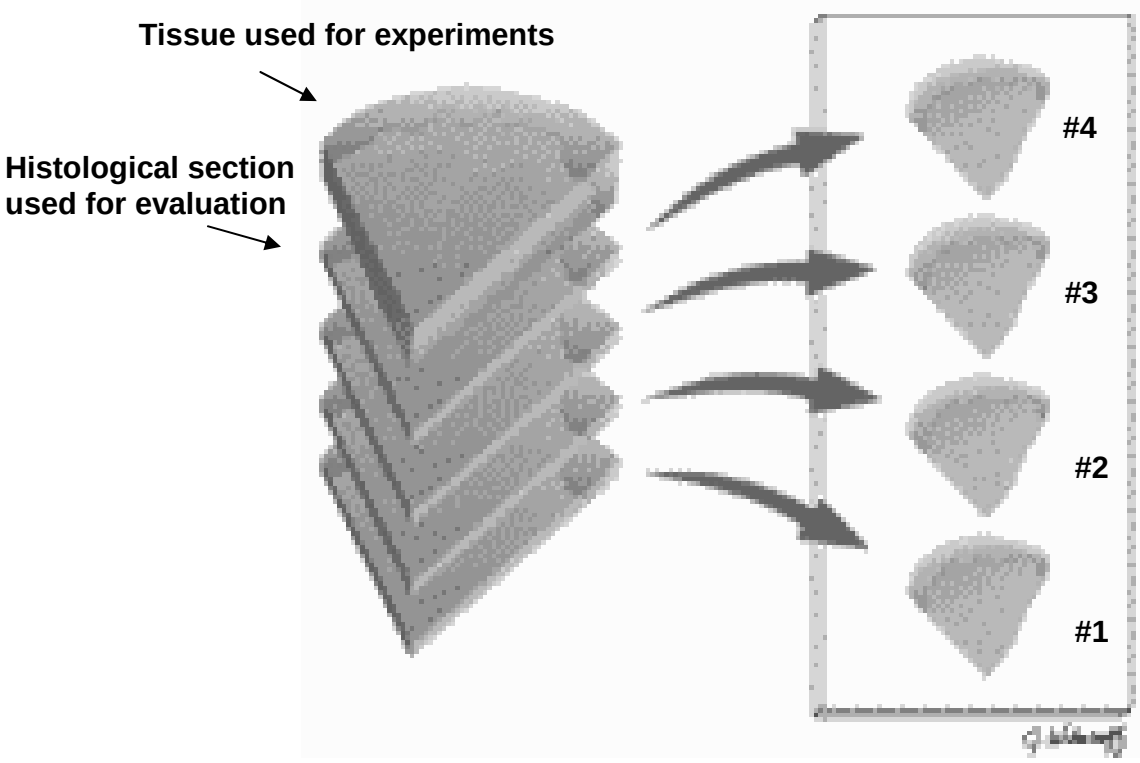

Figure 3. Preparation of the horizontal histological frozen sections.

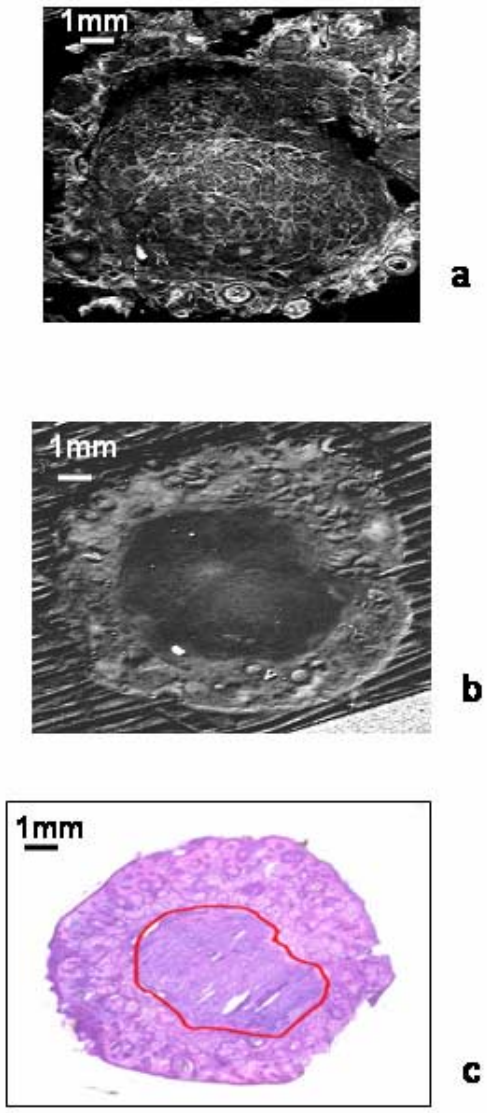

Figure 4. Images of nodular BCC stained in 0.2 mg/ml aqueous solution of MB: a) confocal mosaic acquired at 660 nm; b) superficial macro-image acquired at 660 nm; c) histological frozen section. Tumor margins in (c) as determined by Mohs surgeon are outlined with red line.

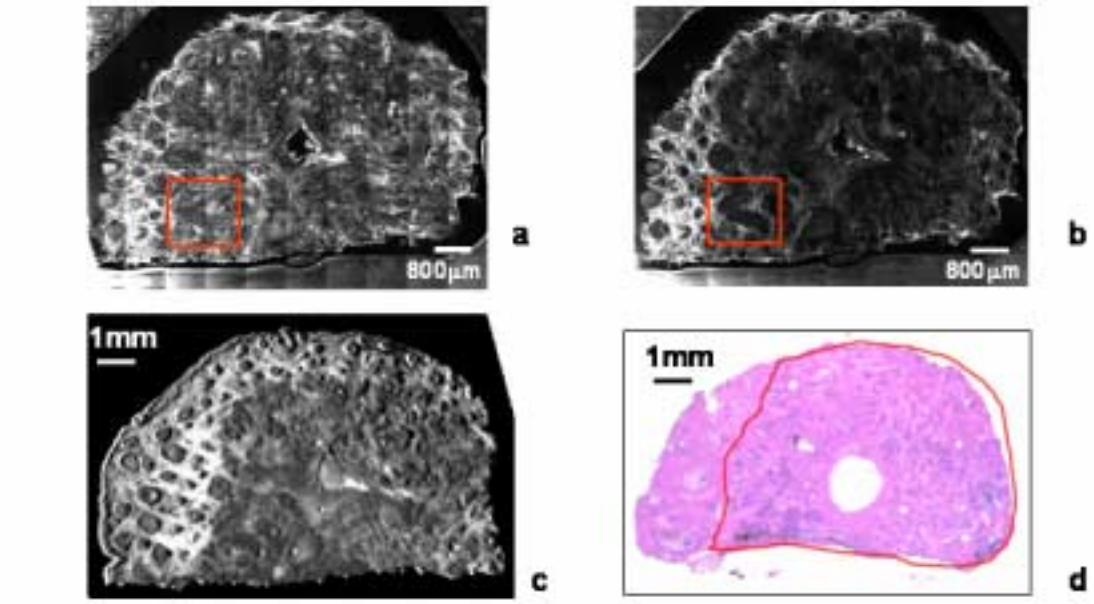

Figure 5. Images of infiltrative BCC stained in 0.2 mg/ml aqueous solution of TB. a) Confocal mosaic acquired at 830 nm. b) Confocal mosaic acquired at 630 nm. c) Superficial macro-image acquired at 630 nm. Red square in the confocal mosaics outlines the area presented in the confocal images in Figures 6a and b. d) Histological frozen section. Tumor margins in (d) as determined by Mohs surgeon are outlined with red line.

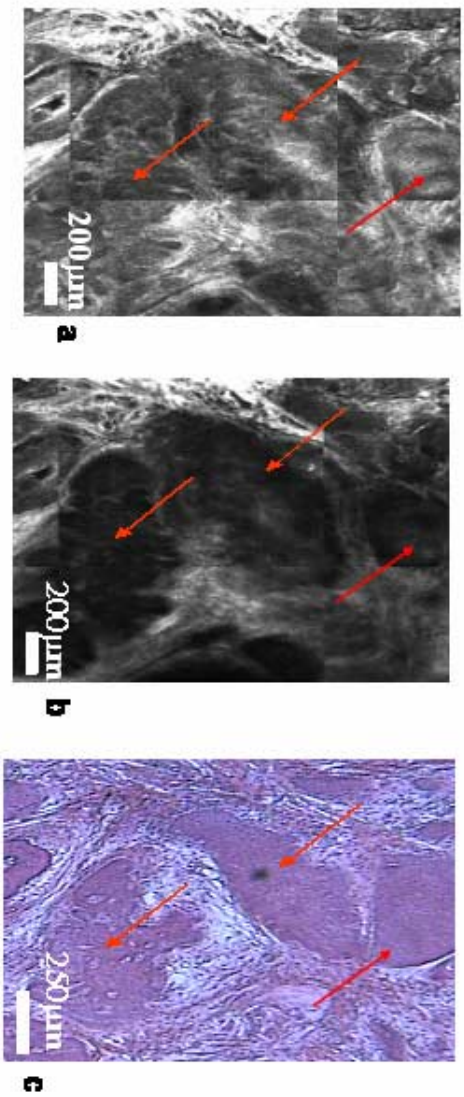

Figure 6. Images of infiltrative BCC stained in 0.2 mg/ml aqueous solution of MB. Red arrows point to the locations of the tumor lobules. a) Confocal image at 830 nm taken from the red square area of the mosaic presented in Fig. 3 a. b) Confocal image at 660 nm taken from the red square area of mosaic presented in Fig.3 b. c) Histological frozen section.

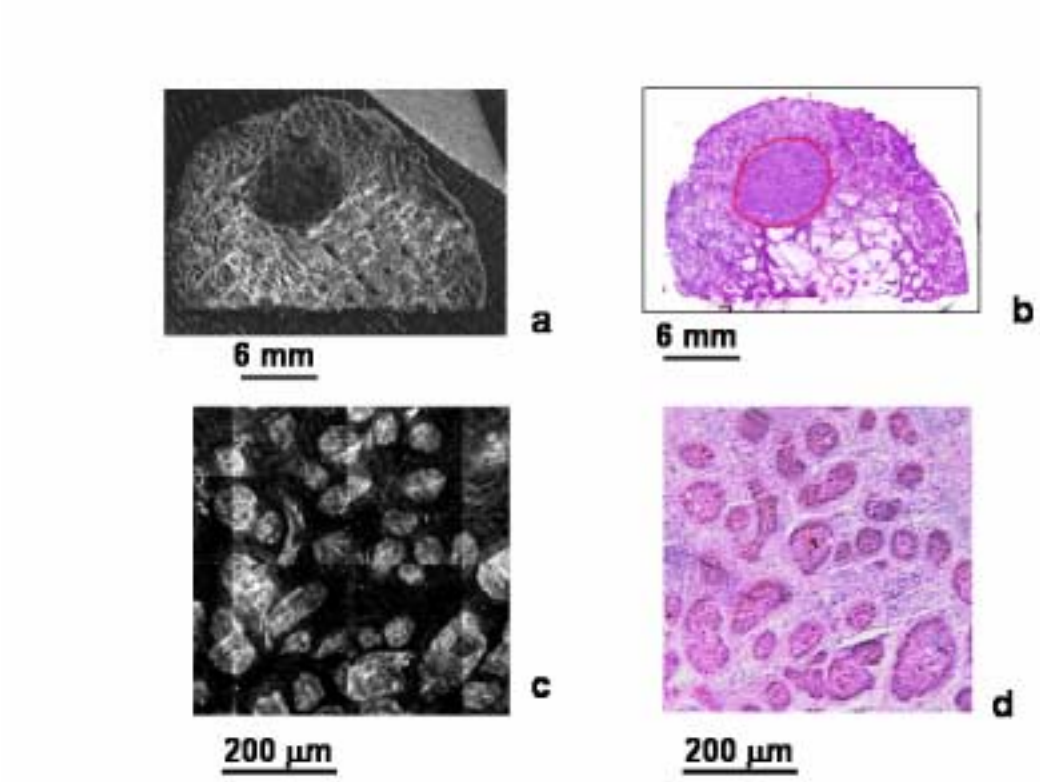

Figure 7. Images of invasive SCC stained in 0.1 mg/ml aqueous solution of TB. a) Superficial macro image acquired at 630 nm. b) Histological frozen section. Tumor margins in (b) as determined by Mohs surgeon are outlined with red line. c) Confocal image of cancer acquired at 630 nm. d) Magnified image of the histological frozen section taken from the same area as presented in Figure 7c.

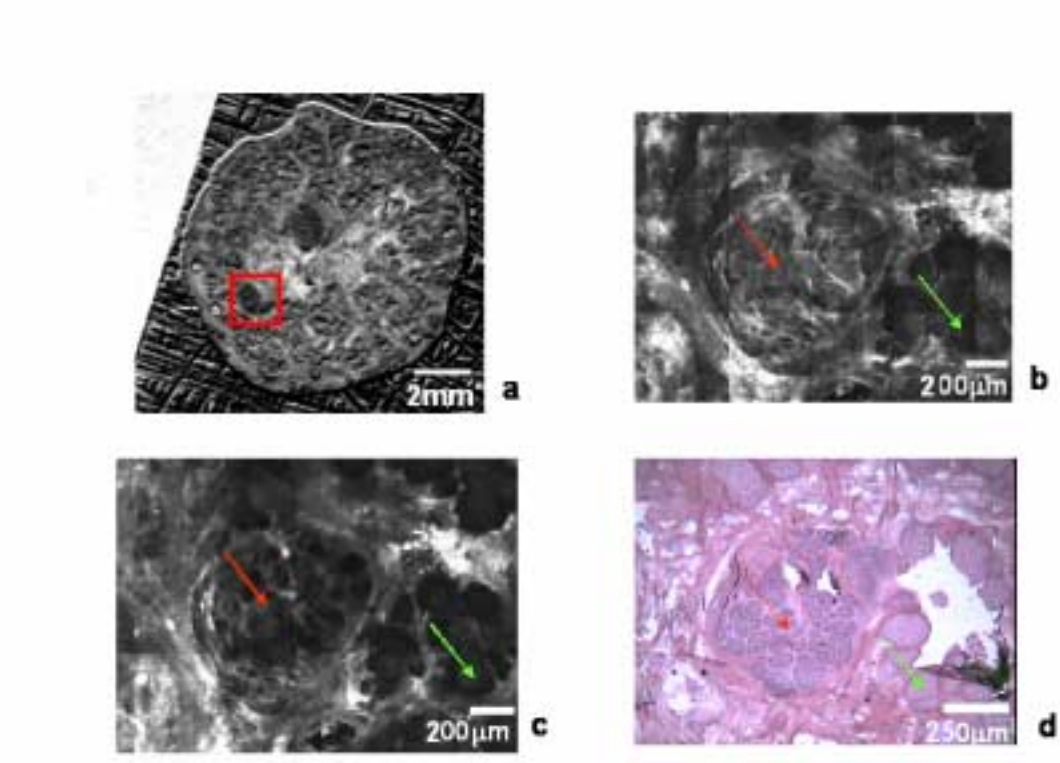

Figure 8. Images of micro-nodular BCC stained in 0.2 mg/ml aqueous solution of MB. a) Superficial macro-image acquired at 660 nm. Red square outlines the area presented in confocal images and histopathology in Figures 8b, c, and d. b) Confocal image at 830 nm taken from the red square area of the macro-image presented in Fig.8 a. c) Confocal image at 660 nm taken from the red square area of the macro-image presented in Fig.8 a; d) histological frozen section. Red arrow shows the location of tumor lobules, green arrow shows sebaceous glands.

NORTHEASTERN UNIVERSITY

Graduate School of Engineering

Thesis Title: Multi-Spectral Confocal Microscopy for Localization of Exogenous Contrast Agents in Nonmelanoma Skin Cancers

Author: Jose Goncalves Barbosa

Department: Electrical and Computer Engineering

Approved for Thesis Requirement of the Master of Science Degree

_____	_____
Thesis Advisor	Date
_____	_____
Thesis Co-Advisor	Date
_____	_____
Thesis Reader	Date
_____	_____
Department Chair	Date

Graduate School Notified of Acceptance:

_____	_____
Director of the Graduate School	Date

NORTHEASTERN UNIVERSITY

Graduate School of Engineering

Thesis Title: Multi-Spectral Confocal Microscopy for Localization of Exogenous Contrast Agents in Nonmelanoma Skin Cancers

Author: Jose Goncalves Barbosa

Department: Electrical and Computer Engineering

Approved for Thesis Requirement of the Master of Science Degree

_____	_____
Thesis Advisor	Date
_____	_____
Thesis Co-Advisor	Date
_____	_____
Thesis Reader	Date
_____	_____
Department Chair	Date

Graduate School Notified of Acceptance:

_____	_____
Director of the Graduate School	Date

Copy of Deposited in Library:

_____	_____
Reference Librarian	Date